Designing Metal Nanoparticles for Catalysis

Scott M. Rogers

Department of Chemistry

University College London

Primary Supervisor: Professor C. Richard A. Catlow

Secondary Supervisor: Dr. Peter P. Wells

Thesis submitted for the degree of Doctor of Philosophy

2017

Declaration

I, Scott M. Rogers confirm that the work presented in this thesis is my own. Where information has been derived from other sources, I can confirm that this has been indicated in the thesis.

……

Abstract

The sol-immobilisation method, in which metal nanoparticles are 'preformed' (stabilised by the polymer, polyvinyl alcohol) before they are anchored to a support material, was adapted in order to prepare monometallic Au/TiO_2 and Pd/TiO_2 catalysts, with tailored properties. Varied temperature and solvent environments (H_2O, mixed H_2O:EtOH and EtOH) were employed during colloidal metal formation, generating metal particles with distinct characteristics (metal particle diameter and available metal sites). The metal nanoparticle properties in the resulting catalysts were fully characterised using a range of spectroscopic (XAFS, IR and UV-Vis) and imaging techniques (TEM and HAADF STEM). It was determined that the preparation of metal nanoparticles at −30°C, in a mixed H_2O:EtOH solvent afforded the smallest average particle diameter, regardless of the choice of metal (2.0 nm for Au, 1.4 nm for Pd). However, when prepared at 1°C in H_2O, a higher population of small Au (< 5 atoms) or Pd clusters (< 20 atoms) existed, compared with any other environment.

The performance of the catalysts were tested in three different reactions; Au/TiO_2 for the oxidation of glycerol, and Pd/TiO_2 for the hydrogenation of furfural and *p*-nitrophenol. For the two former reactions, it was established that metal particle size is not the only factor influencing performance; the highly active isolated metal clusters, as well as the solvent-PVA-metal interaction, are considered very important factors, and are discussed.

Understanding colloidal metal formation, including nucleation and growth phenomena, is vital in the future design of metal nanoparticle properties, and was investigated by means of *in situ* XAFS. A continuous flow method of nanoparticle synthesis was first explored and developed, before a synchrotron based experiment was performed to monitor the nanoparticle generation (colloidal reduction) in a range of reactors fabricated from different materials (silicon/glass, PTFE and PEEK).

Acknowledgements

There are many people who contributed to the work presented in this thesis and deserve credit. Firstly, I need to thank my UCL supervisors Professor Richard Catlow and Dr. Peter Wells for their continual assistance and guidance throughout the project. I am also grateful for the great dedication of Peter throughout my PhD, including daily scientific discussions about the project, as well as helping me with individual skills (communication and supervisory guidance). Dr. Nikolaos Dimitratos of Cardiff University has played a big role in the projects, most notably in helping establish collaborations, offer a wealth of ideas and always being there for a friendly chat.

The PhD was funded by the Engineering and Physical Sciences Research Council, for which I am very grateful.

All the collaborators produced high quality work helping strengthen projects. Dr. Alberto Villa and Dr. Carine Chan-Thaw from the University of Milan are thanked for the multiple catalytic reactions, project discussions and contribution to publications. Nan Jian, a member of Professor Richard Palmer's research group at the University of Birmingham, is thanked for providing high quality STEM HAADF images. I am also grateful to some of Richard Catlow's computational team at UCL, including Anna Gould, Dr. Andrew Logsdail, Dr. Arun Chutia and Dr. Adam Thetford, who performed computational studies.

At the institute I was based, the Research Complex at Harwell, I would like to thank the researchers and technicians, namely Dr. Emma Gibson and Dr. June Callison, who provided training, offered advice or performed analysis that contributed to the project. I would also like to thank the other students, and friends, Antony Vamvakeros, Wilm Jones, Alex O'Malley, Anna Gould, Miren Agote and Cath Brookes, who provided lots of 'banter' and support throughout.

Finally, the belief, support and love passed from my family, and long term girlfriend Charlotte has provided the motivation to succeed each day, and so I am extremely grateful.

Publications from this thesis

Scott M. Rogers, C. Richard A. Catlow, Carine E. Chan-Thaw, Diego Gianolio, Emma K. Gibson, Anna L. Gould, Nan Jian, Andrew J. Logsdail, Richard E. Palmer, Laura Prati, Nikolaos Dimitratos, Alberto Villa, and Peter P. Wells, *ACS Catal.*, **2015**, *5* (7), pp 4377–4384.

Scott M. Rogers, C. Richard A. Catlow, Carine E. Chan-Thaw, Arunabhiram Chutia, Nan Jian, Richard E. Palmer, Michal Perdjon, Adam Thetford, Nikolaos Dimitratos, Alberto Villa, and Peter P. Wells, ACS Catal., **2017**, 7 (4), pp 2266–2274.

Table of Contents

Chapter One: Introduction

Chapter Two: Materials and Methods

Chapter Three: Au/TiO_2 for the Oxidation of Glycerol

Chapter Four: Pd/TiO_2 for the Hydrogenation of Furfural

Chapter Five: Pd/TiO_2 for the Hydrogenation of *p*-Nitrophenol

Chapter One. Introduction

The themes that underpin the scope of work undertaken within this thesis are introduced in this chapter. Particular attention is given to the use of nanoparticles within heterogeneous catalysis; their applications, their conventional routes to preparation, and how new scientific methodologies are allowing advances in the field.

1. Introduction to Catalysis

1.1. Catalysis and the Global Economy

Catalysis is fundamental to many processes that contribute to present day life and, more importantly, to a sustainable future.[1] Chemical processes, that are essential for heavily industrialised economies, rely on catalysts to lower the required energy input and increase rates of reaction. Indeed, in excess of 90 % of all chemical processes rely on catalysts.[2-3] The enhancement afforded by catalysts is achieved by providing alternative reaction pathways, where the transition state involved is of lower free energy.

In a world where there is a rising population (7.4 billion in 2016[3]) and finite resource, the move towards sustainable processes of improved atom efficiency and low energy input are essential. Catalysis offers a unique solution both to reduce waste, by creating more selective processes, as well speeding up the reaction kinetics.

In addition to energy generation, there are many processes that involve chemical 'upgrading' to produce products that are more useful in everyday life, such as in the polymer, petrochemical, pharmaceutical and fine chemical industries.

1.2. Heterogeneous Catalysis

There are distinct areas of catalysis that include electro-, bio-, homogeneous- and heterogeneous catalysis. Catalysts participating in electrochemical reactions are termed electrocatalysts, for example, in the case of fuel cells. Natural catalysts, enzymes or cells, are labelled biocatalysts, and have the ability to perform chemical transformations on organic compounds. They attract interest in the field of catalysis due to their chemo-, regio-, and most importantly, enantioselectivity.

The terms homogeneous and heterogeneous catalysis are used when the catalyst material and reactant are in the same (i.e. liquid/liquid), or different (i.e. solid/liquid, solid/gas) phases, respectively.

The present study focuses on heterogeneous catalysis, in which the catalyst is present as a solid, and the reactants are in the liquid phase. The main advantage lies in the catalyst recycling, as the two components (products and catalyst) can be easily separated after reaction, and therefore recycled more easily. Typically, two reaction set-ups are employed when performing heterogeneous catalysis of this nature; batch or continuous flow methods.

The development over the past 30 years in heterogeneous catalysis has largely focused on engineering catalyst materials down to the nanoscale, as well as finding practical and effective synthesis methods. Solid materials in the size regime 1-100 nm are defined as nanoparticles. Particular interest into metal nanoparticles for catalysis has been due to their advantageous properties compared with their larger counterparts:

1) Larger available surface area per unit mass.
2) A different proportion of the types of site available.
3) The energy of the surface is altered by the ultra-small size domain of the particle.
4) Reduction in the amount of metal required.

The important characteristics/properties of the metal nanoparticles governing catalytic performance include metal particle size, shape and structure. To help disperse and stabilise the metal nanoparticles, they are often anchored onto a support material, and so the metal-support interaction is an additional property to consider. Elucidating the effects such properties have towards catalytic performance, and establishing structure-performance relationships is fundamental in the future design of metal nanoparticle catalysts.

2. Designing Metal Nanoparticles

2.1. Controlling Nanoparticle Size and Shape

Thrifting of precious metals by increasing the surface area per gram of catalyst (decrease metal particle size), not only reduces the cost of catalyst production but also

the associated environmental consequences of the mining activities. The reduced sized particles also have a higher proportion of corner and edge sites (figure 1), which change the binding properties of different reactants. There can often be a compromise between these two effects, as shown by the performance towards the oxygen reduction reaction (ORR) catalysed by nano-particulate Pt. In the ORR the planes provide the most active sites for binding O_2 over two adjacent Pt atoms, resulting in a mass normalised activity plot to exhibit a volcano style curve; the smallest nanoparticles contain fewer of the active sites and the larger particles have too little surface area, meaning a compromised size regime gives the highest mass normalised activity.[4] Conversely, there are reports in which the catalysis occurs preferentially on isolated sites, and hence minimising the nanoparticle size is favoured. This behaviour is observed for CO oxidation on Au, in which the low coordinated Au atoms (corners and edges) are the active sites, as they are able to bind CO and oxygen.[5]

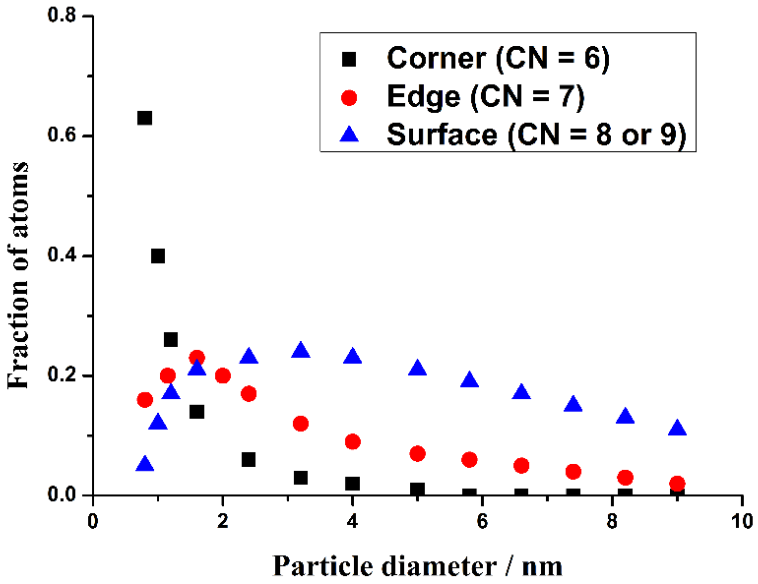

Figure 1. The fraction of atoms located on surface, corner or edge sites in an octahedron as a function of particle diameter.[5]

Controlling the shape of metal nanoparticles is an ongoing challenge. However, there are many reports in which this aim has been achieved, predominantly through colloidal methods.[6-7] The observed metal nanoparticle shape is a result of the different crystal planes present and has a direct effect on the adsorption/desorption properties, and metal-support interaction. There are many possible facet arrangements formed during catalyst synthesis, but typically, low index facets (e.g. 100, 110 and 111) are prominent

as these are the lowest energy arrangements due to the high coordination to surrounding atoms. Coincidently, if corner, edge and kink sites are deemed the active species, it is advantageous to prepare high index facet arrangements, as can be observed in figure 2.[8]

The metal surface area in contact with the support, and hence the number of periphery sites, varies with different shaped metal nanoparticles. In the case of CO oxidation on Au nanoparticles, the periphery is considered a key active site, and the performance is very much shape dependent.[9]

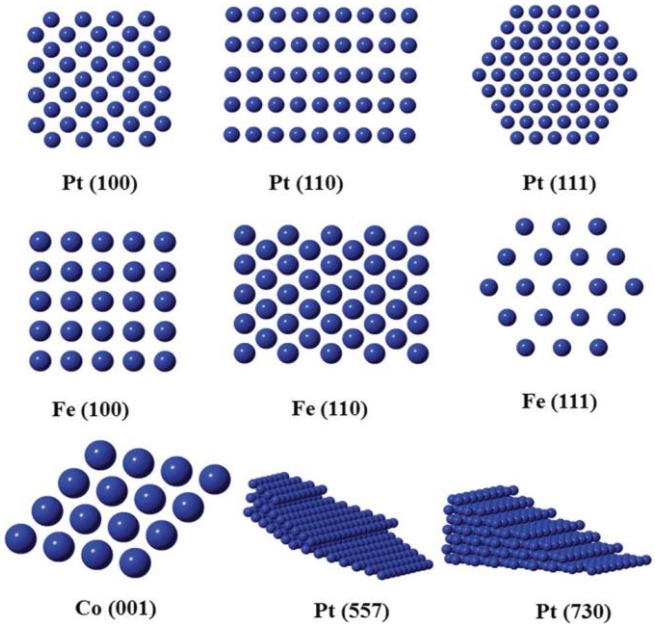

Figure 2. Atomic arrangements of low (e.g. (100), (110), (111)) and high index (e.g. (557), (730)) surfaces of metals indicating highly coordinated atoms and lowly coordinated atoms, respectively.[8]

2.2. Support Effects

One important factor defining a catalyst is its ability to operate, without itself undergoing any permanent chemical/structural change, which may lead to deactivation. Immobilising metal nanoparticles onto a support is an important tool in aiding nanoparticle durability and protects against metal leaching, and metal particle growth, so that they can be recycled. The role of the support, however, can also have an influence on the catalysis, either by, i) changing the structure and shape of the nanoparticles, ii) redox cycling of the metal ions (e.g. MnO_2, CeO_2 and Fe_2O_3 have a metal with two stable redox states), iii) charge transfer to or from the nanoparticles, or iv) acting as a surface for adsorbate species to bind in close proximity to the metal.[10]

The choice of the support material is often governed by the catalytic application. Carbon, for example, is used for fuel cell applications due to its high conductivity,[11] whereas TiO_2 is used in photocatalytic applications as it is a semiconductor with a suitable band gap.[12] In general, the high thermal and chemical stabilities, as well as high surface areas that metal oxides offer means they are suitable candidates for many applications.[13-14]

3. Preparation of Metal Nanoparticles

It is possible to tailor the properties of metal nanoparticles using different preparation routes. Traditional methods used commonly to date are based on impregnation and precipitation techniques, but there have been a growing development in colloidal methods, more specifically sol-immobilisation, as a result of their ability to tune the catalyst properties. The methods, in terms of their general synthesis procedures, advantages and disadvantages, will now be discussed.

3.1. Impregnation

Impregnation is a commonly used method to generate nanoparticles of different sizes. The technique involves 'wetting' of the solid support with a solution containing the desired amount of metal precursor (typically a metal salt). If the required metal is dissolved in to a volume of solvent equal to that of the total pore volume of the support (incipient wetness point), a thick paste like substance is obtained, and the technique is termed as incipient wetness impregnation. The solvent is evaporated off, and the material either obtained as the oxidised form, or subsequently transformed in to the reduced form, if required.

Controlling the morphology of the metal nanoparticles using this methodology is challenging. The metal particle size obtained is dependent on three main factors; the metal loading, support surface area and annealing atmosphere. A lower metal loading, as well as a high surface area support promotes the formation of smaller particles with greater dispersion.[15] High thermal treatments are necessary to remove unwanted chlorine residues, which subsequently leads to high levels of particle agglomeration, particularly in higher metal loading catalysts.[16]

3.2. Precipitation

Co-precipitation is the most common method for mixed-oxide catalyst preparation. It involves the simultaneous precipitation of the metal and support material using an aqueous alkaline solution (e.g $NaCO_3$ or K_2CO_3). In general, the co-precipitation method affords a strong metal-support interaction. Deposition-precipitation, similar to co-precipitation, involves addition of the metal precursor to an aqueous suspension of the support before subsequent precipitation as a hydroxide by raising the pH.[17] The surface of the support acts as a nucleating agent which leads to a greater part of the active precursor attached to the support. The hydroxide species is subsequently calcined and reduced to the desired need.[18] The high number of parameters that require control for precipitation methods, shown in figure 3, makes them very versatile, but differing conditions within the synthesis reactor can lead to an inhomogeneous catalyst, with segregated phases.

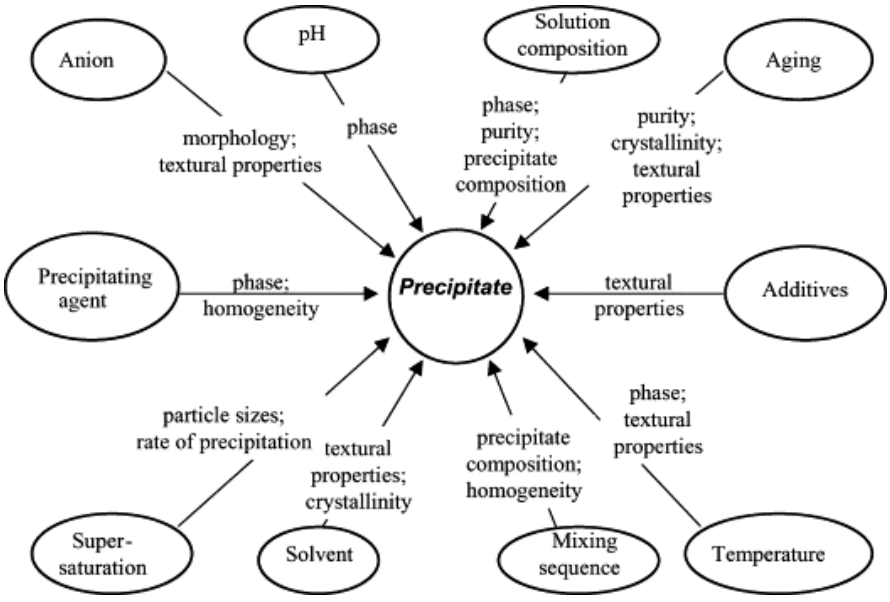

Figure 3. Factors affecting the properties of precipitated catalysts.[16]

3.3. Colloidal Methods

A colloid can be described as a mixture in which one substance is divided into minute insoluble particles and is dispersed throughout a second substance. Essentially, the metal precursor, commonly a salt, is reduced to zero valent metal in the presence of a stabilising agent. There are two types of methods by which stabilising agents act to protect the metal from agglomeration: electrostatic repulsion or steric inhibition. In

some cases, molecules can function as both electrostatic and steric protectors. There are many different molecules that can act as stabilising agents, including donor ligands, polymers and surfactants.

The sol-immobilisation technique is an extension of this method, and consists of anchoring the subsequent colloidal metal on to a support material, which is typically achieved by reducing the pH below that of the isoelectronic point (point of zero charge) of the support (pH ~ 6 for TiO_2), so as to enable the charge interaction between the metal and support. Essentially, the properties of the preformed metal nanoparticles can be tuned prior to their immobilisation, with the variation of many reaction conditions possible (i.e. metal concentration, stabiliser/metal ratio, reducing agent).[19]

Polymers are advantageous as they not only have the ability to tailor metal particle properties, but they also enhance the long term stability of metal nanoparticles during catalytic reactions.[20] Polymers can selectively bind to specific crystal facets, obtaining particles with shape and surface site control.[21-22]A variety of reducing agents can be employed (e.g. hydrogen, alcohols, hydrazine or boronhydrides), which can also influence the metal properties.[23] Poly(vinyl) alcohol is a long chained, high molecular weight polymer that acts to sterically protect the colloidal metal. Its high solubility in water allows for the utilisation of this protecting agent in a desirable 'green' solvent. The first use of PVA for this purpose was in 1996 by DiScipio.[24] Over the past 20 years it has been developed by Dimitratos and Prati,[25-26] and has been successfully used in the preparation of nanoparticles of differing metals.[23, 27] The role of the stabilising agent during catalysis has received a great deal of attention. It has been demonstrated that, for some liquid phase reactions, the presence of polymers at the metal surface does not inhibit the reaction, and acts to protect the metal nanoparticles from agglomeration.

4. Supported Metal Nanoparticles – Catalytic Applications

4.1. Gold Nanoparticles

Au for use in catalysis was for many years considered inert, or at least very inactive compared to other metals. In 1973, Bond *et al*. discovered and reported that supported gold catalysts were in fact useful for the hydrogenation of olefins.[28] More than ten years on, in the mid-1980's, Haruta *et al*. and Hutchings simultaneously discovered

that Au shows excellent catalytic activity when dispersed as small nanoparticles.[29-30] These reactions were the breakthrough for Au catalysis, paving the way for the study of Au in many other catalytic applications over the last 30 years, as well as the developments in catalyst design to optimise performance.

4.1.1. CO Oxidation

This low temperature, gas phase reaction has been widely studied on Au supported catalysts for its potential to remove CO in gas streams for the fuel cell industry. Trace CO poisons fuel cell catalysts which is detrimental to the catalyst performance. Haruta and co-workers identified that supported Au nanocrystals perform remarkably for this reaction, particularly at temperatures below 0 °C, which is not observed for other catalysts.[29] The first support material used was α-Fe_2O_3, but this has since been extended to other metal oxides including TiO_2, CeO_2 and Al_2O_3.[31] The nature of the active site has received a lot of attention, with *ex*- and *in-situ* characterisation techniques helping shed light on the matter. Three important factors are the mean Au particle size, the oxidation state of the Au, and the periphery sites at the Au/support interface. It has been shown that the turnover frequency for CO oxidation per surface gold atom is almost independent of the oxide support but increases sharply with a decrease in diameter of gold particles below 4 nm.[32] This is reasoned by the fact that CO is only adsorbed on steps, edges and corner sites with almost 0 kJ mol^{-1} activation energy.[33] However, Okazaki *et al.* demonstrated that the proportion of gold atoms in contact with the support increases with decreasing Au particle size, and so the support material influences the electronic nature of these atoms more significantly.[34] The number of peripheral sites will also increase, which has been related to increased activity as this is considered the site to which oxygen binds.

4.1.2. Hydrochlorination of Acetylene

Vinyl chloride, produced from the hydrochlorination of acetylene, is an important industrial chemical most commonly known for its use in the production of the polymer polyvinyl chloride. This is the third most important polymer in use today, particularly in the construction industries as a result of its high resistance to photo and chemical degradation.[35] Vinyl chloride is produced when HCl undergoes electrophilic addition across the acetylene triple bond. In the 1950s, vinyl chloride was produced commercially over a carbon supported mercuric chloride catalyst, but the catalyst deactivates rapidly, with the loss of mercury chloride.[36] Despite this, the availability

of coal in China has recently resulted in the commercial production of 13 million tonnes of vinyl chloride annually, using the mercury catalyst. Therefore, there is a lot of interest to diverge away from the volatile mercuric chloride catalyst. The reaction was expected to be a two electron process, involving donation to the metal cation from acetylene, and so gold was predicted to be an active catalyst as the metal cation of gold (Au^{3+}) has a high electrode potential. This prediction was confirmed, with the best catalyst prepared through an incipient wetness method, in which $HAuCl_4$ was dissolved in aqua regia.[30]

4.1.3. Selective Hydrogenation

In order to perform hydrogenation reactions, the metal in question must be able to chemisorb hydrogen. For the case of Au nanoparticles, only gold particles containing rough edges, in the form of edge, step or corner sites have the ability to chemisorb hydrogen molecules, and hence small Au particles promote activity.[37] The chemisorption process occurs at low temperatures; however, hydrogen is quickly desorbed upon heating.

One exciting area of research is in the transformation of CO and CO_2 to methanol, as this not only produces a useful chemical fuel, but replaces technologies that pump a lot more CO_2 into the atmosphere. Currently, the most active catalysts for the hydrogenation of CO and CO_2 to methanol are based around Cu/ZnO catalysts, with $Cu/ZnO/Al_2O_3$ already commercialised in the production of methanol from CO.[38] Au supported on various metal oxides have been investigated in the conversion of CO_2 to methanol, with only Au/ZnO exhibiting a comparable activity to that of a standard Cu/ZnO.[39-40] Of significance, smaller gold particle sizes gave higher methanol productivity per exposed surface area of gold.

4.1.4. Selective Oxidation of Alcohols

The selective oxidation of alcohols is an important reaction in the synthesis of fine chemicals. Aldehydes, a product formed in the selective oxidation of primary alcohols, are highly valuable components in the perfume industry.[41] Many oxidations of this type are performed using a stoichiometric amount of oxygen donors. Chromate or permanganate are traditional candidates which, however, produce a large amount of waste and cause serious toxicity problems.[42-43] There has therefore been substantial interest for the development of heterogeneous catalysts that use oxygen or hydrogen

peroxide, with oxygen the favoured candidate.[44] Polyols, compounds containing more than one alcohol group, are also target substrates for the oxidation reaction, but the reaction pathways usually lead to multiple products. The challenge is therefore to control and direct the oxidative pathway. There have been many studies published over the last 20 years using Au an effective catalyst for many alcohol substrates, with notable examples including benzyl alcohol and glycerol.[19, 25, 45]

4.2. Palladium Nanoparticles

Many reactions involving Pd are based around unsupported Pd nanoparticles, protected by dendrites or polymer stabilisers. However, for increased catalyst stability, including resistance to morphological changes and metal leaching, the Pd nanoparticles are immobilised on to a support material. The main reactions using supported Pd catalysts will be discussed here, including C-C coupling, hydrogenation and oxidation reactions.

4.2.1. C-C Cross Coupling

Palladium catalysts have played an important role in organic transformation for the past 40 years, and are well known for their application in the formation of carbon-carbon bonds. One type of reaction is termed the Suzuki reaction, which is the coupling of arylboronic acids with aryl halides, another is the Heck reaction, which is the coupling aryl halides with alkenes.[46] Commonly, phosphine coordinated organic complexes are used as effective catalysts, but an interesting alternative is to use heterogeneous catalysts for the ease at which they can be recycled, and the increased stability. There have therefore been efforts in preparing small, supported palladium nanoparticles, and immobilising them on to different supports. The successful preparation and utilisation in this reaction includes employing TiO_2 and carbon supported Pd nanoparticles.[47-48]

4.2.2. Selective Hydrogenation

Pd nanoparticles are well known to be active in hydrogenation reactions. The substrates of interest include unsaturated carbonyls and alkynes. The synthesis of a large number of fine chemicals, particularly in pharmaceutical and fragrance involves the selective hydrogenation of α,β-unsaturated carbonyls. Directing selectivity to produce either unsaturated alcohols or saturated carbonyls has received a lot of attention. α,β-unsaturated carbonyl compounds in which supported Pd nanoparticles

have been used to selectively hydrogenate either moiety include citral,[49] cinnamaldehyde[47] and furfural.[50]

4.3. Platinum Nanoparticles

4.3.1. Fuel Cell Electro-catalysts

The best known application of Pt nanoparticles is as an electro-catalyst in fuel cells. Fuel cells generate electrical energy from a chemical reaction, and have great potential to supply energy during energy demanding periods. Particular interest has focused on improving the slow cathodic oxygen reduction reaction (ORR) in the proton exchange membrane fuel cells (PEMFC), as well as improving the anode catalyst in direct alcohol fuel cells (DAFC), in which either methanol or ethanol feedstocks have been used. To improve the oxygen reduction reaction, efforts have been made not only to reduce the amount of Pt used, but to enhance catalytic activity and stability, which stems from optimising catalyst morphology, shape and composition.[51] In the case of direct methanol and ethanol fuel cells, monometallic Pt catalysts suffer from deactivation as a result of strongly bonded CO, and so much research is focused on bimetallic systems, using metal such as Ru and Sn to help remove CO.[52]

4.4. Silver Nanoparticles

4.4.1. Epoxidation

Ag nanoparticles have been extensively studied for the industrial production of both ethylene and propylene oxide. Although ethylene oxide is an unpleasant hazardous (carcinogenic and mutagenic) chemical for household use, it is used industrially in the production of detergents, thickeners, solvents and plastics.[53] Propylene oxide's major application is in the production of polyurethane plastics.[54] Both ethylene and propylene oxide are produced by direct epoxidation of the corresponding alkene using molecular oxygen, over supported Ag catalysts.[54] The selective production of ethylene oxide has shown to be dependent on both Ag particle size and shape. Interestingly, larger Ag particles were favourable, and efforts were made during the catalyst preparation to block low-coordinated sites with chlorine, to improve product selectivity.[53]

5. Aims and Objectives

The review thus far has not only highlighted the importance of designing metal nanoparticles and the typical preparation methods used to achieve this, but has also shown the use of supported noble metal based nanoparticles in current catalytic applications. The work presented in this thesis has two main aims; (1) optimising preparation methods to prepare metal nanoparticles with tailored properties for catalytic applications and (2) understanding the processes that occur during metal nanoparticle synthesis.

The sol-immobilisation method is the chosen preparation method as it has demonstrated the ability to tune the metal nanoparticle properties. Optimisation procedures include temperature and solvent variations, as well as investigating the continuous flow preparation of metal nanoparticles. A range of characterisation techniques will be employed to help determine the structure of the resulting metal nanoparticles and supported catalysts including infrared spectroscopy, electron microscopy and X-ray absorption spectroscopy, as well as computational studies to corroborate with experimental work. The supported metal catalysts are tested for their performance in both oxidation and hydrogenation reactions, with emphasis on defining structure/performance relationships.

Elucidating, and understanding the 'nucleation' and 'growth' processes that occur during metal reduction in colloidal metal synthesis is fundamental to the future design of metal nanoparticles. However, monitoring such processes is difficult, and so advanced techniques (synchrotron based) are used to study colloidal metal synthesis in a range of reactors, fabricated from different materials.

6. References

1. Sleight, A. W. *Science,* 1980**, *208*** (4446), 895-900.
2. Delmon, B. *Journal of Thermal Analysis and Calorimetry,* 2007**, *90*** (1), 49-65.
3. Bereau, P. R. *2016 World Population Data Sheet,* 2016.
4. Giordano, N.; Passalacqua, E.; Pino, L.; Arico, A. S.; Antonucci, V.; Vivaldi, M.; Kinoshita, K. *Electrochimica Acta,* 1991**, *36*** (13), 1979-1984.
5. Hvolbæk, B.; Janssens, T. V. W.; Clausen, B. S.; Falsig, H.; Christensen, C. H.; Nørskov, J. K. *Nano Today,* 2007**, *2*** (4), 14-18.
6. Ahmadi, T. S.; Wang, Z. L.; Green, T. C.; Henglein, A.; El-Sayed, M. A. *Science,* 1996**, *272*** (5270), 1924-1925.
7. Tao, A. R.; Habas, S.; Yang, P. D. *Small,* 2008**, *4*** (3), 310-325.
8. Li, Y.; Liu, Q.; Shen, W. *Dalton Transactions,* 2011**, *40*** (22), 5811-5826.
9. Haruta, M.; Date, M. *Applied Catalysis a-General,* 2001**, *222*** (1-2), 427-437.
10. Cuenya, B. R. *Thin Solid Films,* 2010**, *518*** (12), 3127-3150.
11. Dicks, A. L. *Journal of Power Sources,* 2006**, *156*** (2), 128-141.
12. Ni, M.; Leung, M. K. H.; Leung, D. Y. C.; Sumathy, K. *Renewable and Sustainable Energy Reviews,* 2007**, *11*** (3), 401-425.
13. Julkapli Nurhidayatullaili, M.; Bagheri, S., Magnesium oxide as a heterogeneous catalyst support. In *Reviews in Inorganic Chemistry*, 2016; Vol. 36, p 1.
14. Campelo, J. M.; Luna, D.; Luque, R.; Marinas, J. M.; Romero, A. A. *ChemSusChem,* 2009**, *2*** (1), 18-45.
15. Delannoy, L.; El Hassan, N.; Musi, A.; Le To, N. N.; Krafft, J.-M.; Louis, C. *The Journal of Physical Chemistry B,* 2006**, *110*** (45), 22471-22478.
16. Campanati, M.; Fornasari, G.; Vaccari, A. *Catalysis Today,* 2003**, *77*** (4), 299-314.
17. Zanella, R.; Giorgio, S.; Henry, C. R.; Louis, C. *The Journal of Physical Chemistry B,* 2002**, *106*** (31), 7634-7642.
18. Li, W. C.; Comotti, M.; Schuth, F. *Journal of Catalysis,* 2006**, *237*** (1), 190-196.
19. Dimitratos, N.; Villa, A.; Prati, L.; Hammond, C.; Chan-Thaw, C. E.; Cookson, J.; Bishop, P. T. *Applied Catalysis A: General,* 2016**, *514***, 267-275.
20. Shan, J.; Tenhu, H. *Chemical Communications,* 2007**,** (44), 4580-4598.
21. Xiong, Y.; Washio, I.; Chen, J.; Cai, H.; Li, Z.-Y.; Xia, Y. *Langmuir,* 2006**, *22*** (20), 8563-8570.
22. Zhou, Q. F.; Bao, J. C.; Xu, Z. *Journal of Materials Chemistry,* 2002**, *12*** (2), 384-387.
23. Jia, C.-J.; Schuth, F. *Physical Chemistry Chemical Physics,* 2011**, *13*** (7), 2457-2487.
24. DiScipio, R. G. *Analytical Biochemistry,* 1996**, *236*** (1), 168-170.

25. Dimitratos, N.; Porta, F.; Prati, L. *Applied Catalysis A: General,* 2005**,** ***291*** (1–2), 210-214.
26. Prati, L.; Martra, G. *Gold Bulletin,* 1999**,** ***32*** (3), 96-101.
27. Kim, E. J.; Yeum, J. H.; Choi, J. H. *Journal of Materials Science & Technology,* 2014**,** ***30*** (2), 107-111.
28. Bond, G. C.; Sermon, P. A.; Webb, G.; Buchanan, D. A.; Wells, P. B. *Journal of the Chemical Society, Chemical Communications,* 1973**,** (13), 444b-445.
29. Haruta, M.; Kobayashi, T.; Sano, H.; Yamada, N. *Chemistry Letters,* 1987**,** ***16*** (2), 405-408.
30. Hutchings, G. J. *Journal of Catalysis,* 1985**,** ***96*** (1), 292-295.
31. Hashmi, A. S. K.; Hutchings, G. J. *Angewandte Chemie-International Edition,* 2006**,** ***45*** (47), 7896-7936.
32. Haruta, M.; Tsubota, S.; Kobayashi, T.; Kageyama, H.; Genet, M. J.; Delmon, B. *Journal of Catalysis,* 1993**,** ***144*** (1), 175-192.
33. Haruta, M.; Daté, M. *Applied Catalysis A: General,* 2001**,** ***222*** (1–2), 427-437.
34. Okazaki, K.; Ichikawa, S.; Maeda, Y.; Haruta, M.; Kohyama, M. *Applied Catalysis a-General,* 2005**,** ***291*** (1-2), 45-54.
35. Johnston, P.; Carthey, N.; Hutchings, G. J. *Journal of the American Chemical Society,* 2015**,** ***137*** (46), 14548-14557.
36. Hutchings, G. J.; Grady, D. T. *Applied Catalysis,* 1985**,** ***16*** (3), 411-415.
37. Juliusa, M.; Robertsa, S.; Fletchera, J. Q. *Gold Bulletin,* 2010**,** ***43*** (4), 298-306.
38. Bowker, M.; Hadden, R. A.; Houghton, H.; Hyland, J. N. K.; Waugh, K. C. *Journal of Catalysis,* 1988**,** ***109*** (2), 263-273.
39. Sakurai, H.; Tsubota, S.; Haruta, M. *Applied Catalysis A: General,* 1993**,** ***102*** (2), 125-136.
40. Sakurai, H.; Haruta, M. *Catalysis Today,* 1996**,** ***29*** (1–4), 361-365.
41. Villa, A.; E-Chan-Thaw, C.; Schiavoni, M.; Campisi, S.; Wang, D.; Prati, L. *Chinese Journal of Catalysis,* 2014**,** ***35*** (6), 945-951.
42. Kimbrough, D. E.; Cohen, Y.; Winer, A. M.; Creelman, L.; Mabuni, C. *Critical Reviews in Environmental Science and Technology,* 1999**,** ***29*** (1), 1-46.
43. Enache, D. I.; Edwards, J. K.; Landon, P.; Solsona-Espriu, B.; Carley, A. F.; Herzing, A. A.; Watanabe, M.; Kiely, C. J.; Knight, D. W.; Hutchings, G. J. *Science,* 2006**,** ***311*** (5759), 362-365.
44. Sheldon, R. A.; Arends, I. W. C. E.; Dijksman, A. *Catalysis Today,* 2000**,** ***57*** (1–2), 157-166.

45. Dimitratos, N.; Lopez-Sanchez, J. A.; Morgan, D.; Carley, A. F.; Tiruvalam, R.; Kiely, C. J.; Bethell, D.; Hutchings, G. J. *Physical Chemistry Chemical Physics,* 2009***, 11*** (25), 5142-5153.

46. Li, Y.; El-Sayed, M. A. *Journal of Physical Chemistry B,* 2001***, 105*** (37), 8938-8943.

47. Corma, A.; Garcia, H.; Leyva, A. *Journal of Molecular Catalysis a-Chemical,* 2005***, 230*** (1-2), 97-105.

48. Chen, X.; Hou, Y.; Wang, H.; Cao, Y.; He, J. *The Journal of Physical Chemistry C,* 2008***, 112*** (22), 8172-8176.

49. Aramendia, M. A.; Borau, V.; Jimenez, C.; Marinas, J. M.; Porras, A.; Urbano, F. J. *Journal of Catalysis,* 1997***, 172*** (1), 46-54.

50. Pang, S. H.; Schoenbaum, C. A.; Schwartz, D. K.; Medlin, J. W. *ACS Catalysis,* 2014***, 4*** (9), 3123-3131.

51. Bing, Y. H.; Liu, H. S.; Zhang, L.; Ghosh, D.; Zhang, J. J. *Chemical Society Reviews,* 2010***, 39*** (6), 2184-2202.

52. Liu, H. S.; Song, C. J.; Zhang, L.; Zhang, J. J.; Wang, H. J.; Wilkinson, D. P. *Journal of Power Sources,* 2006***, 155*** (2), 95-110.

53. Christopher, P.; Linic, S. *Chemcatchem,* 2010***, 2*** (1), 78-83.

54. Lei, Y.; Mehmood, F.; Lee, S.; Greeley, J.; Lee, B.; Seifert, S.; Winans, R. E.; Elam, J. W.; Meyer, R. J.; Redfern, P. C.; Teschner, D.; Schlogl, R.; Pellin, M. J.; Curtiss, L. A.; Vajda, S. *Science,* 2010***, 328*** (5975), 224-228.

Chapter Two. Materials and Methods

The following section will firstly detail the catalyst preparation method used during this study, sol-immobilisation. All techniques used to characterise the prepared metal sols and solid catalysts will be described, including UV-Vis spectroscopy, TEM, XAFS, IR spectroscopy, and to a lesser extent MP-AES, STEM HAADF, XRD, XRF and chromatography. Finally, the catalytic experiments that have been performed will be summarised and discussed.

1. Reagents and Materials

The supplier of all the reagents and materials used within the study are detailed in table 1.

Table 1. List of reagents/materials and the subsequent supplier.

Reagent	Supplier
$HAuCl_4.3H_2O$ (> 99.99 %)	Aldrich
K_2PdCl_4 (99.99 %)	Aldrich
$AgNO_3$ (99.99 %)	Aldrich
K_2PtCl_4 (99.99 %)	Aldrich
TiO_2 (P25)	Aeroxide (Evonik)
Sodium borohydride (> 96 %)	Aldrich
Poly(vinyl) alcohol M_w = 9000-10 000 g mol^{-1}	Aldrich
Concentrated sulphuric acid	Aldrich
Acetone	Aldrich
Ethanol (> 99.99 %)	Fisher
Dry ice (carbon dioxide)	BOC
Glycerol (> 99.5 %)	Riedel-de haën
Furfural (> 99 %)	Aldrich
p-Nitrophenol (99 %)	Aldrich

2. The Sol-immobilisation Method

The method employed for metal nanoparticle generation is based on colloidal routes, in which zero-valent metal is stabilised in solution by the presence of a protecting agent. The subsequent metal nanoparticles are anchored on to a support material to yield the final catalyst, the overall process known as the sol-immobilisation method. The use of polyvinyl alcohol (PVA) as stabilising agent has demonstrated that metal nanoparticles can be prepared with a narrow particle distribution, with the average metal particle size dependent on the stabilising/metal ratio. The structure of PVA is illustrated in figure 1, with the 200-230 repeating units for the PVA used in this study (molecular weight = 9-10000 g mol^{-1}).The large polymer structure acts to stabilise metal nanoparticles through steric, rather than electrostatic interactions. The support material used for the catalysts prepared in this thesis was commercial P25 Titanium dioxide (TiO_2), which is a mixture of Anatase and Rutile phases in the ratio of ~ 80:20. This material was chosen as the support material because it is chemically stable, exhibits a strong metal-support interaction, has a respectable surface area (52 m^2 g^{-1}), and is suited to a wide range of catalytic applications. The ease at which the metal nanoparticles can be anchored on to the support without themselves undergoing any chemical change also makes TiO_2 favourable.

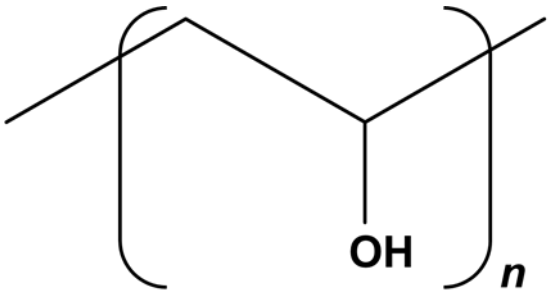

Figure 1. The monomer unit in the polymer, polyvinyl alcohol (PVA), where *n* is the number of repeating units (200-230 for a polymer with a molecular weight of 9-10000 g mol^{-1}).

2.1. The Sol-immobilisation Synthesis Procedure

TiO_2 supported metal nanoparticles were prepared by applying modifications to an established standard sol-immobilisation method.[1-3] Temperature control as well as different solvent systems were employed during the preparation. Different solvent

environments (methanol, ethanol and 1-propanol) have been previously investigated for the preparation of polyvinyl pyrrolidone (PVP) stabilised Pd particles.[4] It was observed that the Pd particle size remains small until an alcohol/water ratio greater than 50 % by volume is used, causing a sharp rise in Pd particle size. However, solvent and temperature effects during the preparation of PVA stabilised metal nanoparticles has not yet been investigated, with particular interest in temperatures at zero and sub-zero.

The metal salt precursor was used to prepare solutions with various H_2O/EtOH ratios with the desired metal concentration (1.26 x 10^{-4} M), to which the same solvent solutions of PVA (1 wt. % solution) were added (PVA/metal wt. ratio = 0.65). $NaBH_4$ (0.1 M, $NaBH_4$/metal molar ratio = 5) were freshly prepared in the respective solvent and added drop-wise to form a sol. After 15-30 minutes of sol generation, depending on the temperature, the colloid was immobilised onto TiO_2 under vigorous stirring conditions (acidified to pH 1-2 with sulphuric acid). For the catalysts prepared in this thesis, the amount of support material required was calculated so as to have a final metal loading of 0.2 or 1 wt. %, and is specified in each chapter. After 60 minutes the slurry was filtered and washed thoroughly with distilled water (18.2 Ω cm^{-2} Milli-Q) to remove all the unwanted chemical species such as Na^+, Cl^- and excess PVA, before it was left to dry at room temperature overnight. The general procedure of metal nanoparticle synthesis is illustrated in figure 2.

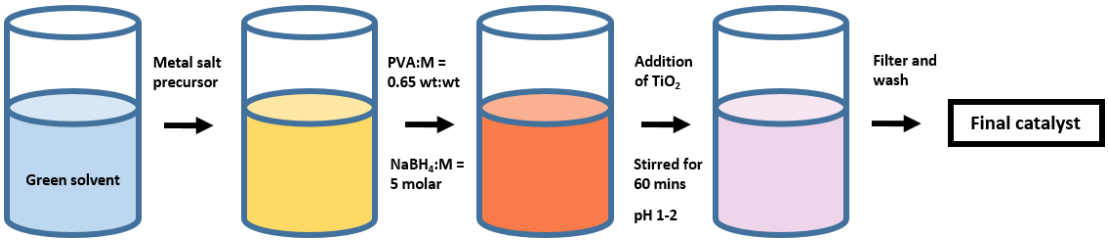

Figure 2. An illustration of the sol-immobilisation technique used for the preparation of TiO_2 supported metal nanoparticle catalysts.

In order to achieve temperatures below 0°C, mixed H_2O/EtOH solvents were used. A dry ice/acetone bath with different ratios of each component were employed to achieve temperatures down to −75°C, with aluminium foil wrapped around the system to help maintain temperature. Additional dry ice was used to maintain temperature throughout the synthesis. For temperatures at 1°C, a water ice bath with aluminium foil was used

which, once at temperature, remained stable throughout the synthesis. For temperatures higher than room temperature, a hot plate with a thermocouple was used to maintain the temperature. Again, the beaker was surrounded with foil to help distribute the heat evenly throughout the mixture.

3. Ultra Violet-Visible (UV-Vis) Spectroscopy

This method refers to absorption or reflectance spectroscopy in the 200-800 nm region of the electromagnetic spectrum. Molecules containing π-electrons or non-bonding electrons undergo electronic transitions upon exposure to UV-Visible light, promoting an electron from ground to excited state. One of the most widely used methods for characterising the optical and electronic structure of metal nanoparticles is through UV-Vis spectroscopy. For metals that possess a plasmon-resonance band, such is the case with Au, Ag and Cu, it can be an indicative tool towards the metal particle size based on the intensity and position of the band during the sol formation.[5-8] The plasmon resonance arises due to free conduction electrons oscillating as a consequence of induced electromagnetic radiation interaction.[9] The SPR band appears in the range 400-600 nm, depending on the metal, with increasing particle size causing a red shift, and increased particle distribution causing band broadening. Not only particle size affects the plasmon resonance, as other factors including solvent and surface functionalization can contribute to the exact frequency and intensity of the band.[10] Whether the metal possesses a plasmon resonance band or not, such is the case with palladium, the technique is useful to follow the reduction process from a metal salt, to metal nanoparticle during the sol-immobilisation process.

The quantitative determination of highly conjugated organic compounds can be performed using UV-Vis spectroscopy. The Beer-Lambert law states that the absorbance of a solution is directly proportional to the concentration of the absorbing species in the solution and the path length, according to equation 1.

$$A = \varepsilon cl \qquad \textbf{Equation 1}$$

Where A = absorbance, ε = molar extinction coefficient (M^{-1} cm^{-1}), c = concentration (M) and l = path length (cm). The molar extinction coefficient can be calculated by maintaining the same path length whilst varying the concentration of analyte to

establish a calibration curve. A plot of absorbance against concentration will yield a slope equal to the ε.

All UV-Vis spectroscopic measurements were performed with a Shimadzu UV-1800 spectrometer using either quartz or polystyrene cuvettes. The solvent (18.2 Ω cm^{-2} Milli-Q H_2O) was used to perform the baseline/background measurement.

4. Microwave Plasma – Atomic Emission Spectroscopy (MP-AES)

MP-AES is used for accurate elemental analysis, with detection limits of parts per million (ppm), and was used to determine the elemental compositions of the prepared catalysts. The technique works by employing microwave energy, in the GHz range, to produce a plasma discharge, using nitrogen, which can be obtained from ambient air. Samples are typically nebulized prior to interaction with the plasma in MP-AES measurements. The atomized sample passes through the plasma, resulting in the promotion of electrons to the excited state. The light emitted electrons return back to the ground state, resulting in a characteristic emission line, which can be measured at the detector. Analysis was performed using an Agilent 4100 series spectrometer.
Solid samples must undergo a digestion procedure, which essentially involves the dissolution of all solid sample using acids, with the exact experimental protocol used as follows: the solid samples (0.1 g) were digested in aqua regia (3:1 HCl:HNO_3, 8 ml) using an Anton Paar Multiwave 3000. The samples were heated to 200°C at 12°C per minute and held for 40 minutes before being cooled to 20°C. Samples were then removed from the digester and diluted in deionised water to form a 0.1 wt. % solution. Metal standards were used to calibrate the machine and H_2O was used as a 'blank' measurement.

5. Transmission Electron Microscopy (TEM)

TEM succeeds in directly observing the morphology of the catalyst surface on the nanometre scale, with the metal nanoparticle size and distribution the key characteristics to obtain. Metal nanoparticles generated by the sol-immobilisation method are typically below 10 nm, and so it is not possible to image them using a conventional light microscope, but they are visible with a TEM. The comparable resolutions achieved by both light and electron microscopes are attributed to the

different wavelengths of light photons and electrons. The typical wavelength of a light photon is 400-700 nm, limiting the resolution to this range. However, the de Broglie equation describes electrons to have both wave and particle properties, and it is the wave-like property enables electrons to be used for high resolution imaging.[11] De Broglies wavelength can be expressed using the equation as follows:

$$\lambda = \frac{h}{\rho} \qquad \textbf{Equation 2}$$

Where λ is the wavelength of the particle, h is Plancks constant (6.626×10^{-34} J s) and ρ is the momentum of the particle (mass x velocity).

By adjusting the electron velocity, the appropriate wavelength for TEM can be obtained. An illustration of a TEM is shown in figure 3. The operation of the TEM involves the use of a filament (or electron gun) emitting electrons from the top of a vacuumed column (~ 10^{-5} mbar), where they are focused on to the specimen by a series of electromagnetic lenses (condenser lenses). The energy of the electron beam is typically 200 keV, and the vacuum enables the beam to travel without interference from air molecules.[12] Depending on the thickness and atomic number of the elements in the specimen of interest, there will be a different level of interaction, with some of the electrons either being absorbed or scattered. After sample interaction, projection lenses spread the beam on to a fluorescent screen. The specimen can be viewed on this screen, and is used to manually align and focus the instrument. The microscope is also fitted with a charged coupled device (CCD) camera in order convert the electron intensity into a digital image. Generally, the samples were viewed in bright field imaging mode, in which the specimen appears darker, dependent on the sample thickness and atomic number of the elements in the specimen, and regions with no sample will appear bright. A second operational mode is dark field imaging, in which the scattered electron beam after interaction with the sample is detected and processed to an image in which the sample appears bright, on a dark background. Samples for examination by TEM were prepared by dispersing the catalyst powder (~ 5 mg) in high purity ethanol (~ 2 mL) using ultra-sonication, then allowing a drop of the suspension (~ 40 µl) to evaporate on a holey carbon film supported by a 300 mesh copper grid. TEM was performed by myself unless otherwise stated, using a JEOL JEM 2100 model microscope, at the Research Complex at Harwell. Particle size distributions

were calculated using a post processing programme, ImageJ, which is available from the RSB website.[13] For each image the scale bar was used as a reference to transform the scale in to image pixels per nm. Using the line tool, the diameter of each particle was manually picked, and the resulting metal particle size displayed in an output file (excel). The procedure was repeated across 300 particles before the average diameter was calculated from the output file.

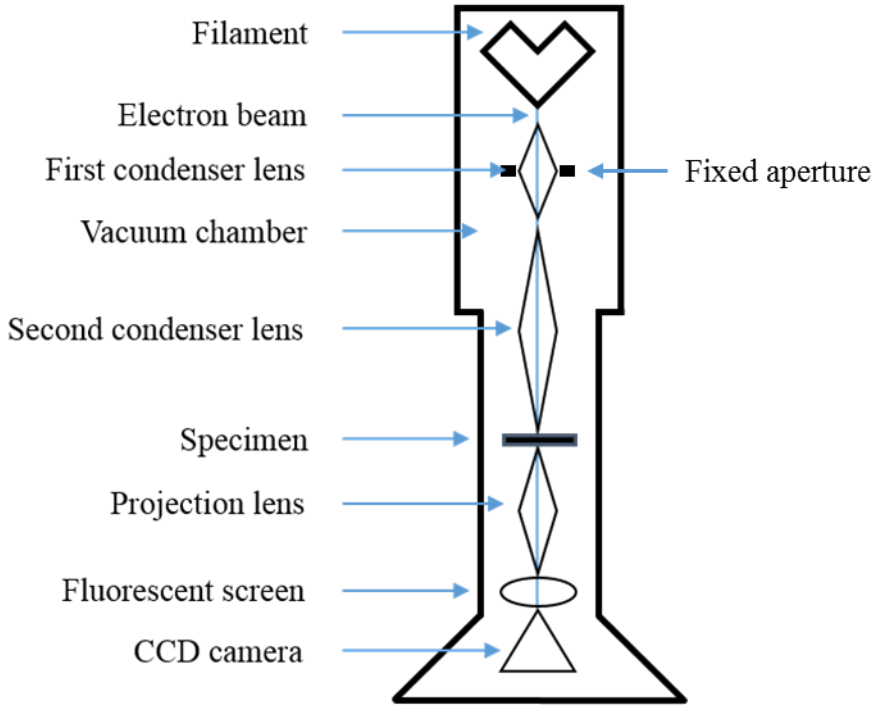

Figure 3. Schematic set up of a TEM column operating in bright field mode.

5.1. Scanning TEM High Angle Annular Dark Field (STEM HAADF) Microscopy

For high resolution analysis of small metal clusters, samples were sent to the Nanoscale Physics Research Laboratory at the University of Birmingham for analysis using STEM HAADF microscopy. In scanning TEM, the electron beam is focused into a narrow spot which is subsequently scanned over the sample in a raster. This mode can be coupled with a high angle detector to form atomic resolution images. The detector operates by detecting the electrons that are scattered at high angles, rather than the Bragg scattered electrons (figure 4). The atomic number of the scattering atoms (Z number) is more influential to the image created, with heavier atoms scattering more electrons, resulting in brighter regions amongst a dark background.[12] The samples for STEM HAADF were examined using a JEOL JEM 2100F STEM model. The

integrated HAADF STEM intensity was used to obtain the size of ultra-small clusters, with the intensity taken from larger clusters, with a known number of metal atoms, functioning as reference.[14]

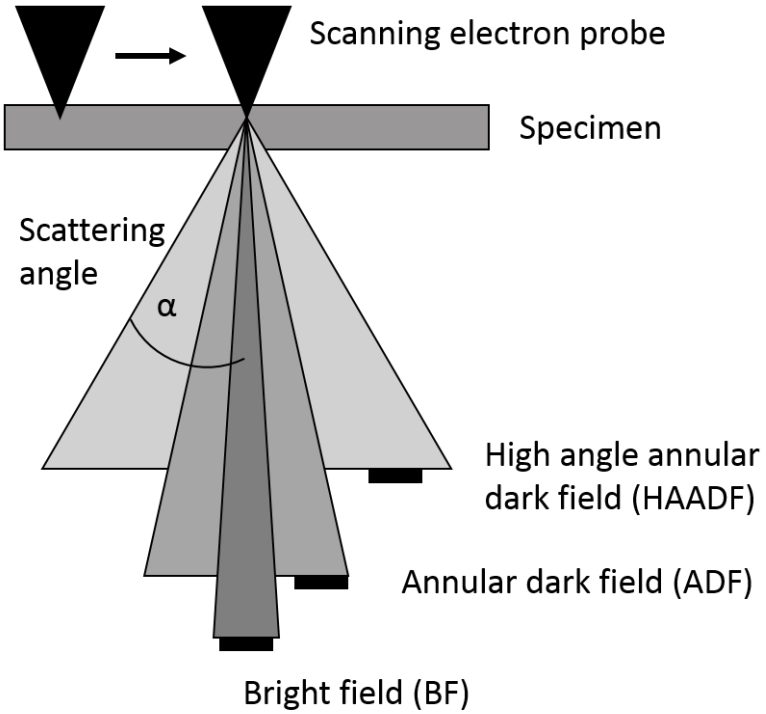

Figure 4. Illustration of the types of modes available depending on the extent of electron scattering from the sample.[12]

6. Infra-red (IR) Spectroscopy

The infra-red region of the electromagnetic spectrum, between that of the visible and microwave range, is commonly employed for functional group identification in both organic and inorganic compounds. IR was used in this study to assess the catalyst surface, in particular the available metal nanoparticle sites (linear or bridge sites) and the electronic properties of the metal. It is possible to use an IR active surface adsorbed probe molecule to obtain crucial information, by assessing the band intensities and wavelength shifts.[15] CO is a common probe molecule due to the characteristic IR bands in the region 1800-2200 cm^{-1}. Spectra are assignable due to the shifts in frequency of the bands as a result of increased/decreased electron density occupying the π^* anti-bonding orbital of the CO molecule.[16]

IR spectroscopy was collected in two different modes, namely transmission or diffuse reflectance. Transmission experiments rely on the sample to be able to transmit the infrared radiation, and so sample preparation involves pelletizing the minimal amount of sample, which can be a disadvantage, depending on the material. Diffuse Reflectance Infra-red Fourier Transform Spectroscopy (DRIFTS) is an invaluable analysis tool for investigating the chemical and physical structures of materials in which transmission experiments are not viable (i.e. samples that are too absorbing). It is particularly useful for *in situ* analysis, due to the ease to which the local sample environment can be controlled.[17-18]

Many processes occur when radiation interacts on to the specimen's surface, including absorption, specular reflection, internal reflection or diffusion in all directions. Diffuse reflection spectroscopy relies on the latter effect. Diffuse specular reflection involves multiple reflections without penetrating the sample, whereas true diffuse reflection is a consequence of beam penetration into one or more particles. Although radiation exits the sample at any angle, it contains data on the absorption properties of the material. This phenomena enables many different materials to be examined, so long as they do not fully absorb the IR beam, such as carbonaceous materials. The beam pathway in DRIFTS is illustrated in figure 5, in which mirrors are used to direct the beam through the sample and to the detector.[19]

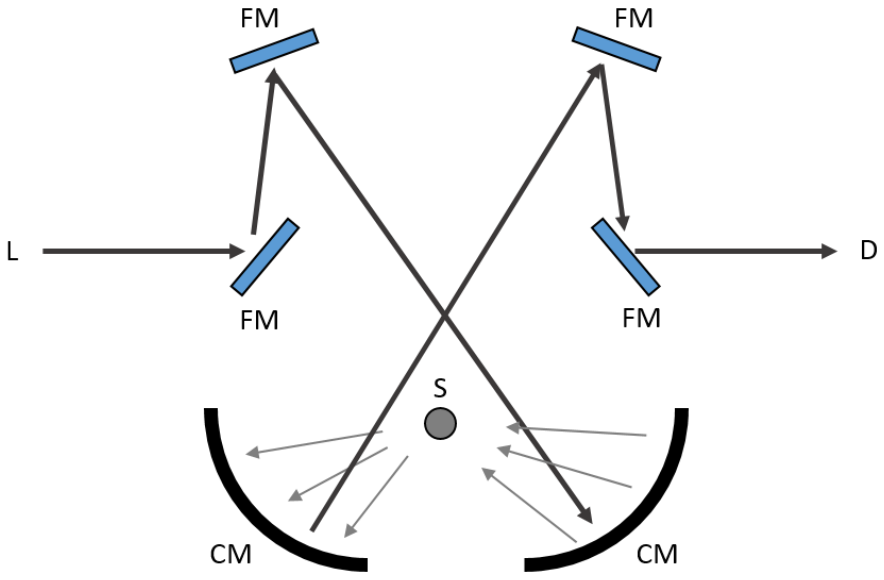

Figure 5. Illustration of the beam path in a diffuse reflectance accessory. L, light source; D, detector; S, sample; FM, flat mirror; CM, curved mirror.

6.1. DRIFTS Experimental Procedure

FTIR spectra were obtained with an Agilent Cary 680 spectrometer and Mercury Cadmium Telluride (MCT) detector cooled with liquid nitrogen. Spectra were acquired at a spectral resolution of 2 cm^{-1} and accumulating up to 64 scans. For each experiment, the catalyst was placed in the sample holder and smoothed to leave a flat surface. The cell and catalyst were then purged with helium for 30 minutes to obtain a background spectrum of the catalyst. Carbon monoxide was introduced using a 10 % CO/He mixture at a flow rate of 30 cm^3 min^{-1} over a 5 minute period. The CO was switched off and helium passed over the catalyst surface, for 30 minutes, at a flow rate of 30 cm^3 min^{-1} in order to remove gaseous and physisorbed CO. A second spectrum was acquired. In order to observe the bands responsible for CO adsorbed on metal sites, a subtraction of the background spectrum from the second spectrum was performed.

6.2. Transmission IR Experimental Procedure

Fourier Transform (FT) transmission IR spectra were obtained with an is10 Nicolet spectrometer equipped with a deuterated triglycine sulfate (DTGS) detector at a spectral resolution of 2 cm^{-1} and accumulating up to 64 scans. For each experiment, ~ 25 mg of catalyst was pressed to form a self-supported wafer (1.3 cm^2). The pellet was carefully placed in the gas sealed Harrick cell, which was subsequently purged with Helium for 30 minutes to obtain a background spectrum before CO was introduced using a 10 % CO/He mixture at a flow rate of 70 cm^3 min^{-1} over a 30 second period. Three CO doses of this nature were administered for each experiment. The gas was switched to Helium for 30 minutes, at a flow rate of 70 cm^3 min^{-1}, in order to remove gaseous and physisorbed CO from the catalyst surface before a spectrum was then obtained. Subtraction of the background resulted in a spectrum containing bands responsible for CO adsorption.

7. X-ray Diffraction (XRD)

This analytical technique is commonly used for phase identification, as well as providing information of the crystallite size, shape and atomic spacing in the material. The prepared catalysts are powders, consisting of small crystallites with random

orientations. Statistically, one or more crystals will be in the correct orientation so that the Bragg's law can be satisfied. As the powder consists of small particles randomly orientated all diffraction angles will be represented. For diffraction experiments a monochromatic source of X-rays should be used, with wavelength similar to the inter-planar spacing.[20]

The Scherrer equation (equation 3) can be used to estimate an average crystallite size from powder XRD. As the particle size increases, the diffraction lines narrow, and vice versa. By fitting a Gaussian peak to the diffraction line, the full width half maximum (FWHM) can be obtained and applied to calculate the crystallite size.

$$\langle L \rangle = \frac{K\lambda}{\beta \cos\theta} \qquad \textbf{Equation 3}$$

Where ⟨L⟩ is the mean particle (crystallite) size, λ is the X-ray wavelength, β is the peak width (FWHM) in degrees, θ is the Bragg angle and K is a constant associated with crystallite shape (often taken as 0.9).

Powder XRD was performed at the Materials Characterisation Laboratory at ISIS, Harwell with a Miniflex 600 spectrometer. The powdered sample was placed in an aluminium holder and flattened until smooth. The operating conditions were typically 2θ range = 5-90°, scan step size = 0.02 deg, and scan speed = 5 mdeg min^{-1}.

8. X-ray Fluorescence (XRF)

X-ray fluorescence is an analytical technique used to determine the elemental composition of materials. The details of how the technique works are as follows: A beam of X-rays (primary) is directed at the samples surface. If the energy of an X-ray is high enough, the interaction with an atom will eject a core electron and create a vacancy. To restore atom stability, an electron from a higher energy level falls in to the electron vacancy, and the excess energy between the two levels is released in the form of an emitted X-ray (secondary). The intensity and energy of the secondary X-ray is measured at the detector, with the latter characteristic to each element. XRF was performed at beamline I18 at Diamond Light Source, Didcot, U.K, in conjunction with an X-ray spectroscopy experiment.

9. X-ray Absorption Spectroscopy (XAS)

X-ray absorption spectroscopy is a powerful technique used in the structural characterisation of materials without long range order, and gives a good representation of the whole sample. The technique is divided into two sections, X-ray Absorption Near Edge Structure (XANES) and Extended X-ray Absorption Fine Structure (EXAFS), both of which will be explained. XANES provides information about the oxidation states and local coordination geometry. EXAFS is a useful technique to probe the local structure, gaining important information on the coordination and radial distribution to neighbouring atoms.

9.1. XAS: The Theory

In XAS experiments the attenuation of X-rays through a material is proportional to the incident energy (I_o), and can be investigated over a path length (x) as shown:

$$dI = -\mu I_o dx \qquad \textbf{Equation 4}$$

Where μ is the absorption coefficient, a function of the photon energy, E. After integration over the path length, x, the Beer Lambert equation is obtained:

$$I = I_o e^{-\mu E x} \qquad \textbf{Equation 5}$$

Where I is the intensity of X-rays transmitted. There is a decrease in absorption of the X-rays with increasing incident energy until such an energy is reached, that is a feature known as the absorption edge. At this specific energy there is a sudden increase in X-ray absorption, corresponding to the excitation of a core electron into an excited state or continuum. The position of the absorption edge is dependent on the principle quantum number of the orbital from which the electron is ejected. This process is known as the photoelectron effect in which the ejected photoelectron is released with kinetic energy, E_k:

$$E_k = hv - E_{binding} \qquad \textbf{Equation 6}$$

The outgoing photoelectron is described as a spherical wave function, with wave vector, k.

$$k = \sqrt{\left(\frac{8\pi^2 m_e}{h^2}\right)(h\nu - E_o)} \qquad \textbf{Equation 7}$$

Where m_e = electron mass, E_o = zero point energy.

The outgoing wave can experience backscattering off neighbouring atoms, and as a result the final state wave function must be taken in to account, which is a sum of both the outgoing and backscattered waves.

$$\varphi_{final} = \varphi_{outgoing} + \varphi_{backscattered} \qquad \textbf{Equation 8}$$

The type and extent of interference that results between the two waves determines the variation in the total absorption coefficient as shown in figure 6, and gives rise to the EXAFS, which can extend up 1000 eV past the absorption edge, as shown in figure 7.[20]

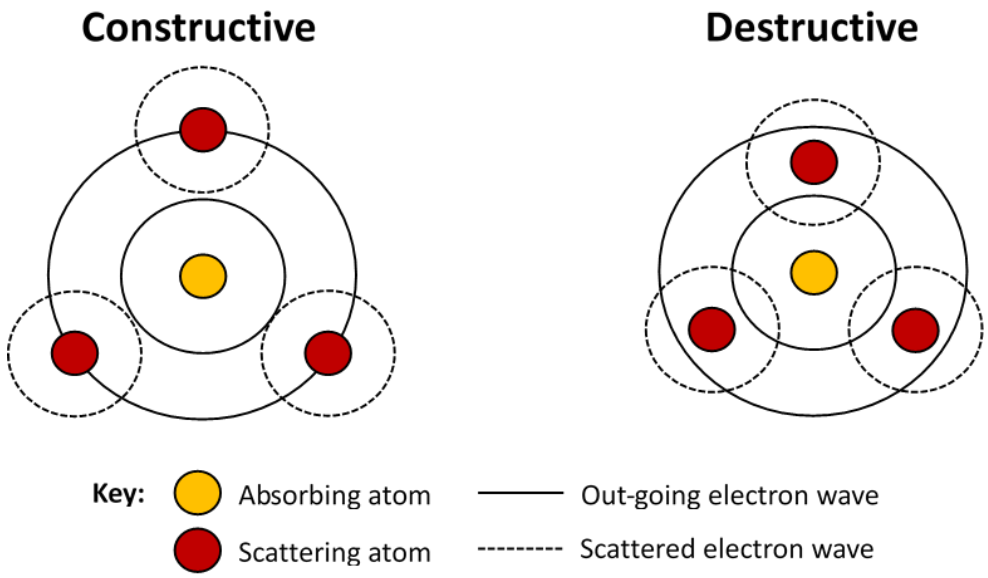

Figure 6. The different interference patterns arising that contribute to the final total absorption coefficient.

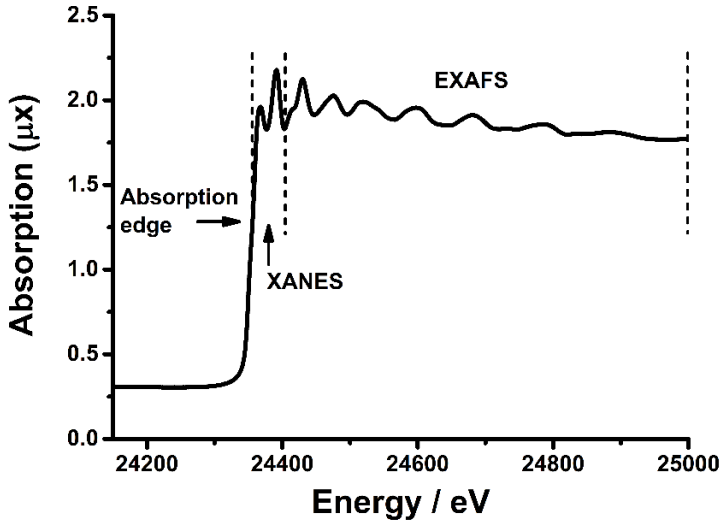

Figure 7. XAS spectrum of a Pd foil at the Pd K edge.

The oscillations in the EXAFS are given by χ, the normalized part of μ, in which the absorption of a free atom as result of elastic and inelastic X-ray scatter (μ_o) has been subtracted. The EXAFS signal, $\chi(k)$ can be obtained as a function of the wave vector, k:

$$\chi(k) = \frac{(\mu - \mu_o)}{\mu_o} \qquad \textbf{Equation 9}$$

The EXAFS function, $\chi(k)$ consists of an amplitude term and phase component, which can be expressed in the standard EXAFS equation as shown below.[21]

$$k\chi(k) = S_0^2 \sum_i \frac{N_i A_i}{r_i^2} e^{\left(\frac{-2r_i}{\lambda}\right)} e^{(-2\sigma_i^2 k^2)} sin[2kri + 2\Phi_i(k)] \qquad \textbf{Equation 10}$$

Where S_0^2 is the amplitude reduction factor; *Ni* is the number of atoms of type *i* at distance *ri* from the absorber atom; $e^{(-2\sigma_i^2 k^2)}$ is the Debye Waller term; σ_i^2 is the relative mean squared disorder along the distance between the absorbing and scattering atoms, *i*; A_i is the is the amplitude from the backscattered atom; $e^{\left(\frac{-2r_i}{\lambda}\right)}$ is a measure of the finite lifetime of the excited state, with λ the mean free path of the photoelectron; and $sin[2kri + 2\Phi_i(k)]$ contains the phase component with Φ_i defined as the phase shift.[22]

XANES deals with the region to about 50 eV past the main absorption edge of the edge of interest (figure 6). The interpretation of this region is difficult due to the complexity as a result of effects such as multiple scattering and distortions of the excited state contributing to the spectrum.

9.2. Data Analysis

Data processing was performed using the IFEFFIT software with the Horae package (Athena and Artemis).[23-24] The raw XAS spectra for a single sample were exported in to Athena, and ensuring there are no glitches in the data, merged to produce one spectrum. The first processing step is to remove the parabolic background by fitting pre- and post-edge lines to the spectrum. This normalises the intensity scale to an edge jump value of one (figure 8A). The E_0 value is set to 0 eV relative to the energy scale, and this is achieved by plotting the XAS spectrum as the first differential, and taking E_0 as the maximum of the first derivative (figure 8B). The contribution due to absorption of a free atom, u_0, is removed by applying a spline. The resulting oscillations in the chi plot should have even amplitude either side of the x-axis (figure 8C). After performing a Fourier transform of the chi plot, a pseudo-radial distribution plot will be produced, reflecting the neighbouring atoms surrounding the absorber (figure 8D).

Artemis is a software package used to calculate values for the coordination numbers, radial distances and the mean square disorder parameter. Refinement of these values is possible, with the R factor an indication of the quality of the fit. An R factor value between 20-30 % is considered acceptable.

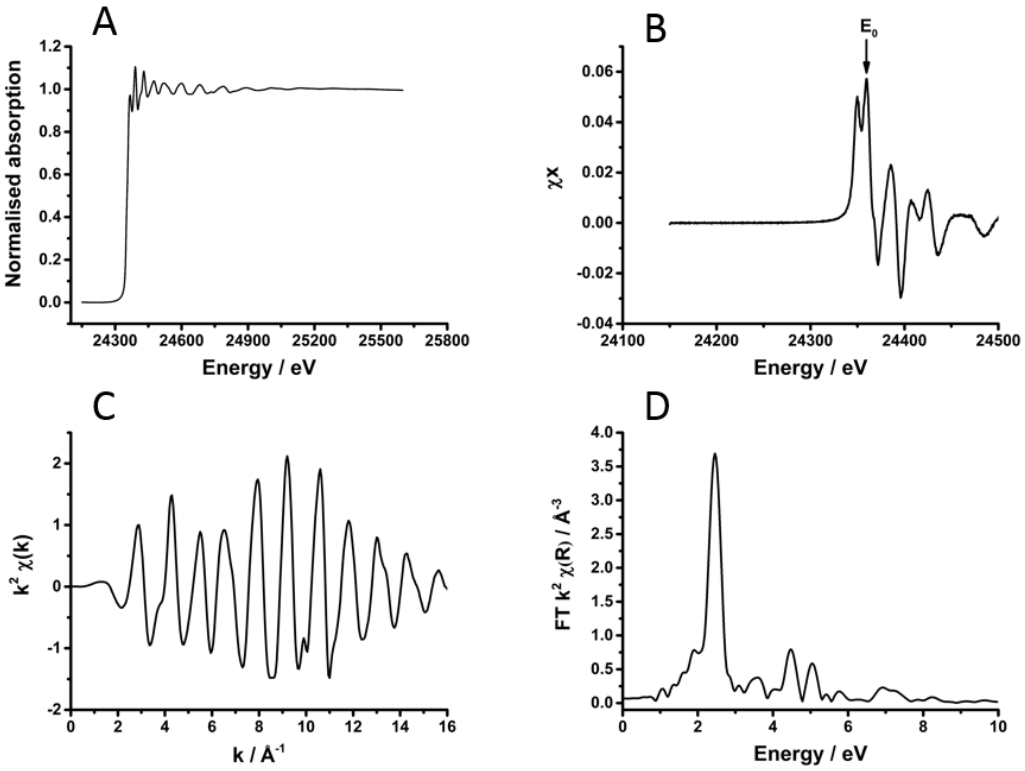

Figure 8. A) Normalised XAS data, B) E_0 identification using the first derivative, C) chi data and D) corresponding Fourier transform data.

9.3. Transmission Mode

Performing XAS in transmission mode is the simplest method to acquire high quality data. This relies upon measuring the X-ray absorption as the energy of the incident photons increases. The intensity of the X-ray beam is measured through ion chambers, and as can be seen in figure 9, there are three different chambers. I_0 measures the incident intensity, I_t measures the intensity once passed through the sample, and I_{ref} measures the intensity once passed through the sample and a metal foil (same metal that is being measured). The principle of detection in the ion chambers: Each ion chamber is filled with a mixture of inert gas, with the amount set to absorb a specific amount of incident flux. They contain two metal plates, between which a constant potential is applied. The ionised inert gas molecules are attracted to the negative side and the electrons to the positive side, generating a current. The size of the current is therefore directly related to the photons entering the chamber.

The absorption of the X-rays by the sample is given by $\ln(I_0/I_t)$. I_{ref} enables the energy of the X-rays to be calibrated against an internal reference metal foil, as sometimes the

energy readings exhibit a slight shift over time. These shifts are very important when analysing the data, particularly in XANES studies where the edge position contains important information.

$$A = \ln(\frac{I_0}{I_t}) \qquad \textbf{Equation 11}$$

Transmission experiments are usually conducted when there is sufficient concentration of the target element in the material. Too little sample, and the X-ray absorption is low resulting in low signal/noise ratio. Too high, and all the X-rays will be absorbed. As well as the target element, all other sample constituents, their concentrations, and their absorption coefficients must be considered. The absorption edge (μx) of the target element must lie between the values of 0.1 and 1.5, with 1 being the ideal value. The mass of sample required to generate a desired absorption edge can be calculated using the equation below.

$$mass = \frac{(\mu x)(a)}{\left(\frac{\mu}{\rho}\right)} \qquad \textbf{Equation 12}$$

Where a = area and ρ = density

This equation can be subsequently rearranged in order to calculate the total absorption from all the compositional elements, which must be below 2.5. Pelletized samples have been used in this study, with pellet diameters of either 13 mm (1.3 cm^2) or 8 mm (0.5 cm^2).

9.4. Fluorescence Mode

For some low metal loading catalysts, the absorbance of the target element is too low, and the absorbance of the surrounding matrix, often the support material, will dominate. In this scenario, it is not possible to conduct transmission experiments, and instead the data is collected in fluorescence mode. The photoelectric effect process, which occurs upon X-ray irradiation, produces a core hole in the atom of the target element. An outer shell electron drops down to fill the core hole, resulting in the emission of fluorescent radiation equal to the difference in energy between the two atomic shells. The fluorescent radiation produced is characteristic to the target

element, however the signal is only a fraction of the total absorption, resulting in much longer collection times. The signal is proportional to the incident intensity as follows:

$$\mu(E) = \frac{I_{fluorescence}}{I_0} \qquad \textbf{Equation 13}$$

The fluorescence radiation is detected using a solid state detector, which can be windowed to detect specific energy ranges. The detector is positioned so that the angle from the incident beam – sample – detector is 90° (figure 9), and is positioned in a manner to yield maximum fluorescence radiation from the target element without causing total saturation. The signal/noise ratio is much lower compared with transmission experiments, meaning longer acquisitions times are required.

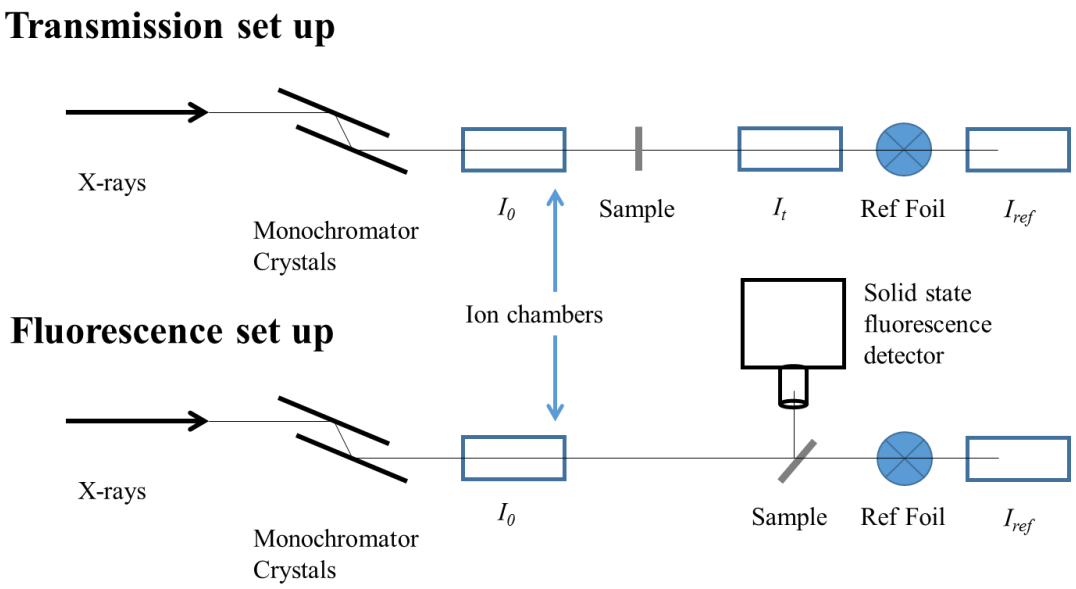

Figure 9. An illustration of the transmission and fluorescence experimental modes that can be used to acquire XAFS.

9.5. X-ray Source – Synchrotrons

X-rays are high energy photons with energy ranging from 500 eV to 500 keV (2.5 nm to 0.0025 nm), and can be produced in synchrotrons throughout the world, offering many advantages to the experimentalist. This includes the production of high intensity X-rays, good tunability over a wide energy range and a high degree of collimation. The synchrotron light in Diamond Light Source is produced and maintained as follows: After heating a high voltage cathode under vacuum, a stream of low energy electrons are produced which are accelerated by earthed anodes. A linear accelerator (LINAC)

is used to accelerate the electrons to a relativistic energy of 100 MeV. Once 100 MeV, the electrons are injected in to the booster ring whereby they undergo further acceleration using a radio frequency voltage source. The electrons reach a final energy of 3 GeV. They enter the storage ring, which consists of 24 straight sections angled to form a closed loop. Bending magnets are used to curve the electron beam between straight sections. The storage ring is maintained under vacuum to minimise the interactions between the electrons and air molecules. Figure 10 illustrates the arrangement of the beamlines at Diamond Light Source.

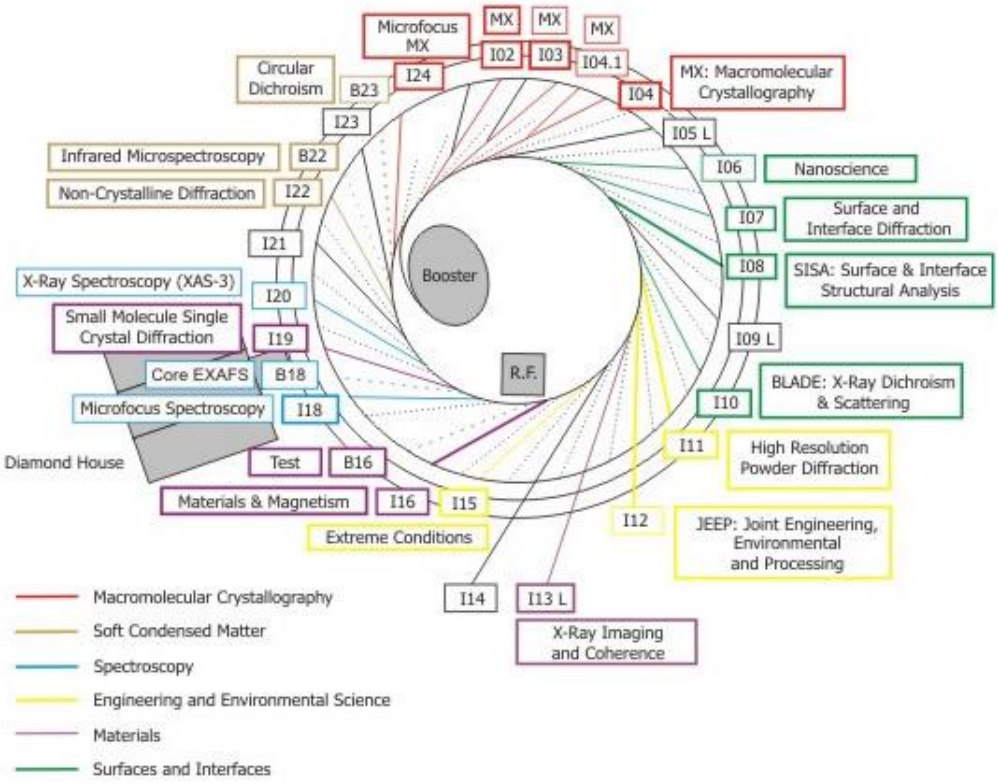

Figure 10. Beamline station arrangement at the Diamond Light Source, Didcot.

10. Chromatography

The goal of all chromatographic methods is to separate the individual components or solutes in a sample. This common technique is used to separate a mixture by taking advantage of the different rates at which the components move through a medium. Typically, there are two phases, the mobile and stationary phase. The components are carried in the mobile phase, and depending on the level of interaction with the stationary phase, due to differences in polarity, are eluted out at different rates

(retention times). Chromatography is either classed as gas or liquid chromatography (GC or LC), depending on the physical state of the mobile phase. The retention time is used for qualitative analysis by comparison with known standards, and the peak area is used for quantitative analysis.

Samples for gas chromatography need to be either a gas or able to be vaporised without decomposition before analysis by GC. Typically a sample is injected into a column with a constant flow of carrier gas where the compounds are separated based on the affinity of the constituents to the stationary phase. The column is placed inside an oven for control of the temperature. After separation and elution from the column the constituents of the sample are passed through a detector, which is usually a flame ionization detector (FID) or thermal conductivity detector (TCD) depending on the analytes. LC is best suited for non-volatile compounds, and although the method of separation is based on the same principles as GC, the mobile phase is liquid and the detection method is different, with UV or refractive index (RI) detectors commonly used.

10.1. FID

A hydrogen flame is used to ionise the sample, with the generation of ions being proportional to the concentration of the species in the gas stream. This detector is particular useful for detecting hydrocarbons as they generally have molar response factors that are equal to the number of carbon atoms, which oxygenates and species containing heteroatoms tend to have a lower response factor.

10.2. TCD

This detector simply responds to changes in the thermal conductivity of the species eluting the column, and compares it to a reference flow of carrier gas. Most compounds have a thermal conductivity much less than that of the common carrier gases of helium or hydrogen, meaning a detectable signal is produced when eluting from the column. The TCD consists of an electrically heated filament in a temperature-controlled cell. A stable heat flow from the filament to the detector body is maintained under normal conditions, but when the thermal conductivity is reduced (upon elution of the analyte), the filament heats up, changing the resistance.

10.3. UV Detector

The principle is the same as that described in section 3 in this chapter, although the wavelength of light used is that in the UV region of the electromagnetic spectrum only (10 – 400 nm). For analysis, it is possible to have single or variable wavelength detectors, measuring absorption of light at these wavelengths to identify the analyte.

10.4. RI Detector

RI detection is used to measure samples that have limited or no UV absorption. The RI detector contains a flow cell split in to two parts: one for the sample and one for the reference solvent. As the chemical compounds elute from the column, a beam of light is passed through the eluted flow. The RI detector measures the difference in refraction between the eluted chemical, and the reference compound (figure 11).

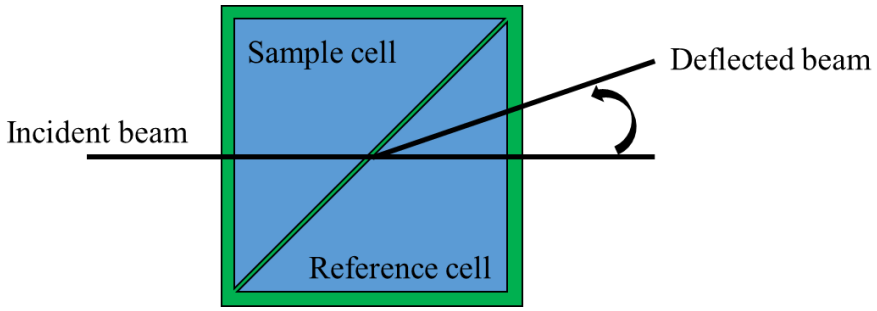

Figure 11. A schematic of the principle mode of detection in an RI detector.

11. Liquid Phase Oxidation of Glycerol

All catalytic testing for the liquid phase oxidation of glycerol was performed by Dr. Alberto Villa and Dr. Carine Chan-Thaw at the University of Milan. Glycerol 0.3 M, and the catalyst (substrate/total Au metal molar ratio = 1000) were mixed in distilled water (total volume 10 mL) and 4 equivalents of NaOH within a Parr 4843 batch reactor with a 30 mL capacity. The reactor was pressurized at 300 kPa with nitrogen and the temperature set to 50°C. Once this temperature was reached, the gas supply was switched to oxygen and the monitoring of the reaction started. Samples were removed periodically and analyzed by HPLC using an Alltech OA- 10308, 300 mm_7.8 mm column and with UV and RI detectors. Aqueous H_3PO_4 solution (0.1 wt. %) was used as the eluent. Concentrations of reactants/products were determined using calibration curves obtained by injecting standard solutions of known concentrations.

Reaction conversion, turnover frequency (TOF) and product selectivity for each of the catalysts was calculated based equations 14, 15 and 16, respectively. The turnover frequency was calculated based on the total moles of metal (as calculated by MP-AES), so as to obtain normalised performance values which can be compared directly with other previously reported studies.[1]

$$Conversion\ (\%) = \frac{moles\ of\ substrate\ at\ T_0 - moles\ of substrate\ at\ T_x}{moles\ of\ substrate\ at\ T_0}\ x\ 100 \qquad \textbf{Equation 14}$$

Where T_0 is the time before the start of reaction and T_x is denoted as the time after starting the reaction.

$$TOF = \frac{moles\ of\ substrate\ converted}{moles\ of\ total\ metal}\ x\ hr^{-1} \qquad \textbf{Equation 15}$$

$$Selectivity\ (\%) = \frac{moles\ of\ product\ formed}{moles\ of\ starting\ substrate}\ x\ 100 \qquad \textbf{Equation 16}$$

12. Hydrogenation of Furfural

All catalytic testing for the hydrogenation of furfural was performed by Dr. Alberto Villa and Dr. Carine Chan-Thaw at the University of Milan. The reaction was performed at two different reaction temperatures, 25 or 50°C. A Parr 4843 stainless steel batch reactor with a 30 mL capacity was used, equipped with a heater, mechanical stirrer, gas supply system and thermocouple. The reaction was performed as follows: Furfural solution (15 mL; 0.3 M in 2-propanol) was added into the reactor and the desired amount of catalyst (Furfural/metal molar ratio = 500) was suspended in the solution. The pressure of the hydrogen was set to 5 bar. The mixture was left at room temperature (25°C) or was alternately heated to 50°C and mechanically stirred at 1250 rpm. At the end of the reaction, the autoclave was cooled down to room temperature (when performed at 50°C), the hydrogen flow was stopped and the autoclave purged with flowing nitrogen for 10 minutes. Samples were removed periodically (0.2 mL) and were analysed using a HP 7820A gas chromatograph equipped with a capillary column HP-5 30m x 0.32mm, 0.25 µm film, provided by Agilent Technologies and TCD and FID detectors. Authentic samples were analyzed to determine separation times. Quantitative analysis with external standard method (n-octanol) was used. Reaction conversion, turnover frequency (TOF) and product selectivity for each of the catalysts was calculated based equations 14, 15 and 16, respectively.

13. Hydrogenation of *p*-Nitrophenol

UV-Vis spectroscopy was used to monitor the reaction. *p*-nitrophenol has an absorbance band at 300 nm, but in the presence of base there is a red shift to 400 nm, as a result of the transformation in to *p*-nitrophenolate ions.[25] At this wavelength, it is possible to observe the absorbance of *p*-nitrophenolate using plastic cuvettes. A calibration was performed in order to calculate a molar extinction coefficient of the *p*-nitrophenolate ions, according to the Beer-Lambert law (figure 12). An absorbance *vs.* concentration plot yields a straight line, in which the molar extinction coefficient can be directly obtained from the gradient (figure 13). The hydrogenation of *p*-nitrophenol was performed at the Research Complex at Harwell, and the molar extinction coefficient was calculated to be 18873 M^{-1} cm^{-1}.

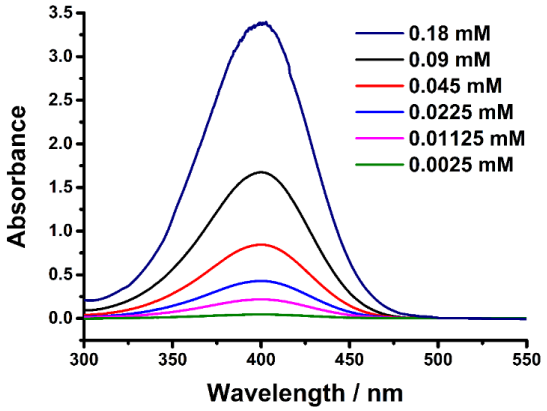

Figure 12. The absorbance of *p*-nitrophenolate at different concentrations.

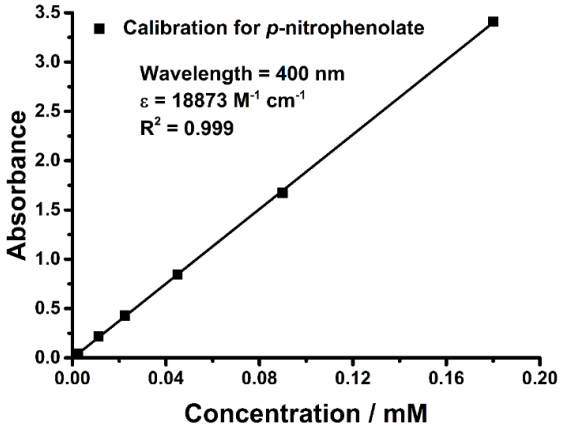

Figure 13. Calibration curve of absorbance versus concentration for *p*-nitrophenolate (absorbance obtained at 400 nm).

In a typical catalytic experiment, 2 mg of catalyst was weighed in to a polystyrene cuvette. $NaBH_4$ (0.3 mL, 0.039 M, $NaBH_4$/*p*-nitrophenol molar ratio = 25) was added to the catalyst, left for 15 seconds, before *p*-nitrophenol solution (2.7 mL, 1.80 x 10^{-4} M, *p*-nitrophenol/metal molar ratio = 13) was subsequently added, initiating the start of the reaction. UV-Vis spectra (600-300 nm) were then collected at room temperature with 12 second time intervals for 15 minutes. For recycling experiments, the reaction procedure was scaled-up and performed in a round bottom flask using the same conditions. The catalysts were collected after reaction, washed with deionised water (100 mL) and dried at room temperature.

14. References

1. Dimitratos, N.; Messi, C.; Porta, F.; Prati, L.; Villa, A. *Journal of Molecular Catalysis A: Chemical,* 2006**, *256*** (1–2), 21-28.
2. Lopez-Sanchez, J. A.; Dimitratos, N.; Miedziak, P.; Ntainjua, E.; Edwards, J. K.; Morgan, D.; Carley, A. F.; Tiruvalam, R.; Kiely, C. J.; Hutchings, G. J. *Physical Chemistry Chemical Physics,* 2008**, *10*** (14), 1921-1930.
3. DiScipio, R. G. *Analytical Biochemistry,* 1996**, *236*** (1), 168-170.
4. Teranishi, T.; Miyake, M. *Chemistry of Materials,* 1998**, *10*** (2), 594-600.
5. Salvati, R.; Longo, A.; Carotenuto, G.; De Nicola, S.; Pepe, G. P.; Nicolais, L.; Barone, A. *Applied Surface Science,* 2005**, *248*** (1–4), 28-31.
6. Seoudi, R.; Fouda, A. A.; Elmenshawy, D. A. *Physica B: Condensed Matter,* 2010**, *405*** (3), 906-911.
7. Benkovicova, M.; Vegso, K.; Siffalovic, P.; Jergel, M.; Luby, S.; Majkova, E. *Thin Solid Films,* 2013**, *543*** (0), 138-141.
8. Khanna, P. K.; More, P.; Jawalkar, J.; Patil, Y.; Rao, N. K. *Journal of Nanoparticle Research,* 2009**, *11*** (4), 793-799.
9. Link, S.; El-Sayed, M. A. *The Journal of Physical Chemistry B,* 1999**, *103*** (21), 4212-4217.
10. Philip, D. *Spectrochimica Acta Part A: Molecular and Biomolecular Spectroscopy,* 2008**, *71*** (1), 80-85.
11. Qiu, P.; Wang, L.; Mao, C. B. *Transmission Electron Microscopy Characterization of Nanomaterials*, Kumar, C. S. S. R., Ed. Springer Berlin Heidelberg, 2014; pp 1-41.

12. Niemantsverdriet, J. W. *Spectroscopy in Catalysis*, Wiley-VCH Verlag GmbH & Co. KGaA, 2007; pp 179-216.
13. Schneider, C. A.; Rasband, W. S.; Eliceiri, K. W. *Nat Meth,* 2012***, 9*** (7), 671-675.
14. Jian, N.; Palmer, R. E. *Journal of Physical Chemistry C,* 2015***, 119*** (20), 11114-11119.
15. Lear, T.; Marshall, R.; Lopez-Sanchez, J. A.; Jackson, S. D.; Klapotke, T. M.; Baumer, M.; Rupprechter, G.; Freund, H. J.; Lennon, D. *Journal of Chemical Physics,* 2005**,** ***123*** (17), 13.
16. Thibault-Starzyk, F.; Maugé, F. *Characterization of Solid Materials and Heterogeneous Catalysts*, Wiley-VCH Verlag GmbH & Co. KGaA, 2012; pp 1-48.
17. Smith, B. C., *Fundamentals of Fourier Transform Infrared Spectroscopy*. 2 ed.; Taylor & Francis: 2011.
18. Armaroli, T.; Bécue, T.; Gautier, S. *Oil & Gas Science and Technology - Rev. IFP,* 2004***, 59*** (2), 215-237.
19. Niemantsverdriet, J. W. *Spectroscopy in Catalysis*, Wiley-VCH Verlag GmbH & Co. KGaA, 2007; pp 217-249.
20. Niemantsverdriet, J. W. *Spectroscopy in Catalysis*, Wiley-VCH Verlag GmbH & Co. KGaA, 2007; pp 147-177.
21. Geantet, C.; Pichon, C. *Characterization of Solid Materials and Heterogeneous Catalysts*, Wiley-VCH Verlag GmbH & Co. KGaA, 2012; pp 511-536.
22. Koningsberger, D. C.; Mojet, B. L.; van Dorssen, G. E.; Ramaker, D. E. *Topics in Catalysis,* 2000***, 10*** (3-4), 143-155.
23. Ravel, B.; Newville, M. *Journal of Synchrotron Radiation,* 2005***, 12*** (4), 537-541.
24. Newville, M. *Journal of Synchrotron Radiation,* 2001***, 8*** (2), 322-324.
25. Liu, J. C.; Qin, G. W.; Raveendran, P.; Kushima, Y. *Chemistry-a European Journal,* 2006***, 12*** (8), 2132-2138.

Chapter Three. Au/TiO_2 for the Oxidation of Glycerol

An area of research that has progressed in the last 20 years is the valorization of renewable raw materials, due to the progressive depletion of fossil resources. The following chapter explores the catalytic transformation of an important bio-derived compound, glycerol (1,2,3-propanetriol), using Au based catalysts prepared by sol-immobilisation method.

1. Introduction

Since its discovery in 1779, the production of glycerol has increased significantly.[1] Glycerol is sourced from triglycerides, the main constituents of fats and oils (animal and vegetable). There are three production methods used to produce glycerol, depending on the type of reaction triglycerides undergo: i) Saponification, the chemical transformation illustrated in scheme 1 where Y = ONa, yielding glycerol and soaps, ii) Hydrolysis, scheme 1 where Y = OH, yielding glycerol and fatty acids or, iii) Transesterification, scheme 1 where Y = OCH_3, yielding glycerol and fatty acid methyl esters. The latter process is the well accustomed chemical process to produce bio-diesel, in which 10% of the weight of biodiesel is generated in glycerol.[1] It is estimated that the world production of glycerol has reached 4 billion gallons of glycerol in 2016.[2]

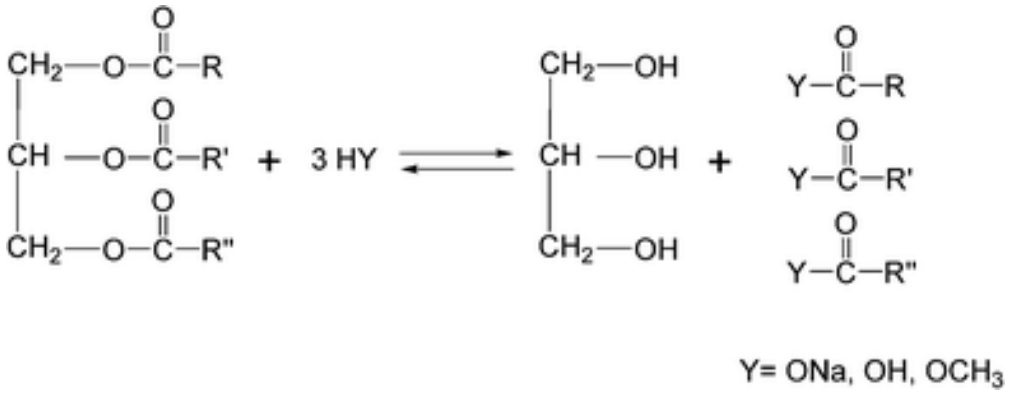

Scheme 1. The synthesis of glycerol from fats and oils.[3]

Glycerol is considered a precious commodity due to the transformations it can undergo to produce a range of useful chemicals and energy fuels. As discussed in chapter 1,

section 4.1.4, the selective oxidation of alcohols to yield a specific product is an important reaction in the synthesis of many useful intermediates or valuable fine chemicals.[4] As a highly functionalised molecule, possessing three hydroxyl groups rendering similar chemical reactivity, there are many possible oxidation products as demonstrated in scheme 2, hence yielding a selective product is difficult.[5] However, it has been established that the initial oxidation pathway (oxidation at the primary or secondary alcohol) is dependent on the reaction conditions (pH, temperature, substrate/metal ratio), as well as the choice of the metal catalyst employed to perform the catalysis. Useful selective products are dihydroxyacetone, which has been used as an active substance in sunless tanning lotions as well as a monomer in polymeric biomaterials,[3] and glyceric acid, which can be used for the treatment of skin disorders.[3]

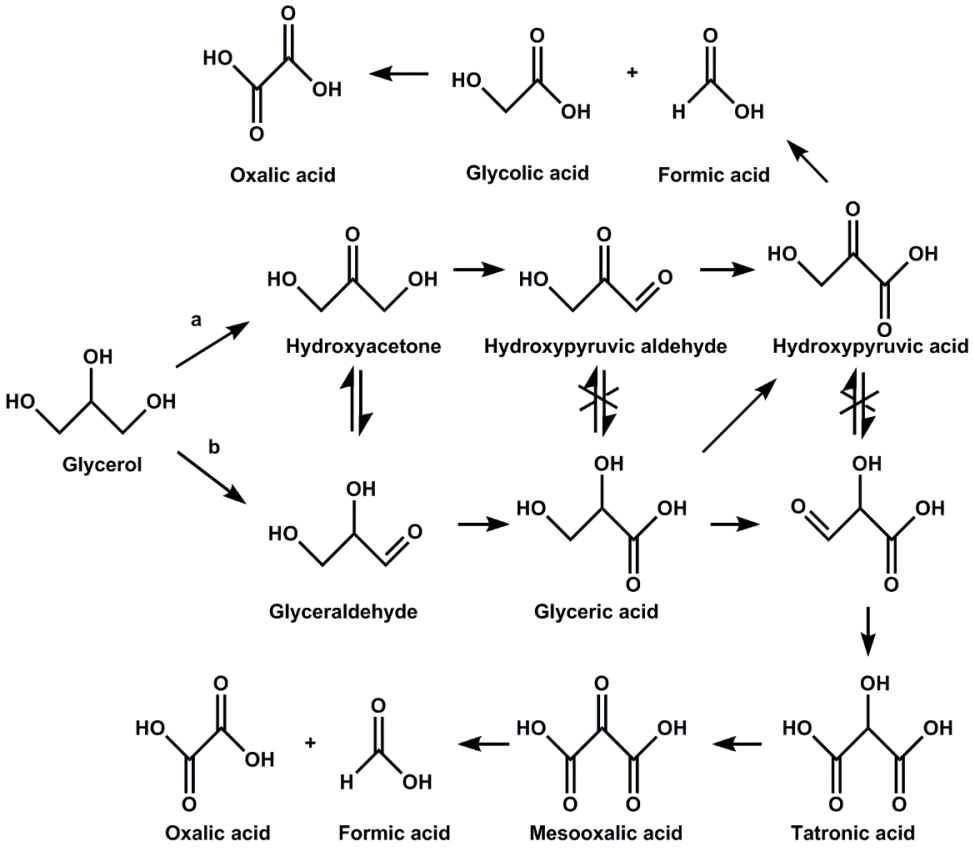

Scheme 2. Product distribution from the oxidation of glycerol.[6]

The high boiling point of glycerol, 290°C, means the reaction is carried out in the liquid phase, using dioxygen as the more environmentally friendly oxidant compared with traditional oxidising agents (permanganate and chromic acid).[7] The liquid phase oxidation of glycerol is typically performed under mild basic conditions, within a temperature range of 30-60°C and oxygen pressure from atmospheric to a few

atmospheres. Although studies are performed under basic conditions, the role of the base is still not fully understood but in many studies it is thought to be involved in the first step of the oxidative process, in which the glycerol molecule is deprotonated to form the alkoxide anion.[8] It has also been proposed that the presence of the base may also be important for prolonging the catalyst life by removing hydroxyacid products that are irreversibly adsorbed on the metal active sites.[9-12] Most literature studies have focused on noble metal based catalysts (Pd, Pt and Au), with the oxidation proceeding more selectively on Au compared with other metals.[13-14] Pt has been shown to suffer from oxygen poisoning,[15] whereas Au is much more resistant allowing higher oxygen partial pressures to be employed.

Rossi, Prati and co-workers were the first to show that supported gold nanoparticles were effective for liquid phase alcohol oxidations in the presence of a base.[13, 16-17] Subsequent research by Carretin *et al*. in 2002 showed that carbon supported Au catalysts were active for glycerol oxidation, but only under pressurised and basic conditions.[18] The Au/C catalyst exhibited 100 % selectivity to glycerate but only 56 % glycerol conversion. In the past 14 years, extensive research has focused on understanding and determining the catalyst properties governing performance (activity and selectivity). One of the most studied parameters is the influence of the Au particle size, to which it was concluded that larger particles are more selective to glycerate but exhibit lower mass activity (turnover frequencies) than smaller particles, [17, 19-20] and thus a compromised gold particle size is desirable to achieve the optimum catalytic activity and selectivity, ~ 20 nm.[21]

The choice of the support material has also been studied, and it has been shown that carbon is not the only effective support, but metal oxides such as titania can also be utilised for this reaction.[22] Enache *et al*. previously demonstrated that titania, supporting Au and Pd nanoparticles, was a useful material in the liquid phase of other alcohols.[23]

The sol-immobilisation method is a preparation technique with great ability to prepare metal nanoparticles with tailored properties. In general, this reproducible preparation method affords small Au particles < 10 nm with a narrow particle size distribution.[24] The effect of Au particle size on both selectivity and activity in glycerol oxidation has previously been investigated in two separate studies by Dimitratos *et al*., in which a

systematic variations in Au particle size was achieved by varying the concentration of metal precursor, polymer/metal ratio and reducing agent during the sol-immobilisation synthesis procedure.[24-25] As mentioned earlier, the activity of the catalyst in glycerol oxidation decreased as the Au particle size increased, with a reverse trend observed for the selectivity towards glyceric acid, but it was also demonstrated that the amount of stabilising agent, PVA, influences the catalyst performance. The role of the PVA in the oxidation of glycerol reaction is still not fully understood, but it is thought to influence the binding of glycerol by interaction through the hydroxyl groups.[26-27]

In the present chapter, a modified sol-immobilisation method, as detailed in chapter 2, section 2 is used to prepare Au/TiO_2 catalysts. Preforming metal nanoparticles, as is the case during the sol-immobilisation technique, has advantages as it allows for greater control over the metal particle properties. The effect of temperature and solvent environment during colloidal Au formation, on the resulting Au morphology (Au diameter and surface sites), has not previously been explored to our knowledge. In the present study the catalyst structure is investigated using TEM, STEM HAADF, XAFS and CO-chemisorption with IR, corroborated by DFT calculations. All catalysts are tested for their performance in the liquid phase oxidation of glycerol to investigate the influence of preparation conditions on the catalyst activity, selectivity and stability.

2. Experimental Details

2.1. Catalyst Synthesis

A modified sol-immobilisation method, as detailed in chapter 2, section 2, was used to prepare Au/TiO_2 catalysts. All theoretical Au loadings were 1 wt. % on to TiO_2. As mentioned, different temperatures and H_2O/EtOH solvent ratio were used during the catalyst preparation, with the conditions presented in table 1, as well as an abbreviated notation to be used throughout the chapter. Different solvents were employed in order to vary the temperature; PVA is insoluble in $H_2O \leq 0$°C.

Table 1. Details of the Au/TiO_2 catalysts prepared using the sol-immobilisation method

Temperature / °C	H_2O/EtOH solvent ratio (vol:vol)	Sample notation
1	100	Au A1
25	100	Au A2
50	100	Au A3
75	100	Au A4
−30	50	Au B1
0	50	Au B2
30	50	Au B3
−75	0	Au C1
−30	0	Au C2

2.2. UV-Vis, MP-AES, TEM, STEM HAADF, XRD and DRIFTS Analysis

The details of all the techniques used to characterise the catalyst can be found in chapter 2.

2.3. Au L_3 XAFS Investigations

Au L_3 edge XAFS spectra were acquired on the B18 beamline at the Diamond Light Source, Didcot, U.K. Measurements were performed in fluorescence mode using a QEXAFS set-up with a fast-scanning Si(111) double crystal monochromator and a 9 element Ge detector. The time resolution of the spectra was 2 min/spectrum (k_{max}=14). On average, 25 scans were acquired to improve the signal-to-noise level of the data. An EXAFS spectrum of the Au metal foil was acquired in transmission mode and used as a reference material. All catalysts were prepared as pure pellets, with no dilution.

3. Results and Discussion

3.3. MP-AES Analysis

Elemental analysis was performed to assess the real Au metal loading immobilised on to TiO_2, after a theoretical Au metal loading of 1 wt. % was deposited in all cases. The filtrate collected after the immobilisation process was analysed in MP-AES, and the Au concentrations calculated (table 2) at two particular emission wavelengths characteristic of Au (242.8 and 267.6 nm).

Table 2. MP-AES results of the filtrate obtained in the deposition of 1 wt. % Au/TiO_2.

	Concentrations (ppm) at different Au wavelengths (nm)	
	Au 242.8	**Au 267.6**
Au filtrate A1	0.01	0.01
Au filtrate A2	0.00	0.01
Au filtrate A3	0.00	0.01
Au filtrate A4	0.00	0.01
Au filtrate B1	0.01	0.01
Au filtrate B2	0.00	0.01
Au filtrate B3	0.00	0.01
Au filtrate C1	0.01	0.01
Au filtrate C2	0.00	0.01

Hypothetically, if there was 0 % immobilisation of Au on to TiO_2, the resulting filtrate would record a concentration of 15.4 ppm in the MP-AES analysis, based on the concentrations used in the digestion procedure. As the maximum concentration obtained from any one filtrate is 0.01 ppm, it concludes that the proportion of Au that failed to immobilise is negligible, and the Au metal loading on to TiO_2 is 1 wt. % in all catalysts.

3.6. XRD

XRD was used to assess the long range order in the Au/TiO_2 catalysts and, where possible, obtain an average Au crystallite size using the Scherrer equation. The diffraction pattern of the catalyst prepared at 1°C in H_2O (A1) is illustrated in figure

1. It is evident that the major diffraction contribution is from the TiO_2 support material, which consists of anatase and rutile phases, and not from the Au metal.[28] The small Au particle size coupled with the low metal loading, is the likely cause as to why the Au is not observed in the diffraction pattern, deeming it impossible to apply the Scherrer equation for an average Au crystallite size estimation. Instead, TEM and XAFS are used to calculate the average Au particle diameter.

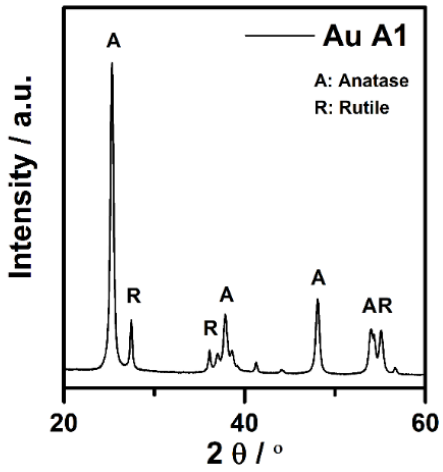

Figure 1. The diffraction pattern of the Au/TiO_2 catalyst, in which colloidal Au was prepared at 1°C in a H_2O solvent (A1).

3.2. UV-Vis Spectroscopy

UV-Vis spectroscopy was used during colloidal Au formation, to assess both the state of reduction of the metal salt precursor, and the Au surface plasmon resonance (SPR) band, which can be used as an indicative tool to assess metal nanoparticle size. Figure 2 shows the UV-Vis spectrum of the $HAuCl_4$ precursor, with a peak at 222 nm, indicative of ligand to metal charge transfer in $[AuCl_4]^-$.[29] Upon reduction with $NaBH_4$, and stirring for 30 minutes, this bands disappear for preparation temperatures > 0°C, and a subsequent band appears at ~ 500 nm. The presence of this band, the SPR band, indicates nano-particulate Au has been formed.[29] In all cases, the SPR band is broad, and so the wavelength position of the SPR band is taken as the wavelength at maximum absorbance in this region, and is reported in table 3. It appears that for low temperature preparation below 0°C (Au B1, C1 and C2), there is still a small amount of metal precursor species remaining, as there is a small band at 290 nm in each spectrum taken after 30 minutes. Lowering the temperature within the same solvent

environment increases the viscosity of the colloidal mixture. The increased viscosity negatively affects the stirring rate in the mixture, and hence in this instance, slows the ability of $NaBH_4$ to reduce the metal precursor.

The Au SPR band position can be shifted depending on the surrounding solvent environment, as a result of differing dielectric properties of the solvent media.[30] Therefore, it is only possible to comment on shifts within the same solvent systems. It can be observed that there is a general shift to a higher wavelength of the peak position of the SPR band as the temperature to which the Au sols are synthesised, increases. The shift indicates the formation of larger Au particles as the temperature of colloidal reduction increases.[31] This trend is observed for both the pure H_2O and mixed H_2O:EtOH solvent systems. For Au C1 (−75°C, EtOH), there is no obvious SPR band, or it is too broad to observe. There are three possibilities for this: the size of the Au nanoparticles in the colloid is very small, nano-particulate Au has not been formed (larger particles instead), or there has not been sufficient reduction to enable the preparation of colloidal Au. The latter is most likely due to the high viscosity of the mixture inhibiting the stirring speed at low temperatures, and hence the reduction rate.

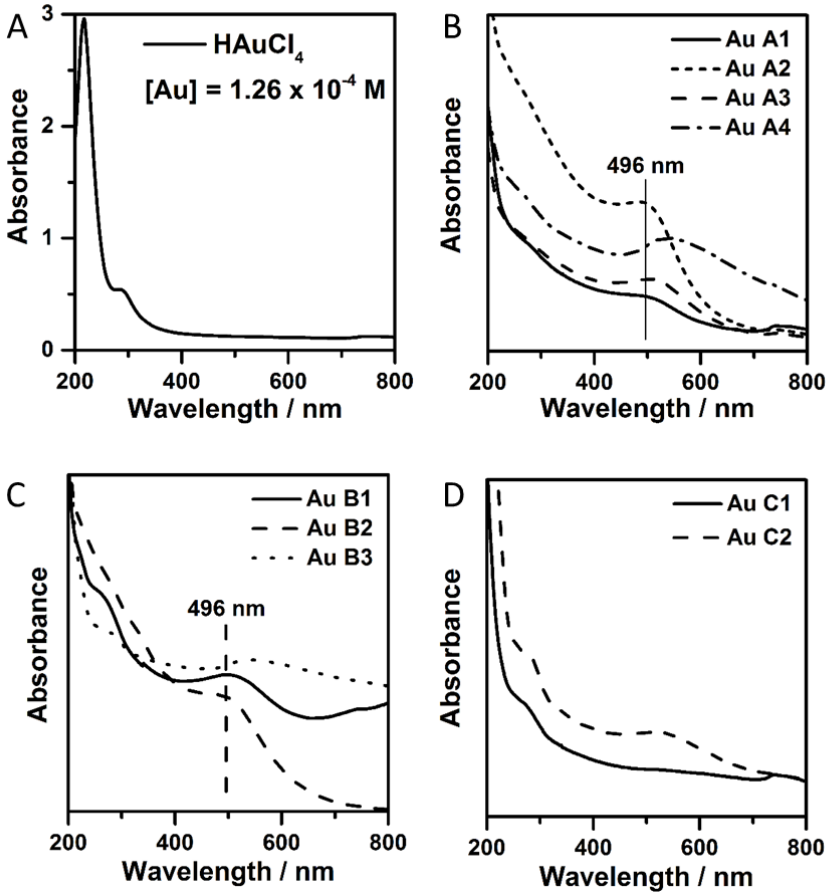

Figure 2. UV-Vis spectra of the $HAuCl_4$ precursor (A) and the subsequent Au sols generated after reduction of the salt in the presence of PVA within different solvent environments H_2O (B), H_2O:EtOH (C) and EtOH (D), at different temperatures.

3.4. TEM

TEM was performed on all Au/TiO_2 catalysts to determine the average Au particle diameter, and observe the particle diameter distribution, with the effect of temperature and solvent on the average Au particle size illustrated in figure 3. Representative TEM images and the derived histograms of the Au catalysts are presented in figures 4 and 5, respectively, with the average Au particle diameter and deviation presented in table 3. The standard sol-immobilisation method widely used for the preparation of supported metal nanoparticles (PVA/metal wt. ratio = 0.65, $NaBH_4$/metal molar ratio = 5, 25°C) is equivalent to Au A2 in this study, yielding an average Au particle diameter of 2.3 nm.

It is apparent that increasing the temperature at which the colloidal Au is prepared, results in an increased average Au particle diameter. The smallest average Au particle

diameter afforded in a H_2O solvent was 2.0 nm, achieved when the catalyst was prepared at 1°C (Au A1).

Preparing colloidal Au in the mixed H_2O:EtOH and pure EtOH solvents results in the same temperature dependant average Au particle diameter effects. The smallest Au particles of any solvent system were prepared at −30°C in a mixed H_2O:EtOH, yielding an average Au diameter of 1.8 nm. This appears to be the smallest average Au particle diameter obtained using the sol-immobilisation method with PVA and $NaBH_4$. The decrease in particle diameter achieved from that of the standard preparation may appear small, but it provides evidence that this sol-immobilisation method (using PVA and $NaBH_4$) can be modified to stabilise very small metal particles under the right conditions. To observe how the solvent environment during preparation affects the average Au particle size, it is possible to compare catalysts A1 against B2 (1°C), as well as A2 against B3 (25°C), as these samples have comparable temperatures of colloidal reduction. There is little difference in average Au particle size when comparing A1 and B2, but there is an increase of 1.8 nm between the catalysts A2 and B3, which gives an indication that switching to a lower H_2O:EtOH solvent ratio increases the Au particle size during colloidal preparation. Switching to a pure EtOH solvent, and generating colloidal Au at −75°C did not have the desired effect of reducing the average Au particle diameter further. Instead, preparation in an EtOH solvent yields larger Au particles, regardless of the temperature. This effect can probably be attributed to the insoluble nature of PVA in EtOH, with full solubility only achieved if a few drops of H_2O are added during its preparation.

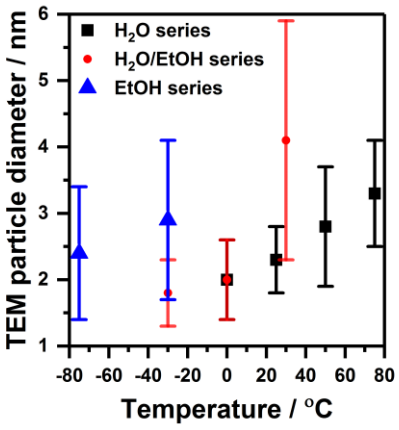

Figure 3. The effect of temperature on the average Au particle diameter from TEM, in different solvent systems, across 300 particles.

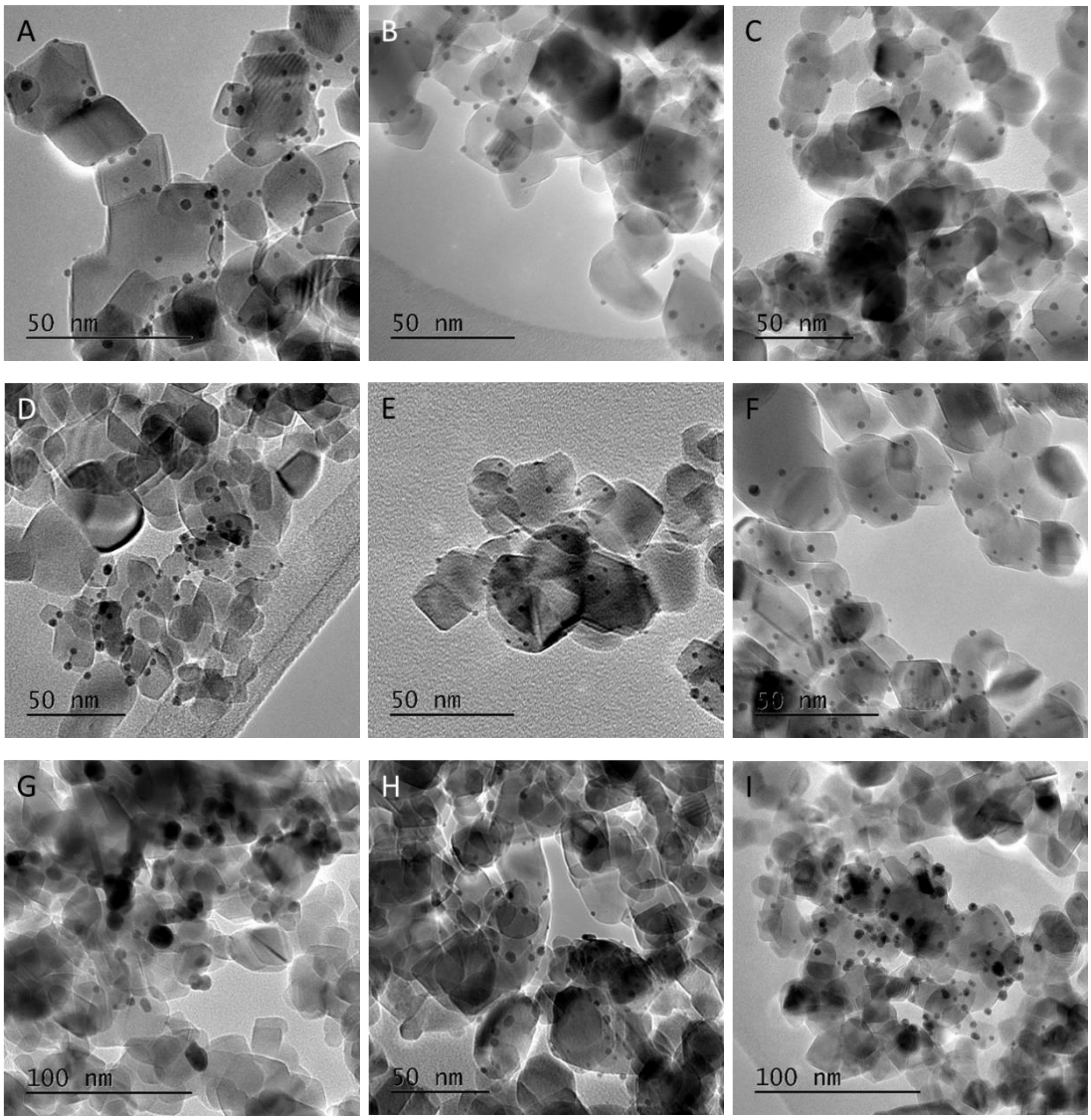

Figure 4. Au particle diameter histograms for the Au/TiO_2 catalysts prepared at different temperatures and in different solvent environments; A) 1°C H_2O A1, B) 25°C H_2O A2, C) 50°C H_2O A3, D) 75°C H_2O A4, E) −30°C H_2O:EtOH B1, F) 1°C H_2O:EtOH B2, G) 30°C H_2O:EtOH B3, H) −75°C EtOH C1 and I) −30°C EtOH C2.

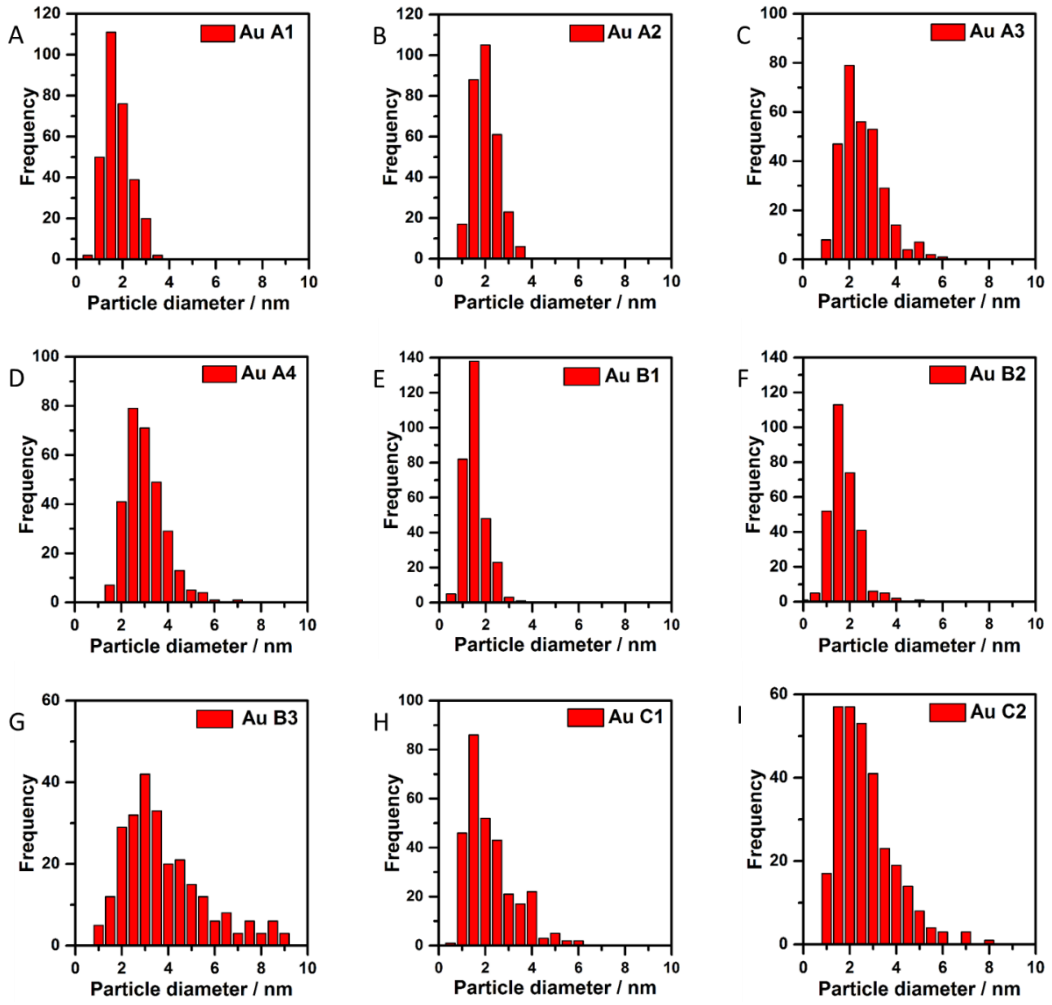

Figure 5. Au particle diameter histograms for the Au/TiO_2 catalysts prepared; A) 1°C H_2O A1, B) 25°C H_2O A2, C) 50°C H_2O A3, D) 75°C H_2O A4, E) −30°C H_2O:EtOH B1, F) 1°C H_2O:EtOH B2, G) 30°C H_2O:EtOH B3, H) −75°C EtOH C1 and I) −30°C EtOH C2.

Table 3. SPR band maximums for colloidal Au prepared under various conditions, and TEM Au particle diameters and corresponding standard deviation (over 300 particles) for the resulting Au/TiO_2 catalyst.

Au/TiO_2 catalyst	**UV-Vis maximum / nm**	**Average TEM particle size/ nm**
A1	500	2.0 ± 0.6
A2	490-500	2.3 ± 0.5
A3	500-510	2.8 ± 0.9
A4	538	3.3 ± 0.8
B1	490-500	1.8 ± 0.5
B2	496	2.0 ± 0.6
B3	535-546	4.1 ± 1.8
C1	-	2.4 ± 1.0
C2	516-520	2.9 ± 1.2

3.5. HAADF STEM

A1 and B1 catalysts were examined through HAADF STEM microscopy, which is capable of angstrom resolution, to investigate the presence of Au clusters that are too small to image with standard TEM. For both Au catalysts, Au clusters below 1 nm were recorded, with a select few illustrated in figure 6. It was observed that ultra-small Au clusters comprising of only a few atoms are present for the Au A1 catalyst (figure 7), but were not, however, identified for B1. The quantitative analysis of the clusters' integrated HAADF STEM intensity calculates the ultra-small clusters to consist of 1 to 5 Au atoms. Clusters of this size regime have not before been observed for the sol-immobilisation method in which PVA and $NaBH_4$ are used as the protecting and reducing agent, respectively. However, a limitation of this technique is the required effort and time in order first to find, and then to image the small metal clusters in high resolution. Therefore, it is quite possible that low temperature preparation in the mixed solvent does yield ultra-small clusters similar, but their abundance is lower, compared with the Au A1 catalyst.

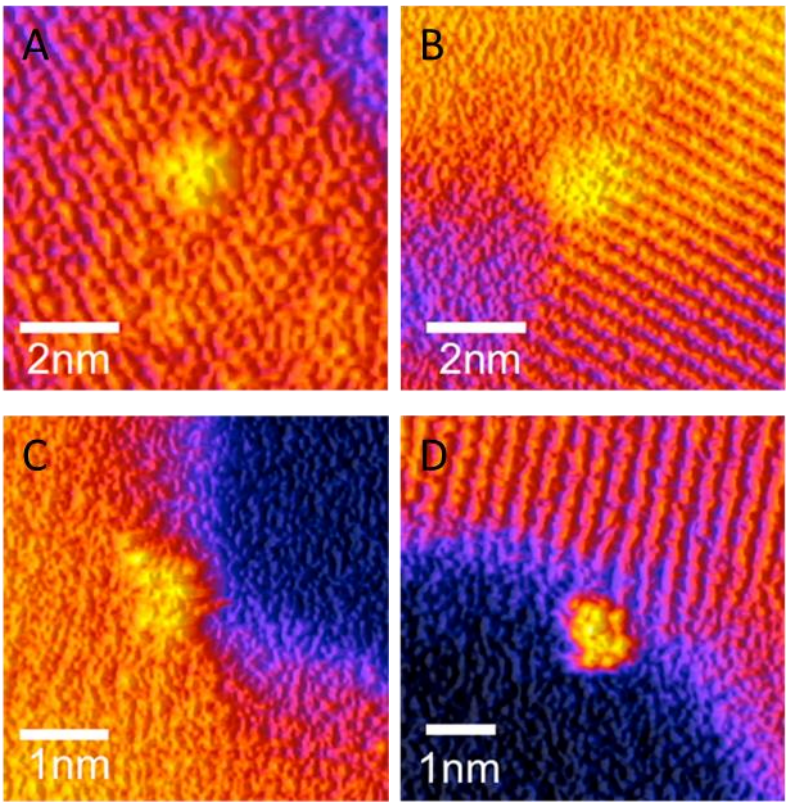

Figure 6. HAADF STEM images of; A and B) A1 Au/TiO_2 catalyst (prepared in H_2O at 1°C) and C and D) B1 Au/TiO_2 catalyst (prepared in H_2O:EtOH at −30°C).

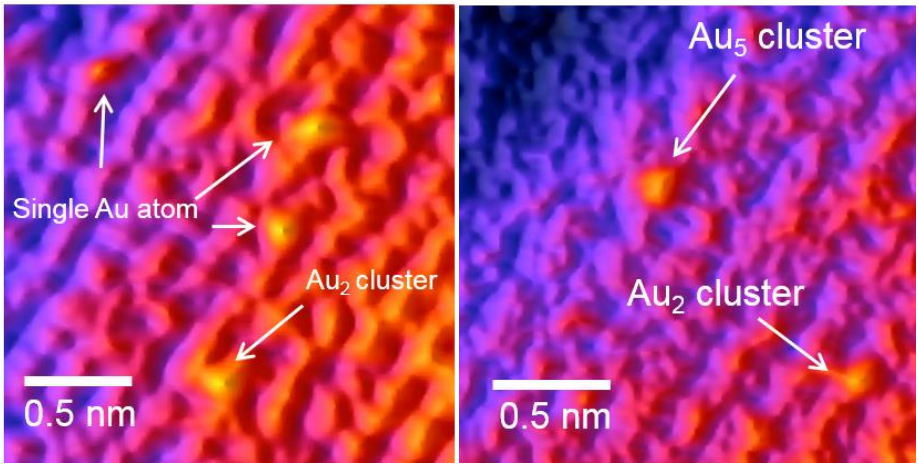

Figure 7. HAADF STEM images of Au/TiO_2 catalyst, in which colloidal Au was prepared at 1°C in a H_2O solvent (A1), indicating the presence of ultra-small Au clusters.

3.7. EXAFS

As discussed in chapter 2, section 9, XAS is a powerful technique which is not limited to study materials with long range order, but instead can be used to study the structure of all materials (ordered and amorphous). In this study, EXAFS is used to calculate the average Au particle size, as a representation of the whole sample. The first shell EXAFS fitting parameters are shown in table 4, as well as the k^2-weighted magnitude Fourier transform data and corresponding fit presented in figure 8. The magnitude in the y-axis is related to the average scattering contribution from neighbouring atoms. Considering two different sized Au nanoparticles, the average coordination to a neighbouring Au atom would be lower in the smaller particle compared with the larger counterpart. Therefore, the amount of signal scattering, and hence the magnitude of the y-axis, would be lower. EXAFS data shows that for all catalysts prepared, the Au environment is dominated by a primary Au coordination shell. After data fitting in the Artemis software, the Au-Au first shell coordination numbers range between 7.7-11.2, all of which are lower than that found for bulk Au (12), indicating nano-particulate Au has been formed. Transforming the first shell coordination number in to Au particle size is performed using the approach of Beale *et al*,[32] in which the EXAFS spectrum of Au clusters with different packing arrangements and number of Au atoms (and subsequent Au particle diameters) was simulated. The formula used in this study is based on the assumptions that the nanoparticles are spherical, face centred cubic and a coordination number < 10, with the calculated Au particle sizes presented in table 4. The average Au particle diameters obtained from EXAFS strongly supports the

conclusion from the TEM analysis: B1 is the catalyst with the smallest average Au particle diameter (1.18 nm), and there is a systematic increase in average Au particle size with increased temperature of colloidal Au preparation. As well as using the coordination number to assess the particle size, an extension of the primary Au-Au radial distance (R) from 2.81 to 2.84 Å represents increased Au particle size.[33] The particle diameter obtained from EXAFS is smaller than that obtained with TEM, which is typical, due to EXAFS accounting for all the atoms that cannot be observed with standard TEM.

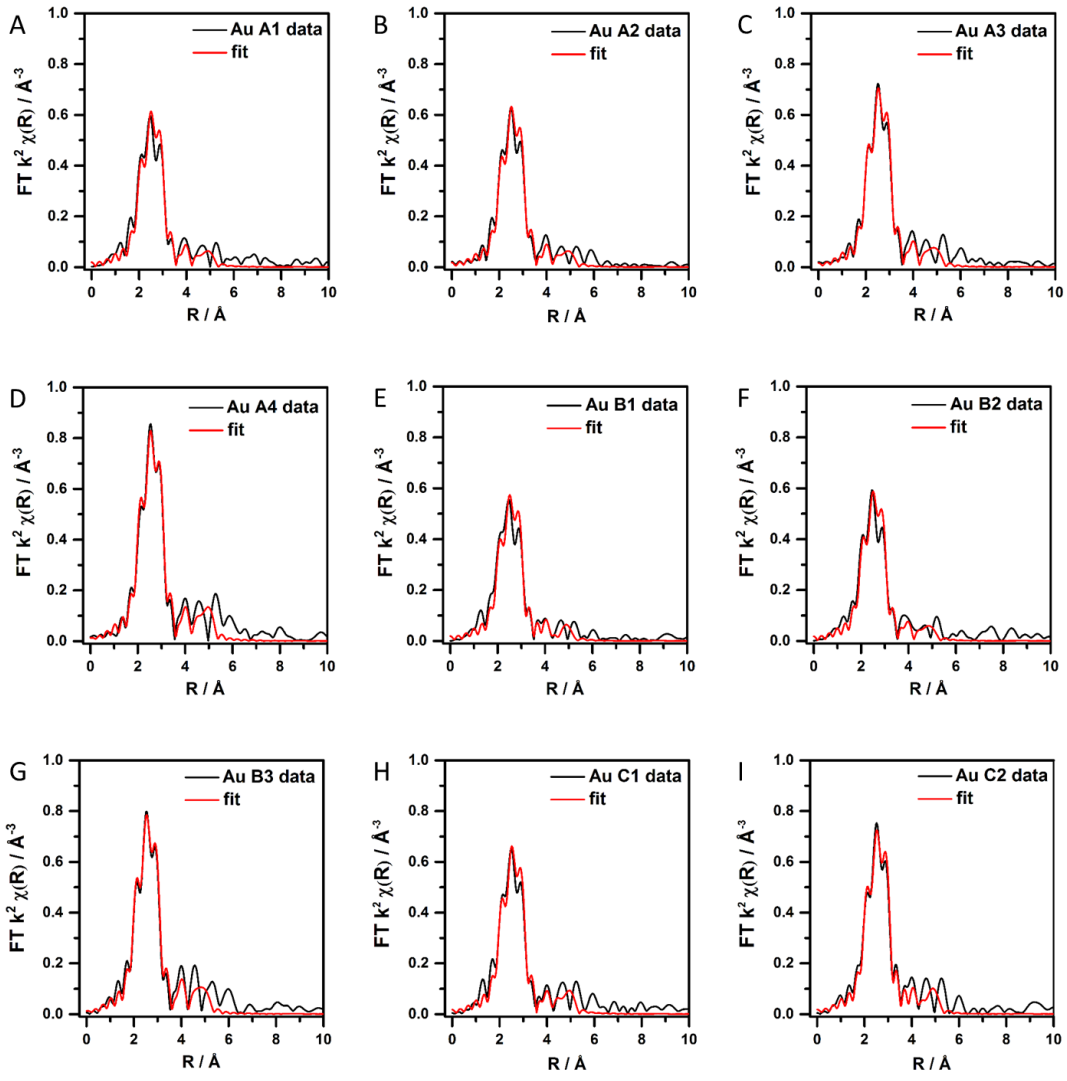

Figure 8. Magnitude component of the k^2 weighted Fourier transform data and corresponding fit for all the Au/TiO_2 catalysts prepared in different solvent systems at controlled temperatures; A) 1°C H_2O A1, B) 25°C H_2O A2, C) 50°C H_2O A3, D) 75°C H_2O A4, E) −30°C H_2O:EtOH B1, F) 1°C H_2O:EtOH B2, G) 30°C H_2O:EtOH B3, H) −75°C EtOH C1 and I) −30°C EtOH C2.

Table 4. Au L_3 edge EXAFS fitting parameters for the Au/TiO_2 catalysts prepared in different solvent systems at controlled temperatures.

Sample [a]	Absorber-Scatter	N	*R* / Å	$2\sigma^2$ / Å^2 [b]	E_f / eV	R_{factor}	Average Au diameter / nm
	Au-Au	8.2 (4)	2.81 (7)	0.008	2 (1)	0.03	1.35
Au A1	Au-Au	2 (1)	4.01 (7)	0.008			
	Au-Au	5 (3)	4.94 (5)	0.010			
	Au-Au	8.4 (3)	2.82 (6)	0.008	3 (1)	0.02	1.42
Au A2	Au-Au	2 (1)	4.03 (4)	0.008			
	Au-Au	5 (2)	4.95 (4)	0.010			
	Au-Au	9.5 (3)	2.83 (5)	0.008	3 (1)	0.02	1.97
Au A3	Au-Au	3 (1)	4.03 (5)	0.008			
	Au-Au	6 (2)	4.95 (5)	0.010			
	Au-Au	11.2 (4)	2.84 (4)	0.008	3 (1)	0.01	-
Au A4	Au-Au	4 (1)	4.04 (4)	0.008			
	Au-Au	10 (3)	4.98 (2)	0.010			
	Au-Au	7.7 (4)	2.82 (1)	0.008	3 (1)	0.03	1.18
Au B1	Au-Au	1 (2)	4.43 (8)	0.008			
	Au-Au	4 (3)	4.94 (4)	0.010			
	Au-Au	7.9 (4)	2.82 (1)	0.008	3 (1)	0.03	1.24
Au B2	Au-Au	2 (1)	4.00 (4)	0.008			
	Au-Au	5 (3)	4.93 (4)	0.010			
	Au-Au	10.6 (5)	2.84 (1)	0.008	3 (1)	0.02	-
Au B3	Au-Au	4 (2)	4.04 (3)	0.008			
	Au-Au	9 (3)	4.95 (2)	0.010			
	Au-Au	8.9 (4)	2.83 (1)	0.008	3 (1)	0.02	1.63
Au C1	Au-Au	2 (1)	4.03 (5)	0.008			
	Au-Au	7 (3)	4.96 (3)	0.010			
	Au-Au	9.8 (5)	2.83 (1)	0.008	3 (1)	0.03	2.23
Au C2	Au-Au	1 (2)	4.4 (1)	0.008			
	Au-Au	7 (3)	4.95 (3)	0.010			

[a] Fitting parameters: $S_o^2 = 0.80$ as deduced by Au foil standard; Fit range $3.5<k<13$, $1.15<R<5$; # of independent points = 23

[b] $2\sigma^2$ / Å^2 values fixed with no associated error

3.8. DRIFTS

CO-adsorption studies were used to assess qualitatively the nature of the available Au surface sites, with the spectra shown in figure 9. The CO adsorption bands for the Au catalysts prepared in H_2O at 1 and 25°C (A1 and A2) have more defined, sharper CO adsorption bands compared to the catalyst prepared at 50°C (A3). A high population of CO on to a single type of site affords a sharp band, whereas distribution over many different types of site results in a broader band. As regards the electronic properties at the Au/TiO_2 interface, previous literature has been used to assign the observed bands. The small band at ~ 2115 cm^{-1} present in the CO adsorption spectra of A1 and A2 (labelled i) can be assigned to CO–Au^0 species.[34] The broad band ~ 2040 cm^{-1} observed for each sample (labelled ii) is assigned to CO–$Au^{\delta-}$, as a result of electronic transfer from the reducible TiO_2 support to very small gold particles or clusters.[35-36] For A1 and A2 samples, it is evident from the asymmetric nature of this band that it comprises two different adsorption sites. The bands present below 1900 cm^{-1} (labelled iii) are more difficult to assign from the literature, with only bridge bonded CO on Au_5 clusters reported at this wavenumber to our knowledge.[37] The spectra of B1 and C1 catalysts resemble that of A3, with broad bands indicating a wider range of Au sites exist. The breadth associated with the CO adsorption bands for samples A3, B1 and C1 can be attributed to the dipole coupling effect between neighbouring CO molecules: when CO coverage is large, the dipoles between CO molecules couple, broadening the adsorption band. The sharp absorption bands observed in A1 and A2 provide evidence that there is limited coupling, confirming that the sites are more isolated (edge, step or corner sites). It is understandable that for the larger Au particle containing catalysts, the CO bands are broader, but it is difficult to ascribe the broad bands observed in catalyst B1, in which the smallest Au particles exist. The only factor can be associated with the influence of the stabilising agent, PVA, on the Au species during the catalyst preparation in different solvents. The interaction between PVA and the EtOH solvent appears detrimental to the available Au sites for CO-adsorption. The samples of interest were not pre-treated in any way in order to clean the catalyst surface or to modify the electronic properties. Hence in all cases the stabilizing agent, PVA, may crucially inhibit the ability of each sample to adsorb CO at the surface. As a result, facile removal of the stabilizing agent has been widely investigated, with the aim of

removing the protecting agent without affecting the structure of the catalyst. Despite several efforts, it still not certain if this can be achieved.[38]

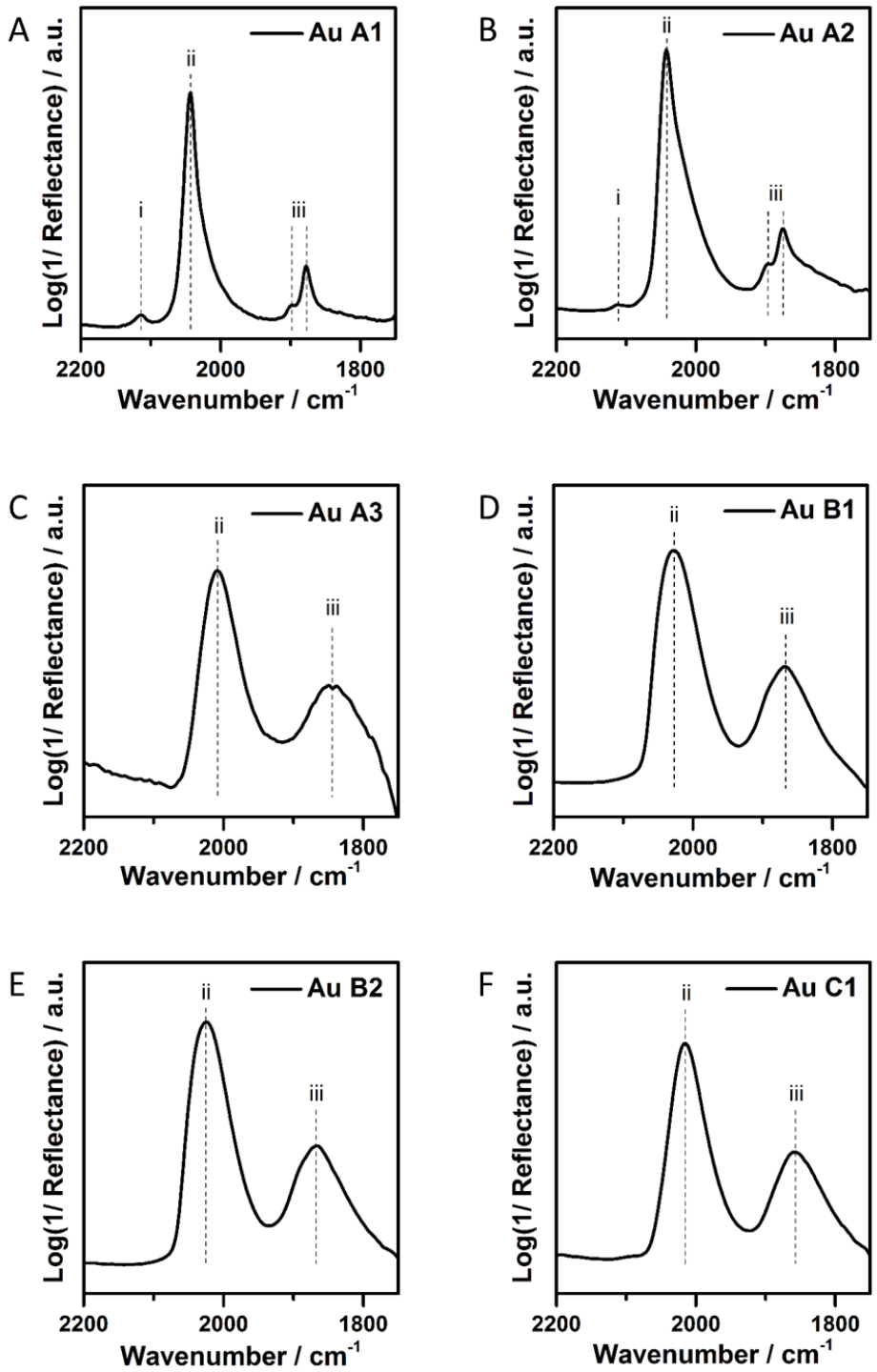

Figure 9. FTIR spectra from CO-adsorption studies on Au/TiO_2 catalysts prepared at different temperatures under varied solvent environments; A) 1°C H_2O A1, B) 25°C H_2O A2, C) 50°C H_2O A3, D) −30°C H_2O:EtOH B1, E) 1°C H_2O:EtOH B2 and F) −75°C EtOH C1.

3.9. Computational IR

All computational studies for the present chapter were performed by Anna Gould and Dr. Andrew Logsdail from UCL.

The HAADF STEM images clearly indicate there are extremely small gold clusters, and from the experimental IR, there are CO-chemisorption bands below 1900 cm^{-1} that are tentatively assigned to small Au cluster bands . These lower energy peak positions are not well documented for gold nanoclusters, but have been found in calculations on Au_5CO and $Au_{13}CO$ by Jian and Xu[37] and Phala *et al,*[39] respectively, where the CO molecule binds favorably at a bridged site in both cases. Computational studies were used to corroborate with the experimental IR data obtained, investigating CO-chemisorption on small Au clusters.

Methods: The geometries for small Au-CO clusters were taken from the previous work of Jiang and Xu,[37] and geometry optimisations were performed. DFT calculations were performed as implemented by the projector-augmented wave method (PAW).[40] Grid-based PAW (GPAW) uses a real-space grid, transforming the wavefunctions at the core to a smooth pseudo-wavefunction.[41] A converged grid spacing of 0.18 was used to represent numerically the wavefunction, and structural convergence was achieved when the forces on all atoms were found to be < 0.01 eV $Å^{-1}$.

The molecules investigated were: Au_5CO, Au_4CO, Au_3CO, Au_2CO, $Au_2(CO)_2$, $Au(CO)_2$, and AuCO. Depending on the number of electrons in the system, spin polarized (Au_5CO, Au_3CO, $Au(CO)_2$ and AuCO) and spin-paired (Au_4CO, Au_2CO, $Au_2(CO)_2$) calculations were performed for odd- and even- electron systems, respectively, with the generalized gradient approximation (GGA) or Perdew, Burke and Ernzerhof (PBE) as the exchange-correlation functional;[42] the residual minimisation method, direct inversion in iterative subspace (RMM-DIIS) was used for convergence of the self-consistent cycle. For the odd-electron systems a low-spin doublet configuration (μ=1) was energetically preferable in all cases. The IR vibrational frequencies were calculated using finite difference methods, and compared to CO in the gas-phase, and adsorbed at varying sites on Au (100) and (111) surfaces: namely the atop, bridge, hollow sites on the (100) surface; and the atop, bridge, hcp and fcc sites on the (111) surface. In addition the Au surface was modelled using a 5-layer thick slab with 2D periodicity, using 1 k-point per 0.024 $Å^{-1}$ in the directions parallel to the surface plane (i.e. x- and y-). These studies show that the calculation of

stretching frequencies may be limited to the contributions of the CO molecule and Au atoms that are directly bound to it, with all other atoms frozen, thus significantly reducing the computational requirement. Finally, the influence of charge on the vibrational frequencies is considered, to simulate the effect of the charge donating TiO_2 support. Geometry optimization and vibrational frequency analysis was performed on small Au_xCO clusters and for CO adsorbed at varying sites on (100) and (111).

Results: The calculations show that the relevant vibrational modes in the IR spectra may be restricted to those relating to the CO molecule and directly bonded Au atoms. The CO stretching frequencies for selected Au_xCO clusters and surface adsorption sites are given in table 5. From the results outlined, it is observed that the CO stretching frequencies, when adsorbed on small gold clusters, are lower than for gas-phase CO and similar to the slab calculations where the CO molecule is adsorbed in an atop position, with a vibrational frequency of ~ 2090 cm^{-1}. However, when CO binds in a bridging fashion, the vibrational frequency is shifted to considerably lower wavenumbers on the (100) and (111) surfaces. Both Au_3CO and Au_5CO molecules have CO positioned in a bridging arrangement, yet the CO stretching frequency for the Au_5CO is much lower, at 1869.9 cm^{-1}. This result suggests that CO stretching frequencies below 1900 cm^{-1} may be assigned to bridging positions for the CO adsorbate on small Au clusters, and may therefore correspond to the unusually distinct peaks highlighted in figure 10.

To understand the influence of the charge donating supports, TiO_2, on the CO stretching frequencies, the Au_5CO molecule was negatively charged before re-optimisation of the geometry and recalculation of the vibrational frequencies. This procedure resulted in a significant red shift of the CO stretching frequency by 102.7 cm^{-1}, from 1869.9 to 1767.2.9 cm^{-1}. Given also the electronegative nature of Au, such a shift perhaps indicates that lower CO stretching frequencies in the experimental IR spectra could also arise from nanoparticle interactions with the substrate.

CO adsorption onto varying Au surfaces [(111), (100), (110), (310)] exhibits stretching frequencies < 2000 cm^{-1} when the CO molecule is in a bridged arrangement,[43] and thus the peaks significantly below this threshold can be attributed to bridging CO molecules.

Table 5. Calculated CO vibrational frequencies of gas-phase CO, small Au_xCO clusters and CO adsorbed on to (100) and (111) surface slabs. The (100) hollow site is unstable for CO adsorption.

Structure	Adsorption site	CO vibrational frequency / cm^{-1}	Experimental ($^{12}C^{16}O$) / cm^{-1}
CO	gas-phase	2134.6	
AuCO	atop	1998.7	2039.3
Au_2CO	atop	2108.3	2131.9
$Au_2(CO)_2$	atop	2113.5	2110.2
Au_3CO	bridge	2084.3	2075.4
Au_4CO	atop	2096.1	2115.9
Au_5CO	bridge	1869.9	1852.9
$[Au_5CO]^-$	bridge	1767.2	
Au (100)	atop	2085.4	
Au (100)	bridge	1976.7	
Au (100)	hollow	Not stable	
Au (111)	atop	2082.6	
Au (111)	bridge	1998.7	
Au (111)	hcp	1941.1	
Au (111)	fcc	1944.9	

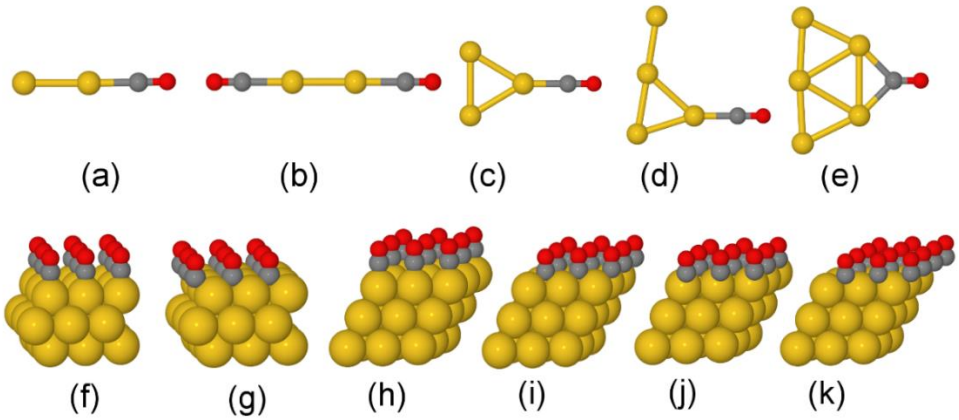

Figure 10. (a) Au_2CO, (b) Au_2CO_2, (c) Au_3CO, (d) Au_4CO, (e) Au_5CO, (f) Au(100) atop, (g) Au(100) bridge, (h) Au(111) atop, (i) Au(111) bridge, (j) Au(111) fcc hollow, (k) Au(111) hcp hollow. Yellow, grey and red spheres represent gold, carbon and oxygen, respectively.

3.10. Catalytic Testing: Liquid Phase Oxidation of Glycerol

All Au/TiO_2 catalysts were evaluated for the liquid phase oxidation of glycerol under standard conditions, as described in chapter 2, section 11. The experiments were performed over a four hour period, with the time online glycerol conversion profiles illustrated in figure 11. The initial rate of reaction appears to be dependent on the solvent choice used during catalyst preparation. For the catalysts prepared in water there is no indication of an induction period, whereas for those prepared in H_2O:EtOH and EtOH solvents, an induction period ~ 15 minutes is observed. It is clear that the presence of EtOH during catalyst preparation influences the initial reaction activity. EtOH probably inhibits reactant accessibility to the Au surface either by: influencing the binding of PVA with the Au surface or directly from residual EtOH. After the initial induction period, the glycerol conversion is faster for the catalysts prepared at lower temperatures in a H_2O solvent.

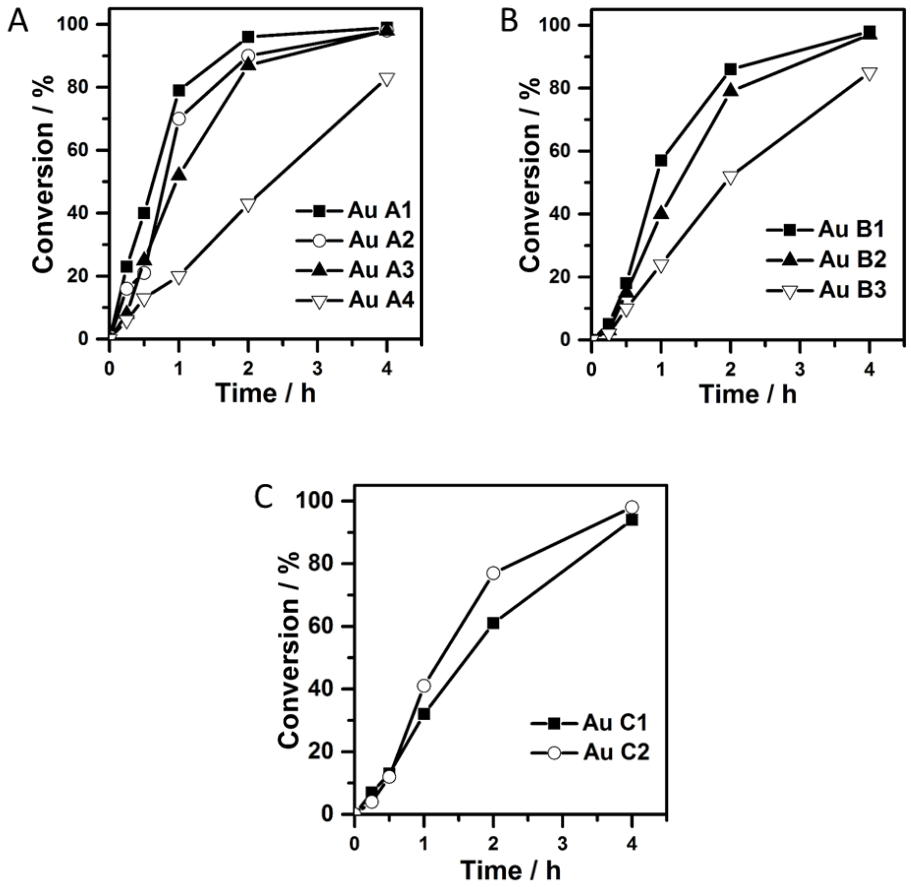

Figure 11. Time online conversion profiles for each Au/TiO_2 catalyst prepared at different temperatures in varied solvent environments.

The catalytic performances of each Au/TiO_2, in terms of activity (TOF) and product selectivity, are reported in figure 12. The presence of base in the reaction means all products are present in salt form. The Au/TiO_2 catalysts prepared in water showed the best catalytic performance compared to the alternative solvent systems, with A1 being the most active catalyst (TOF of 915 h^{-1}). This value, when compared to the limited number of previously reported Au/TiO_2 catalysts, is high. Au/TiO_2 previously prepared by deposition precipitation or synthesized using colloidal methods with Tetrakis(hydroxymethyl)phosphonium chloride (THPC) as the stabilizing agent generated TOFs of 721 and 367 h^{-1}, respectively.[44] The standard sol-immobilisation method, in which the preparation conditions are equivalent to A2 in this study, has a lower activity than A1 (TOF of 663 hr^{-1}). The marked improvement in activity is attributed to the high population of ultra-small Au clusters present for the A1 catalyst, which are thought to be the highly active species. As mentioned earlier, it is possible that the other Au catalysts do comprise ultra-small clusters, but their populations are lower, consistent with the observed activities. A3 and A4 have significantly lower activities than A1 (TOF of 341 and 161 h^{-1}, respectively), with the higher temperatures of preparation causing cluster aggregation. All Au catalysts show very similar selectivity profiles, with the selectivity to glycerate between 73 and80%. The selectivity to glycerate is inversely correlated to Au particle size, with the smaller, more active particles also exhibiting higher selectivity to over-oxidation products (tartronate). The observed trend in selectivity, as previously mentioned, is common for Au catalysts but the similar profiles for all catalysts is interesting considering the differing available Au sites confirmed by IR. Correlating the activity data for all Au catalysts with the average Au particle sizes showed that this is not the only parameter influencing the catalytic performance (activity). Indeed A1, A2, B1, B2 and C1 catalysts showed different catalytic behaviour, despite the similar Au average particle diameter (1.8-2.4 nm). The difference can be attributed to two factors: 1) the population of very small Au clusters as seen in A1 and 2) the interaction between protecting agent and solvent system, which is influenced by the temperature and the solvent in which the Au nanoparticles are generated. It has previously been demonstrated that PVA affects the catalytic performance, as it is proposed that PVA can direct the adsorption of glycerol to Au active sites by interacting with the OH groups of glycerol.[26-27] There is an interesting result for the C series, where the larger

Au particle size catalyst, C2, has a greater activity than the smaller C1. We also attribute this trend to differences in the way PVA interacts with the Au colloids as a consequence of the low solubility of PVA in ethanol, which is exacerbated by the low temperature synthesis. We suggest that EtOH may also interact with the PVA at the nanoparticle surface, and hence influence the adsorption of glycerol, essentially inhibiting its conversion.

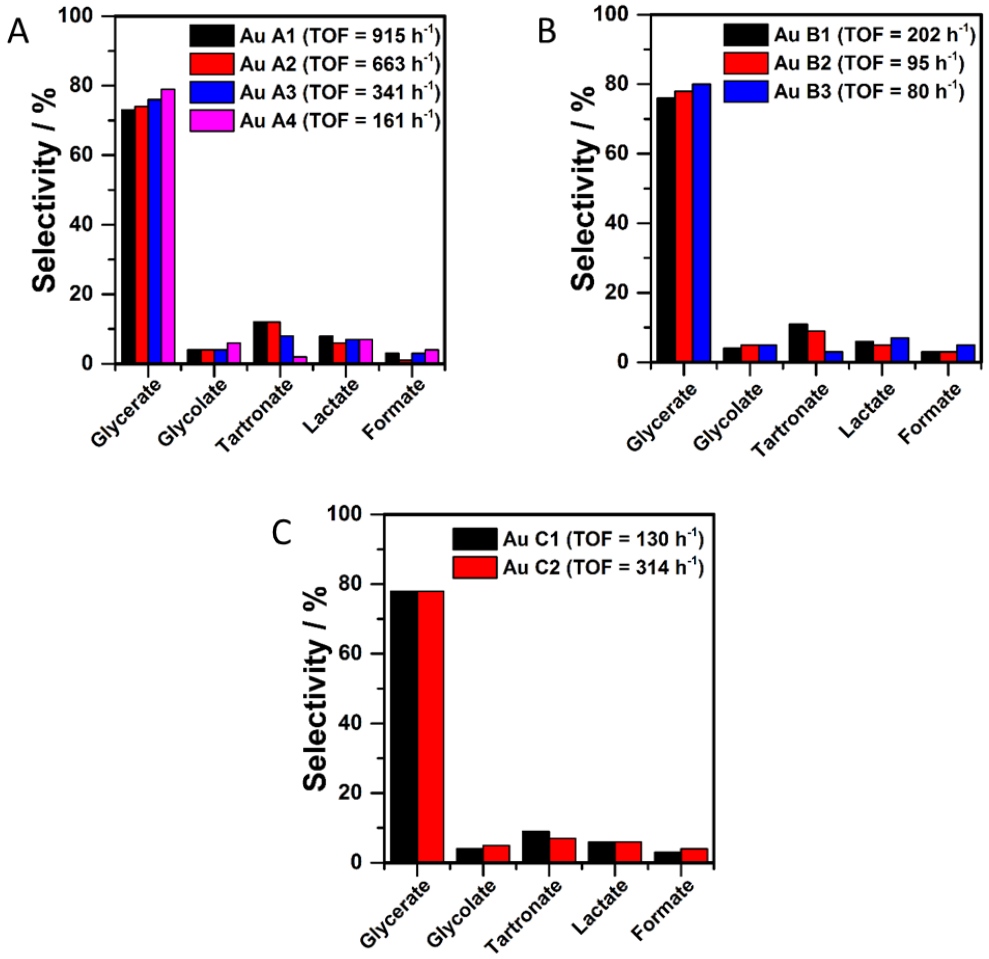

Figure 12. Activity and selectivity profiles for each Au/TiO_2 catalyst, as well as the TOF calculated after 15 minutes of reaction. TOF calculated after 15 minutes of reaction defined as the moles of glycerol converted per mole of Au per hour.

To explore the effect of solvent used for the preparation of Au catalysts on their stability, the recyclability of the catalysts was investigated over 10 successive runs. The most active catalysts for each solvent (A1, B1 and C2) were chosen. The catalysts showed good stability after 10 runs, reaching full conversion after 4h (table 6, 7 and 8). A1 showed a decreasing of TOF between the first and second run (915 and 652 h-

[1]). Afterwards, the TOF remained constant in the successive 8 runs (table 5). The selectivity to glycerate decreased from 73% of the first run to 56% of the second run, where a higher amount of tartronate was produced. This result can be attributed to the change in the average particle size of the A1 catalyst after the first run, with the aggregation of the very small Au clusters that were observed in HAADF STEM analysis. There was indeed an increase in average Au particle diameter before and after the recycling tests from 2.0 to 3.7 nm, by TEM (figures 13A and 14A). Au/TiO_2 prepared in H_2O:EtOH and EtOH showed an increased TOF after the second run (tables 7 and 8), which remained stable in the successive runs, despite the obvious growth in Au particle diameters to 4.5 (+ 2.7) and 4.4 (+ 1.5) nm, respectively. The catalyst stability is prolonged by the presence of the protecting agent, which is consistent with the lower activity observed for catalysts prepared in solvents containing EtOH, in which the solvent of preparation and PVA/Au interaction both influence the sites available for glycerol adsorption.

Table 6. Recycling results using the A1 Au catalyst (prepared in H_2O at 1°C).

A1[a]	TOF (h^{-1})[b]	Conv. (%) after 4h	Selectivity (%) [c]			
			Glyc	Gly	Tartr	Lac
Run 1	915	98	73	4	12	8
Run 2	652	98	56	6	22	9
Run 3	678	99	57	6	25	9
Run 4	659	98	59	6	23	9
Run 5	649	98	57	9	24	6
Run 6	657	97	56	11	23	7
Run 7	638	98	57	10	24	7
Run 8	652	98	58	11	24	6
Run 9	649	98	56	10	22	6
Run 10	632	99	58	12	22	7

Table 7. Recycling results using the B1 Au catalyst (prepared in H_2O:EtOH at −30°C).

B1[a]	TOF (h^{-1})[b]	Conv. (%) after 4h	Selectivity (%) [c]			
			Glyc	Gly	Tartr	Lac
Run 1	202	94	76	4	11	6
Run 2	256	98	67	11	12	7
Run 3	261	98	62	7	21	8
Run 4	265	95	60	8	21	9
Run 5	263	98	61	7	19	9
Run 6	258	99	60	7	22	8
Run 7	246	94	60	8	21	8
Run 8	269	96	58	10	22	7
Run 9	259	97	56	10	22	9
Run 10	250	93	58	10	22	7

[a] Reaction condition: Glycerol/metal molar ratio = 1000, 50 °C, pO2 300 kPa, 1250 rpm. [b] TOF calculated after 15 min of reaction. [c] Selectivity at 90% conversion. Glyc = glycerate; Gly = glycolate; Tartr = tartronate; Lac = lactate.

Table 8. Recycling results using the C2 Au catalyst (prepared in EtOH at −30°C).

C2[a]	TOF (h^{-1})[b]	Conv. (%) after 4h	Selectivity (%) [c]			
			Glyc	Gly	Tartr	Lac
Run 1	314	94	78	5	7	6
Run 2	415	97	76	4	5	10
Run 3	421	98	64	5	9	10
Run 4	432	98	66	4	14	15
Run 5	425	98	65	6	15	13
Run 6	412	99	66	6	15	12
Run 7	408	99	66	6	16	11
Run 8	419	96	66	6	15	11
Run 9	402	98	67	6	14	11
Run 10	389	97	65	7	14	12

[a] Reaction condition: Glycerol/metal molar ratio = 1000, 50 °C, pO2 300 kPa, 1250 rpm. [b] TOF calculated after 15 min of reaction. [c] Selectivity at 90% conversion. Glyc = glycerate; Gly = glycolate; Tartr = tartronate; Lac = lactate.

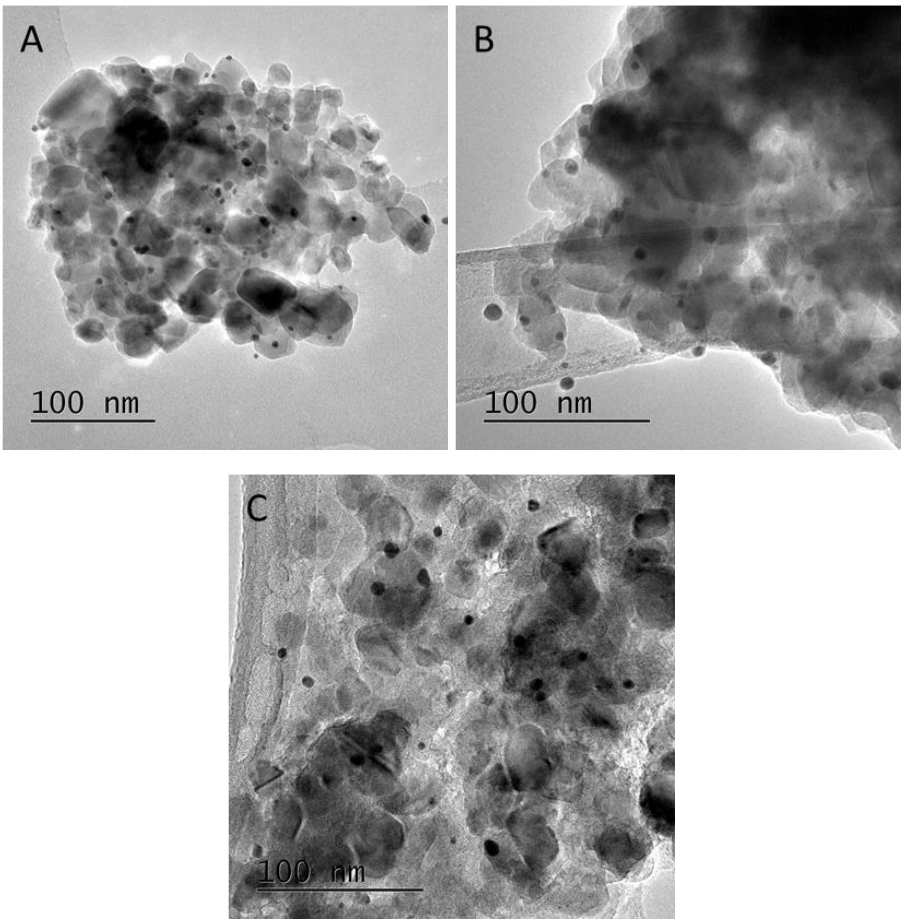

Figure 13. TEM images for the recovered Au/TiO_2 catalysts used in the liquid phase oxidation of glycerol at 50°C; A) 1°C H_2O A1, B) −30°C H_2O:EtOH B1 and C) −30°C EtOH C2.

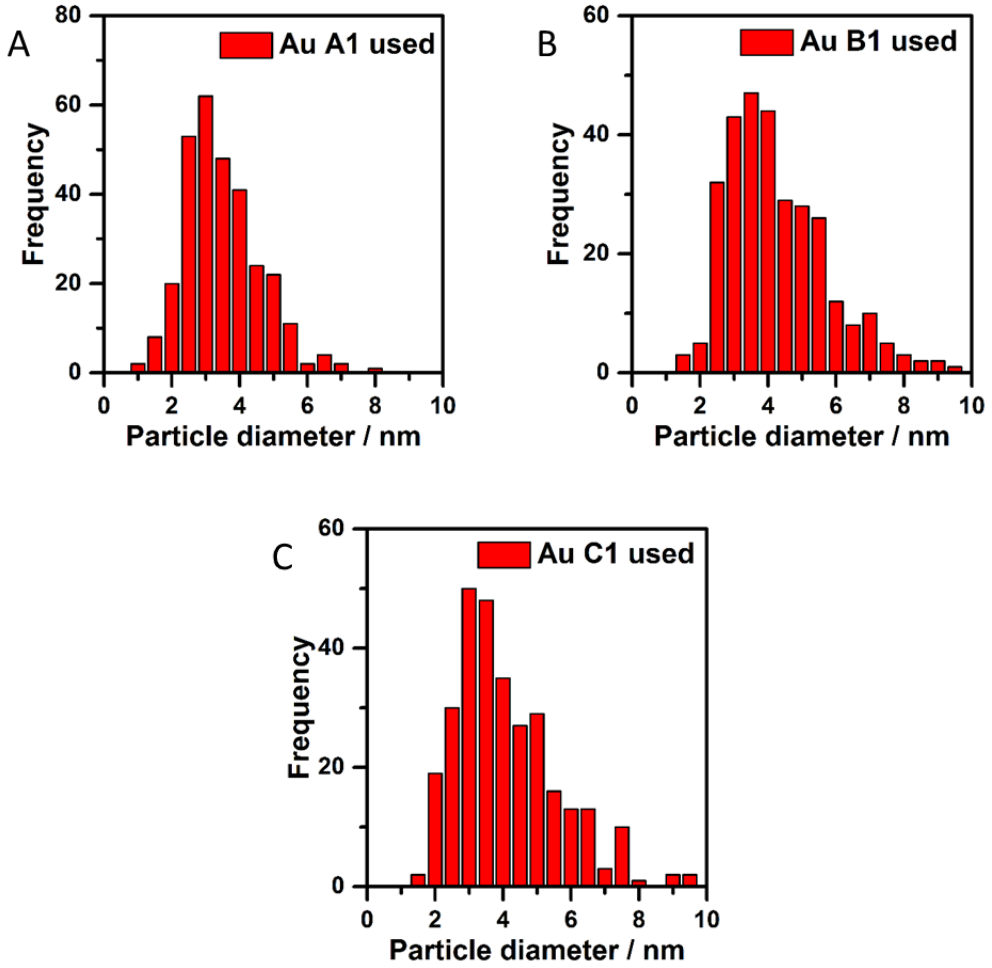

Figure 14. Au particle size histogram for the recovered Au/TiO_2 catalysts used in the liquid phase oxidation of glycerol at 50°C; A) 1°C H_2O A1, B) −30°C H_2O:EtOH B1 and C) −30°C EtOH C2.

4. Summary and Conclusions

The standard sol-immobilisation method using PVA and $NaBH_4$ as stabilising and reducing agents, respectively, is an effective method to prepare small metal nanoparticles with a narrow particle distribution. The smallest Au metal nanoparticles, 1.8 nm by TEM, were afforded when the catalyst preparation was performed at −30°C in a mixed H_2O:EtOH solvent. The results in this study demonstrates how Au nanoparticle characteristics can be systematically tuned using solvent and temperature variations during colloidal synthesis and the impact this has on catalytic performance, specifically for the liquid phase oxidation of glycerol.

The choice of temperature and solvent system during Au/TiO_2 synthesis proved crucial in dictating the performance for the liquid phase oxidation of glycerol, with the Au/TiO_2 catalyst, in which the colloid was generated at 1 °C in a water-only solvent, giving the highest activity. With a TOF of 915 h^{-1}, this compares very favourably not only other Au/TiO_2, but to carbon supported metal catalysts previously assessed under similar reaction conditions. The characterisation of this catalyst, A1, demonstrated the presence of isolated ultra-small Au clusters (1-5 atoms) in high population as shown by HAADF STEM, which is also supported by CO adsorption IR studies showing bands below 1900 cm^{-1} corroborated with theoretical studies. From this study, it is understood that Au particle size is not the only factor affecting catalytic performance, as catalysts with similar average Au particle diameter - A1 and B2, as identified by EXAFS and TEM - gave rise to different catalytic properties, with TOF values of 915 h^{-1} and 95 h^{-1}, respectively. This insight is of great importance when trying to elucidate accurate structure function relationships. Despite the low activity, it was also concluded that the presence of EtOH during catalyst preparation increased the Au/TiO_2 durability, which again was attributed to the EtOH at the Au surface interacting with the PVA and glycerol through the hydroxyl groups. This study links performance of Au/TiO_2 catalysts for glycerol oxidation to the population of specific cluster sizes, and also indicated that reduced average particle diameter alone is not sufficient to promote the reaction. The interaction between the PVA and the Au nanoparticles should not be ignored, and may also influence the types/number of Au aggregates formed alongside affecting which sites are available.

5. References

1. Quispe, C. A. G.; Coronado, C. J. R.; Carvalho Jr, J. A. *Renewable and Sustainable Energy Reviews,* 2013**, *27***, 475-493.
2. Momirlan, M.; Veziroglu, T. N. *International Journal of Hydrogen Energy,* 2005**, *30*** (7), 795-802.
3. Behr, A.; Eilting, J.; Irawadi, K.; Leschinski, J.; Lindner, F. *Green Chemistry,* 2008**, *10*** (1), 13-30.
4. . *Ullmann's Encyclopedia of Industrial Chemistry Wiley-VCH,* 2002**,** (electronic release).
5. Sheldon, R. A.; Arends, I. W. C. E.; Dijksman, A. *Catalysis Today,* 2000**, *57*** (1–2), 157-166.
6. Prati, L.; Villa, A.; Chan-Thaw, C. E.; Arrigo, R.; Wang, D.; Su, D. S. *Faraday Discussions,* 2011**, *152*** (0), 353-365.
7. Sheldon, R. A.; Kochi, J. K. *Metal-catalyzed Oxidations of Organic Compounds,* Kochi, R. A. S. K., Ed. Academic Press, 1981; pp 1-14.
8. Carrettin, S.; McMorn, P.; Johnston, P.; Griffin, K.; Kiely, C. J.; Hutchings, G. J. *Physical Chemistry Chemical Physics,* 2003**, *5*** (6), 1329-1336.
9. Dimitratos, N.; Villa, A.; Wang, D.; Porta, F.; Su, D.; Prati, L. *Journal of Catalysis,* 2006**, *244*** (1), 113-121.
10. Prati, L.; Spontoni, P.; Gaiassi, A. *Topics in Catalysis,* 2009**, *52*** (3), 288-296.
11. Zhu, J. J.; Figueiredo, J. L.; Faria, J. L. *Catalysis Communications,* 2008**, *9*** (14), 2395-2397.
12. Ide, M. S.; Davis, R. J. *Accounts of Chemical Research,* 2014**, *47*** (3), 825-833.
13. Prati, L.; Rossi, M. *Journal of Catalysis,* 1998**, *176*** (2), 552-560.
14. Dimitratos, N.; Porta, F.; Prati, L. *Applied Catalysis A: General,* 2005**, *291*** (1–2), 210-214.
15. Besson, M.; Gallezot, P. *Catalysis Today,* 2000**, *57*** (1–2), 127-141.
16. Porta, F.; Prati, L.; Rossi, M.; Scari, G. *Journal of Catalysis,* 2002**, *211*** (2), 464-469.
17. Porta, F.; Prati, L. *Journal of Catalysis,* 2004**, *224*** (2), 397-403.
18. Carrettin, S.; McMorn, P.; Johnston, P.; Griffin, K.; Hutchings, G. J. *Chemical Communications,* 2002**,** (7), 696-697.
19. Demirel-Gülen, S.; Lucas, M.; Claus, P. *Catalysis Today,* 2005**, *102–103*** (0), 166-172.
20. Ketchie, W. C.; Fang, Y. L.; Wong, M. S.; Murayama, M.; Davis, R. J. *Journal of Catalysis,* 2007**, *250*** (1), 94-101.

21. Carrettin, S.; McMorn, P.; Johnston, P.; Griffin, K.; Kiely, C.; Attard, G.; Hutchings, G. *Topics in Catalysis,* 2004**, *27*** (1-4), 131-136.
22. Dimitratos, N.; Villa, A.; Bianchi, C. L.; Prati, L.; Makkee, M. *Applied Catalysis a-General,* 2006**, *311***, 185-192.
23. Enache, D. I.; Edwards, J. K.; Landon, P.; Solsona-Espriu, B.; Carley, A. F.; Herzing, A. A.; Watanabe, M.; Kiely, C. J.; Knight, D. W.; Hutchings, G. J. *Science,* 2006**, *311*** (5759), 362-365.
24. Dimitratos, N.; Villa, A.; Prati, L.; Hammond, C.; Chan-Thaw, C. E.; Cookson, J.; Bishop, P. T. *Applied Catalysis A: General,* 2016**, *514***, 267-275.
25. Dimitratos, N.; Lopez-Sanchez, J.; Lennon, D.; Porta, F.; Prati, L.; Villa, A. *Catalysis Letters,* 2006**, *108*** (3-4), 147-153.
26. Villa, A.; Wang, D.; Veith, G. M.; Vindigni, F.; Prati, L. *Catalysis Science & Technology,* 2013**, *3*** (11), 3036-3041.
27. Prati, L.; Villa, A. *Accounts of Chemical Research,* 2014**, *47*** (3), 855-863.
28. Yu, J. C.; Yu; Ho; Jiang; Zhang. *Chemistry of Materials,* 2002**, *14*** (9), 3808-3816.
29. Bianchi, C. L.; Canton, P.; Dimitratos, N.; Porta, F.; Prati, L. *Catalysis Today,* 2005**, *102–103***, 203-212.
30. Underwood, S.; Mulvaney, P. *Langmuir,* 1994**, *10*** (10), 3427-3430.
31. Salvati, R.; Longo, A.; Carotenuto, G.; De Nicola, S.; Pepe, G. P.; Nicolais, L.; Barone, A. *Applied Surface Science,* 2005**, *248*** (1–4), 28-31.
32. Beale, A. M.; Weckhuysen, B. M. *Physical Chemistry Chemical Physics,* 2010**, *12*** (21), 5562-5574.
33. Szczerba, W.; Riesemeier, H.; Thunemann, A. F. *Analytical and Bioanalytical Chemistry,* 2010**, *398*** (5), 1967-1972.
34. Dekkers, M. A. P.; Lippits, M. J.; Nieuwenhuys, B. E. *Catalysis Letters,* 1998**, *56*** (4), 195-197.
35. Boccuzzi, F.; Chiorino, A.; Manzoli, M.; Andreeva, D.; Tabakova, T. *Journal of Catalysis,* 1999**, *188*** (1), 176-185.
36. Panayotov, D. A.; Burrows, S. P.; Yates, J. T.; Morris, J. R. *The Journal of Physical Chemistry C,* 2011**, *115*** (45), 22400-22408.
37. Jiang, L.; Xu, Q. *The Journal of Physical Chemistry A,* 2005**, *109*** (6), 1026-1032.
38. Lopez-Sanchez, J. A.; Dimitratos, N.; Hammond, C.; Brett, G. L.; Kesavan, L.; White, S.; Miedziak, P.; Tiruvalam, R.; Jenkins, R. L.; Carley, A. F.; Knight, D.; Kiely, C. J.; Hutchings, G. J. *Nature Chemistry,* 2011**, *3*** (7), 551-556.
39. Phala, N. S.; Klatt, G.; Steen, E. v. *Chemical Physics Letters,* 2004**, *395*** (1–3), 33-37.
40. Blöchl, P. E. *Physical Review B,* 1994**, *50*** (24), 17953-17979.

41. Mortensen, J. J.; Hansen, L. B.; Jacobsen, K. W. *Physical Review B,* 2005**, *71*** (3), 035109.

42. Perdew, J. P.; Burke, K.; Ernzerhof, M. *Physical Review Letters,* 1996**, *77*** (18), 3865-3868.

43. Hussain, A.; Curulla Ferré, D.; Gracia, J.; Nieuwenhuys, B. E.; Niemantsverdriet, J. W. *Surface Science,* 2009**, *603*** (17), 2734-2741.

44. Dimitratos, N.; Villa, A.; Bianchi, C. L.; Prati, L.; Makkee, M. *Applied Catalysis A: General,* 2006**, *311*** (0), 185-192.

Chapter Four. Pd/TiO_2 for the Hydrogenation of Furfural

In chapter 3, the modified sol-immobilisation method, employing varied temperature and solvent environments, was used to prepare Au/TiO_2 catalysts. Despite being a successful approach in the tailoring of metal nanoparticle properties, it is important to demonstrate that the method can be applied to other metals. Hence, in the current chapter, the same preparation conditions are used to prepare Pd/TiO_2, and the resulting catalysts tested for their performance in the hydrogenation of furfural.

1. Introduction

Biorefining, the process in which biomass is converted to useful products, has great importance in the sustainable production of energy and chemicals. The production and utilization of first generation biofuels, described as fuels derived from food sources such as corn, wheat and sugarcane has drawbacks due to their high cost, as well as the debate as to whether the sources should supply food or fuel.[1] Therefore second generation biofuels, in which the fuels are derived from non-edible plant sources, alleviate both cost and ethical issues. These sources are lignocellulosic in origin, comprised of 30-60% cellulose, 20-40% hemicellulose and 15-25% lignin based on a moisture free basis,[1] and the upgrading is based on two main routes, thermo- and bio-chemical. Thermochemical routes includes pyrolysis, liquefaction and gasification, whereas biochemical transformation involves hydrolysis with dilute acids and enzymes. The latter route (biochemical) unlocks valuable sugars from hemicellulose, which can be upgraded further to platform molecules.[2]

The hydrolysis of hemicellulose yields many different sugar monomers, but xylose is the major product that can be subsequently acid catalyzed to the valuable intermediate, furfural.[3] It is reported that 400,000 tons of furfural is produced a year, worldwide,[3] as it is an important precursor in the generation of biofuels[4-5] and chemical intermediates.[6] Based on the high chemical reactivity, there are many possible transformations furfural can undergo to yield useful products, mainly based on hydrogenation, decarbonylation, hydrogenolysis or combinations thereof, as depicted

in scheme 1. Decarbonylation of furfural yields furan, a common organic solvent, whereas hydrogenolysis of furfural yields methyl furan, which is used for the production of pesticides, perfumes and antimalarial drugs.[7]

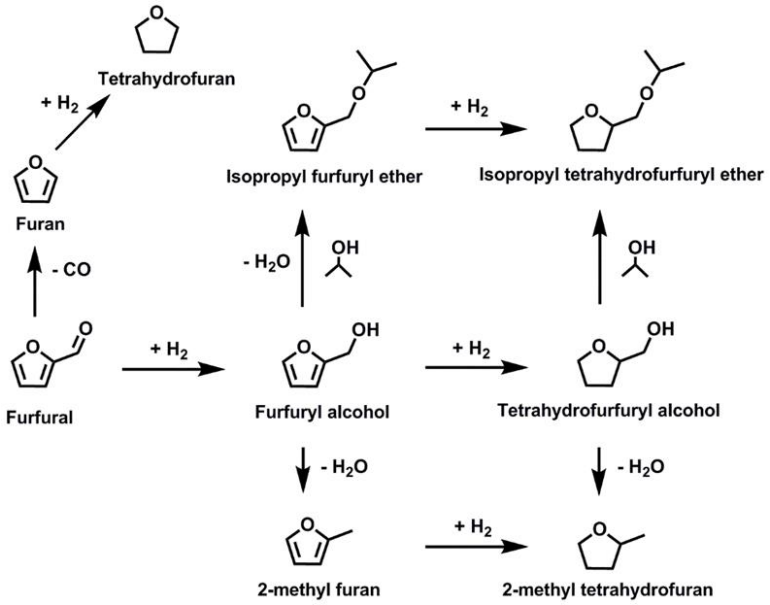

Scheme 1. The reaction pathways during furfural hydrogenation.[8]

Furfuryl alcohol, used in the manufacture of resins, adhesives, and synthetic fibres,[9] is produced from the selective hydrogenation of furfural (scheme 1). Subsequent hydrogenation of furfuryl alcohol produces tetrahydrofurfuryl alcohol, a 'green solvent', often used in printer inks and agricultural applications.[10] Ultimately, the hydrogenation of furfural results in a complex network of products, where there is a need to control the relative distribution. For α,β-unsaturated carbonyl compounds, hydrogenation of C=C is both thermodynamically and kinetically favored over C=O,[11] and therefore the challenge is to find a selective catalyst that has control over C=C or C=O hydrogenation and disfavors alternative pathways, e.g. decarbonylation.

Many heterogeneous catalysts have been investigated for the hydrogenation of furfural, with the majority of studies focusing on Cu, Ni,[12] Ru,[13] or Pd[14-15] based systems. Cu, in the form of Cu chromite,[16] or supported forms,[17-20] have been commonly used, and show good selectivity to furfuryl alcohol as a consequence of the preference of Cu to bind C=O, over C=C.[20] Ni catalysts show different product distribution to Cu, with the primary step favoring decarbonylation, with secondary paths including opening of the furan ring.[21] Another downfall of Ni catalysts for this reaction is the rate at which the metal leaches in liquid phase systems, and therefore

only reactions in the vapor phase are permitted.[14] Pd is an ideal catalyst for hydrogenation processes as it readily dissociates hydrogen under ambient conditions. Recent studies have shown that Pd/TiO_2 based systems are able to hydrogenate furfural effectively at mild conditions (room temperature, 1-3 bar hydrogen).[22-24] The studies focused on Pd nanoparticles prepared by incipient wetness impregnation and showed that methyl furan and furfuryl alcohol were the major products, and that the product distribution could be altered by changing the solvent of reaction and metal loading.[22] Indeed, the differences in furfural binding (η^1 CO, η^1 O, η^2 C-O, and η^2 C-C) and their preference on different crystal facets,[25-26] have been linked to differences in product selectivity for different particle sizes.[27]

During catalyst synthesis, the ability to generate only one type of site (edge, corner, terrace or particular facet) is challenging. As mentioned, different particle size results in different ratios of each site, but a mixture exists nevertheless. Therefore, the ability to manipulate the binding orientation of furfural on to specific metal sites, through the use of blocking agents, is a current research area of interest. Selective control of the hydrogenation pathway has been effectively achieved using self-assembled monolayers (SAMs) as blocking agents.[28-29] Medlin *et al.* used thiolates to selectively block sites that enable furfural to bind in a flat conformation, and hence prohibit the formation of unwanted carbonylation products, whilst leaving only isolated sites (corners, edges) exposed. These sites were found to be more selective towards hydrogenation products.

In this chapter, different temperature and solvent environments, similar to those employed to prepare Au/TiO_2 catalysts in chapter 3, are used to prepare Pd/TiO_2 catalysts, and the resulting catalysts tested for the hydrogenation of furfural at 25 and 50°C. It has already been demonstrated that similar Au particle sizes could be prepared in different solvent environments, but their activities towards glycerol oxidation are very different. Glycerol oxidation on Au occurs only at the primary alcohol, and thus there is no selectivity issue in the first step. In contrast, the different functional groups in furfural means initial selectivity is crucial, and may help elucidate the effect of solvent environment during synthesis, on the afforded metal particle properties. The Pd catalysts are characterized with TEM, STEM HAADF, XAFS, IR (CO-adsorption) and DFT studies to assess the Pd particle size, the nature of the Pd surface sites and the stability of the catalysts during catalysis at the different temperatures.

2. Experimental Details

2.1 Catalyst Synthesis

A modified sol-immobilisation method, as detailed in chapter 2, section 2, was used to prepare Pd/TiO_2 catalysts. All theoretical Pd loadings were 1 wt. % on to TiO_2 (P25) support. As mentioned, different temperatures and H_2O/EtOH solvent ratio were used during the catalyst preparation, with the conditions presented in table 1, as well as an abbreviated name to be used throughout the chapter. Dr Michal Perdjon-Abel was responsible for the preparation of some of the catalysts.

Table 1. Temperature and solvent environments to which each Pd/TiO_2 catalyst was prepared as well as the sample notation to be used throughout.

Temperature / °C	H_2O/EtOH solvent ratio (vol:vol)	Sample abbreviation
1	100	Pd A1
25	100	Pd A2
50	100	Pd A3
75	100	Pd A4
−30	50	Pd B1
1	50	Pd B2
25	50	Pd B3

2.2. UV-Vis, MP-AES, TEM, STEM HAADF and Transmission IR

The details of all the techniques used to characterise the catalysts can be found in chapter 2. Dr. Michal Perdjon-Abel performed TEM on some of the catalysts. Dr. Kristina Penman performed MP-AES analysis on the catalysts and Nan Jian from the University of Birmingham performed the STEM HAADF microscopy

2.3. Pd K edge XAFS Investigations

Pd K edge XAFS studies were carried out on the B18 beamline at the Diamond Light Source, Didcot, U.K. Measurements were performed in transmission mode using a QEXAFS set-up with a fast-scanning Si(311) double crystal monochromator and ion chamber detectors. The time resolution of the spectra was 1 min/spectrum (k_{max} = 18). On average, 15 scans were acquired to improve the signal-to-noise level of the data.

2.4. Catalytic Studies

See to chapter 2, section 12 for details regarding the catalytic hydrogenation of furfural performed using the Pd/TiO_2 catalysts. These experiments were performed by Dr. Alberto Villa and Dr. Carine Chan-Thaw at the University of Milan.

2.5. DFT Studies

The Vienna Ab-initio Simulation Package (VASP) was used to perform DFT based calculations with Grimme's D2 corrections.[30-34] The projector augmented wave (PAW) method was used and the cut-off energy for the expansion of the plane-wave basis set was set to 550 eV, which gave bulk energies converged to within 10E− 5 eV. A convergence criterion of 0.01 eV/Å for our structural optimizations was adopted. For all the preliminary calculations, the most commonly used Perdew-Burke-Ernzerhof (PBE) version of the generalized gradient approximation (GGA) was used to carry out total energy calculations and perform geometry optimizations.[35] For the bulk calculations, the Brillouin zone was integrated using a Monkhorst-Pack (MP) grid of 11×11×11 k-points. Since it is known that the Pd(111) surface is the most stable surface among the low index surfaces, all our calculations were performed on Pd(111) surface.[36] The ideal Pd(111) surfaces were modelled by a 3 × 3 supercell with 5 atomic layers. A lattice constant of 3.904 Å and a k-point grid of 3×3×1 was used. During the optimization process, the upper two atomic layers along with the furfural molecule were relaxed. Bottom three atomic layers were fixed to mimic the bulk of the system. The adsorption energy was calculated using the equation:

$$E_{ad} = E_{Pd(111)+Furfural} - (E_{Pd(111)} + E_{furfural})$$

Where, E_{ad} is the adsorption energy, $E_{Pd(111)+furfural}$ is the energy of the system with furfural molecule adsorbed and $E_{furfural}$ is the energy of the furfural molecule.

All DFT studies in this chapter were performed by Dr. Arun Chutia and Dr. Adam Thetford.

3. Results and Discussion

3.1. UV-Vis Spectroscopy

The reduction process to generate colloidal Pd was followed using UV-Vis spectroscopy. No surface plasmon resonance band is observed for Pd nanoparticles, unlike with Au, and so UV-Vis spectroscopy was only used to ensure the total reduction of the metal precursor during colloidal reduction. The UV-Vis spectrum of the metal salt precursor solution of K_2PdCl_4 is shown in figure 1, with featured peaks at λ_{max} = 210 and 238 nm, indicative of ligand to metal charge transfer in $[PdCl_4]^{2-}$.[37] After 30 minutes of stirring with $NaBH_4$, PVA-stabilised Pd nanoparticles are formed, and the total reduction of the Pd metal precursor is confirmed by the disappearance of the peaks, as illustrated in figure 1.

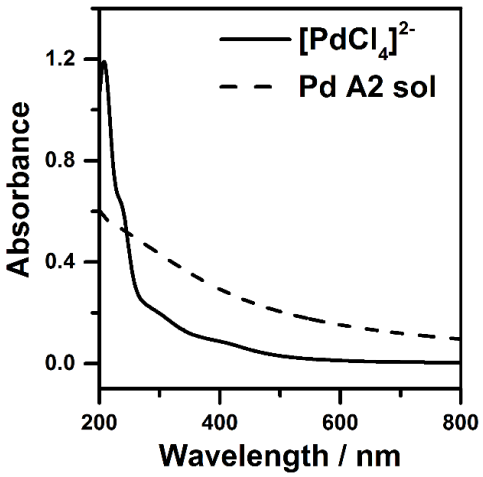

Figure 1. UV-Vis spectra of the K_2PdCl_4 precursor and the subsequent Pd sol generated after reduction of the salt by $NaBH_4$ in the presence of PVA (prepared in a H_2O solvent at 25°C, PdA2).

3.2. MP-AES

After immobilisation of Pd metal on to the support, PdA1, PdA2, PdB1 and PdB2 catalysts were examined in MP-AES to assess the Pd metal loading. Table 2 details the Pd concentration (ppm) of each sample, with this being obtained at two different wavelengths, characteristic to Pd emission (340.5 and 361.0 nm). These concentrations were subsequently converted to give an average Pd weight loading on TiO_2.

Table 2. MP-AES results of the sol-immobilised prepared 1 wt. % Pd/TiO_2 catalysts.

	Concentrations (ppm) at different Pd wavelengths (nm) 1st repetition		Concentrations (ppm) at different Pd wavelengths (nm) 2nd repetition		Average Pd wt. %
	Pd 340.5	**Pd 361.0**	**Pd 340.5**	**Pd 361.0**	
PdA1	7.29	7.42	6.99	7.00	0.72
PdA2	7.39	7.39	7.16	7.12	0.72
PdB1	6.65	6.63	6.69	6.79	0.67
PdB2	8.72	8.80	8.85	8.87	0.88

It is evident that for the Pd catalysts, with the exception of PdB2, there is ~ 70 % of the theoretical Pd loading deposited on to the support. Identifying the whereabouts of ~ 30 % Pd metal is challenging, with the most likely reason being incomplete immobilisation of Pd on to the support. Particularly for the preparation of PdA1 and PdB1, it is apparent the low temperature affects the viscosity of the solvent, and subsequent stirring ability during the immobilisation process. Vicious stirring for a prolonged time period is required to complete immobilisation of Pd nanoparticles on to the TiO_2 support, and for these two environments, more time is required.

3.3. TEM

TEM was used to obtain Pd particle size distribution histograms of all the Pd/TiO_2 catalysts, with selected images and respective histograms illustrated in figures 3 and 4. Within each solvent environment, decreasing the temperature of preparation decreases the average Pd particle diameter, in agreement with the Au work presented in chapter 3. PdA1 (1°C in H_2O = 2.5 nm) and PdB1 (−30°C H_2O:EtOH = 1.4 nm) produced the smallest Pd nanoparticles within their respective solvent series, with PdB1 exhibiting the narrowest particle size distribution of all the catalysts. Obtaining a Pd average particle diameter of 1.4 nm is significant, as it is understood to be the smallest generated, using a sol-immobilisation method involving PVA stabilized particles. The effect of solvent system can be assessed by comparing samples PdA1 and PdB2, and PdA2 and PdB3, which denote samples prepared at 1°C and 25°C, respectively. Interestingly, the B series (H_2O:EtOH solvent) of Pd/TiO_2 produces a larger spread of Pd particle size as a function of preparation temperature, with catalyst PdB2 being evidently smaller than the A series (H_2O solvent) equivalent (PdA1). However, the distribution of sizes for the A series is much narrower, and the catalyst

prepared at 25°C (PdA2), has a smaller average particle diameter compared to the B series analogue (PdB3). These differences are rationalized by the competing influences during sol-immobilization; the rate of metal precursor reduction, solubility of PVA, and interaction of solvent with the metal salt and formed colloid.

At room temperature or below, colloidal Pd is very stable to agglomeration, but at higher temperatures agglomeration is apparent, in which large Pd particles are formed. This is observed in the TEM images obtained for PdA3 (H_2O, 50°C, figure 3C) and PdA4 (H_2O, 75°C, figure 3D), in which particle size analysis was performed over only 100 particles as a result of the high agglomeration.

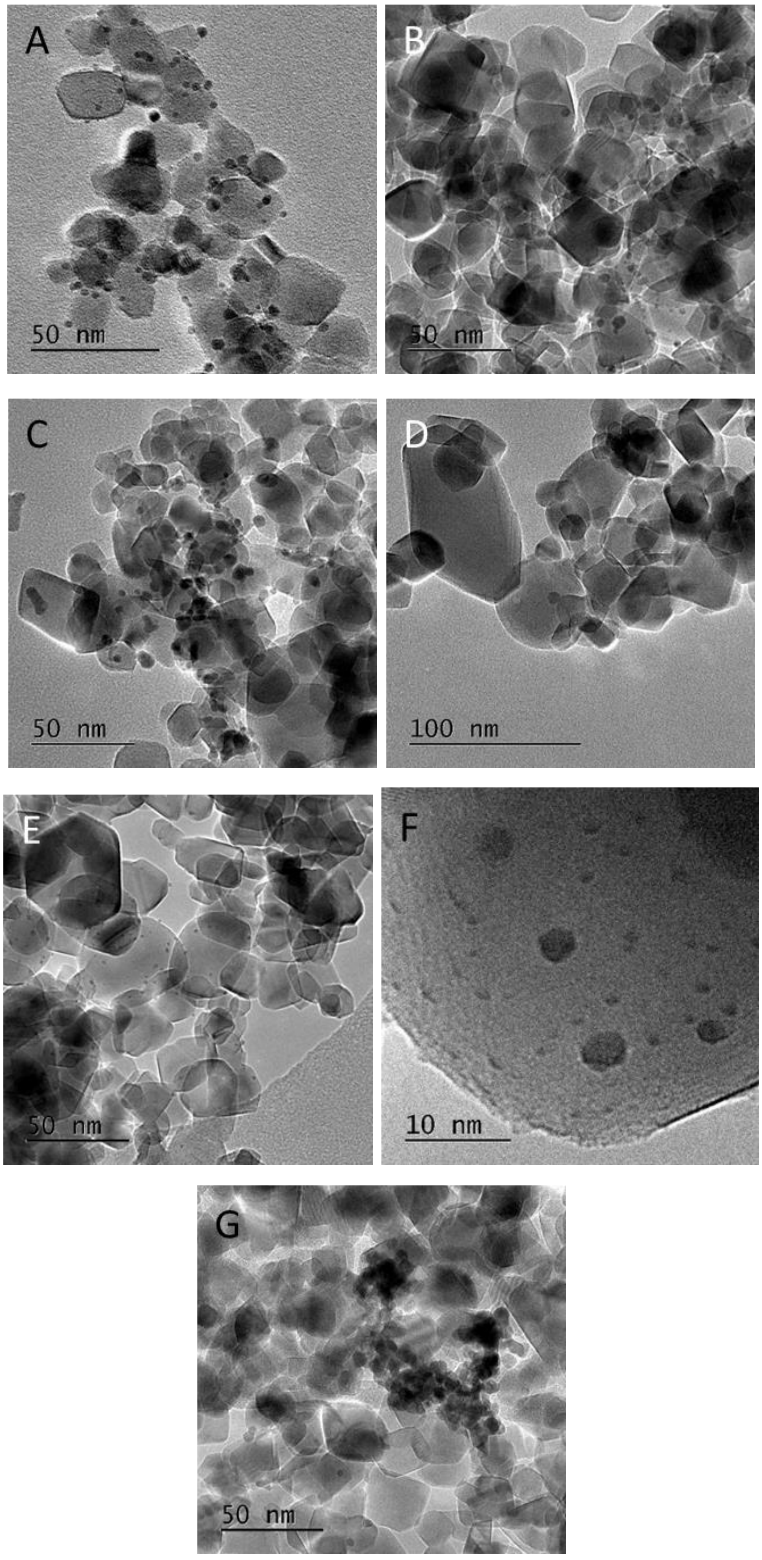

Figure 3. Selected TEM images of fresh 1 wt. % Pd/TiO_2 catalysts prepared at different temperatures, in varied solvent environments; A) 1°C H_2O PdA1, B) 25°C H_2O PdA2, C) 50°C H_2O PdA3, D) 75°C H_2O PdA4, E) −30°C H_2O:EtOH PdB1, F) 1°C H_2O:EtOH PdB2 and G) 30°C H_2O:EtOH PdB3.

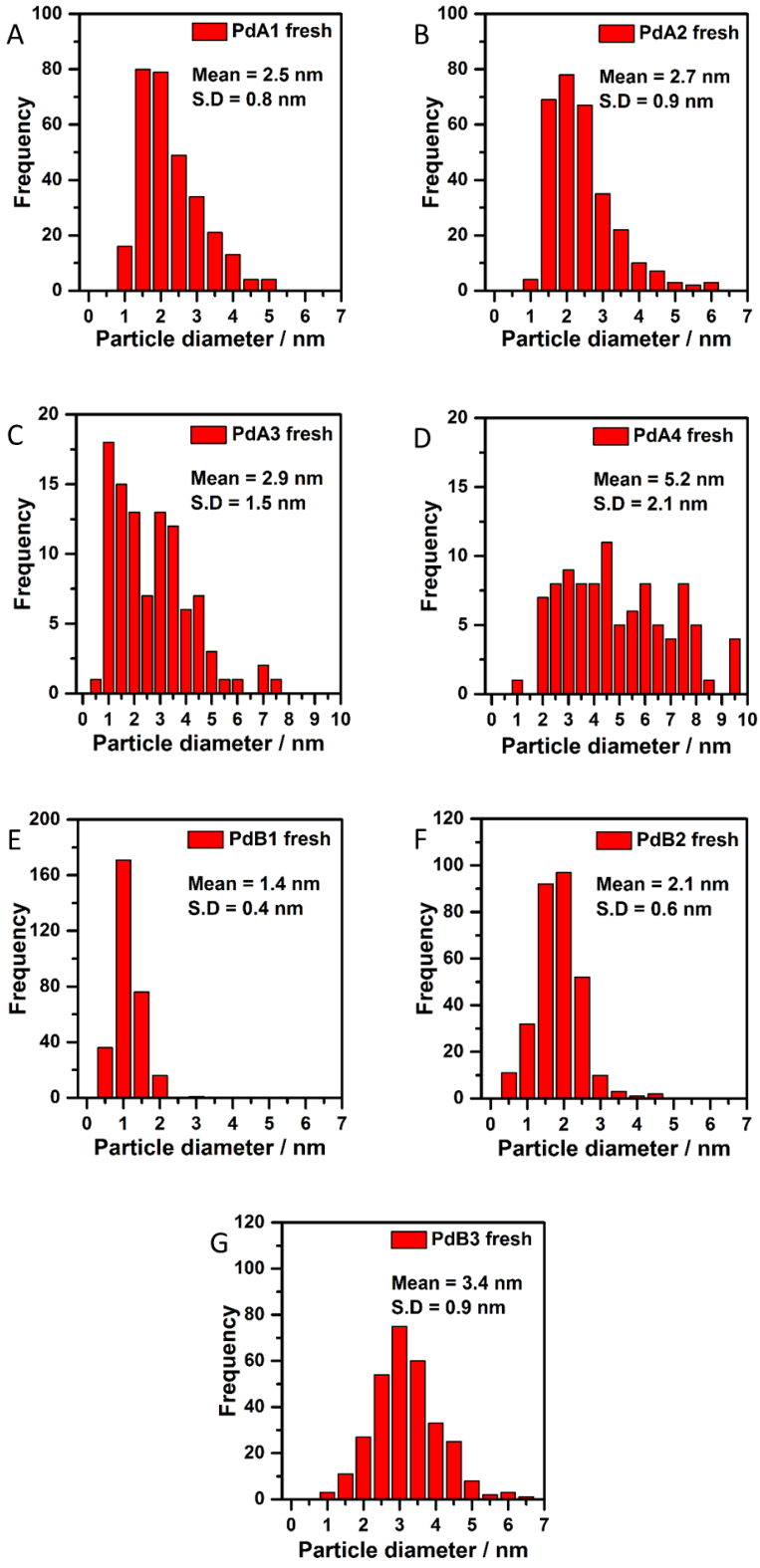

Figure 4. Particle size distribution histograms of fresh 1 wt. % Pd/TiO_2 catalysts prepared at different temperatures, in varied solvent environments; A) 1°C H_2O PdA1, B) 25°C H_2O PdA2, C) 50°C H_2O PdA3, D) 75°C H_2O PdA4, E) −30°C H_2O:EtOH PdB1, F) 1°C H_2O:EtOH PdB2 and G) 30°C H_2O:EtOH PdB3.

3.4. HAADF STEM

PdA1 and PdB1, the catalysts prepared at the lowest temperatures in their respective solvents, were examined with HAADF STEM to investigate the presence of Pd clusters too small to image in high resolution with standard TEM. The presence of ultra-small Pd clusters is clearly evident for both catalysts (figures 5A-D), with many Pd particles below 1 nm observed. The integrated HAADF STEM intensity analysis identifies clusters of Pd < 20 atoms for the PdA1 (1°C H_2O) catalyst (figure 5E).[38-39] The ability to achieve significant populations of metal clusters through standard chemical means remains a challenge, and in accordance with the Au work presented in chapter 3, it has demonstrated that adjusting the temperature of colloidal reduction is able to influence this. The low Z-contrast between Pd and Ti means the Pd nanoparticles are difficult to observe, particularly for clusters containing < 10 Pd atoms.

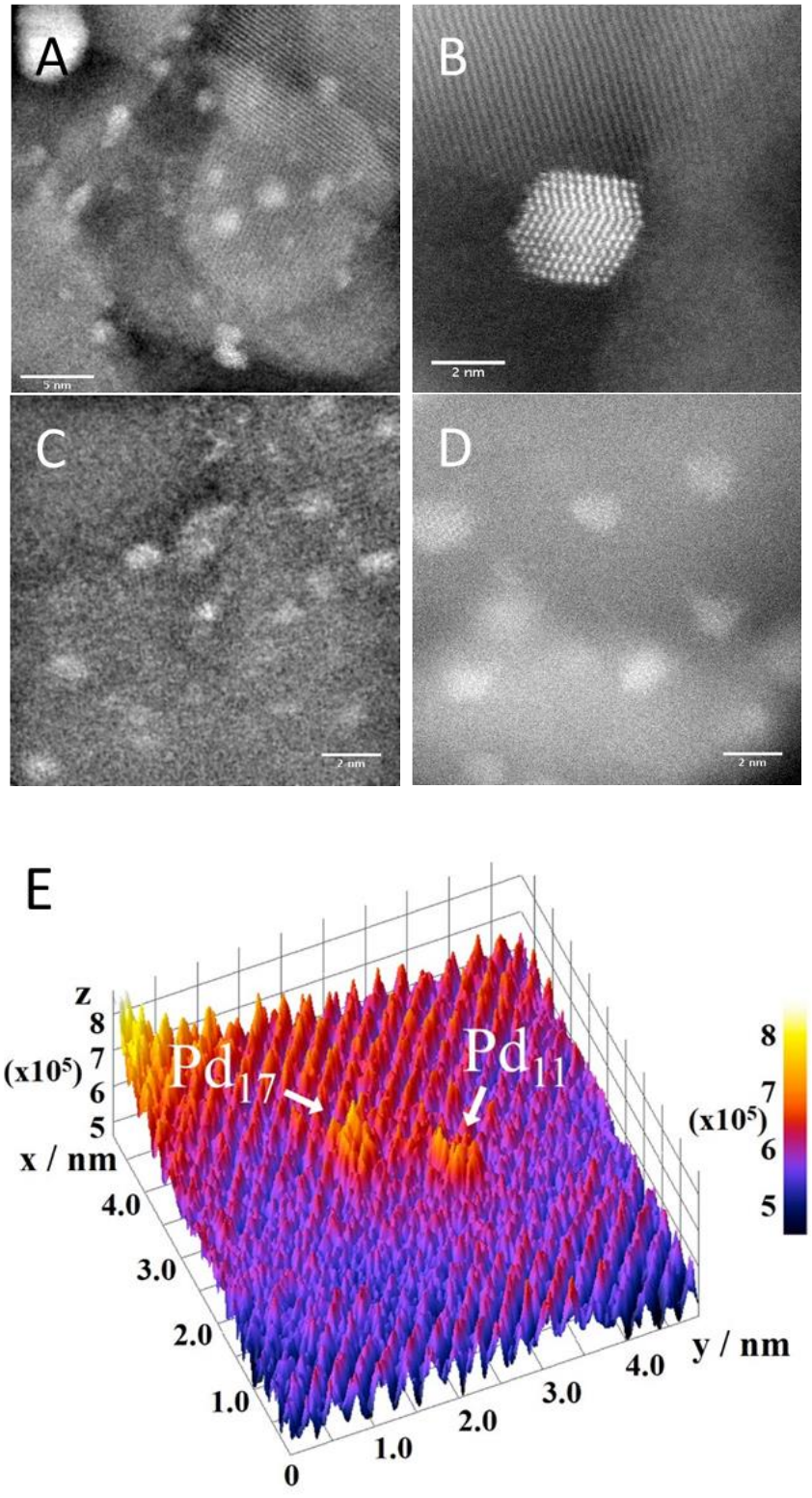

Figure 5. A and B) STEM dark field images of fresh 1 wt. % Pd/TiO_2 prepared at 1°C in H_2O (PdA1), C and D) STEM dark field images of fresh 1 wt. % Pd/TiO_2 prepared at −30°C in H_2O:EtOH (PdB1), and E) Processed HAADF STEM image of PdA1 showing Pd_{11} and Pd_{17} clusters.

3.5. XAFS

XANES is a valuable tool in probing the speciation of metal nanoparticles, in this instance for determining the Pd oxidation state in the Pd/TiO_2 catalysts. The ratio between Pd^{2+} and Pd^0 was performed by linear combination analysis (LCA) of the 1st derivative of the XANES profile, using PdO and Pd foil as reference standards (figure 6 and table 3). It is evident that for each solvent system, lowering the temperature at which colloidal Pd is prepared results in an increase in Pd^{2+}. All XAFS measurements represent the whole sample, meaning that for nanoparticle systems the surface speciation can influence the overall response only for very small nanoparticle size; the ratio of surface:core species increases as the average nanoparticle diameter decreases. Small Pd nanoparticles form an oxidic surface layer at room temperature when exposed to air,[40] and indeed, a clear correlation between average Pd particle diameter (by TEM) and the extent of Pd^{2+} is observed.

Table 3. Solvent and temperature conditions applied for each Pd/TiO_2 catalyst preparation, average Pd particle diameter calculated by TEM analysis and XANES linear combination analysis data for the fresh 1 wt. % Pd/TiO_2 catalysts.

Temperature (°C)	H_2O/EtOH solvent ratio (vol:vol)	Sample notation	TEM average Pd diameter (nm)	Reference standards (%)		
				Pd^{2+}	Pd^0	R_{factor}
1	100	PdA1	2.5 ± 0.8	33	67	0.043
25	100	PdA2	2.7 ± 0.9	29	71	0.037
50	100	PdA3	2.9 ± 1.5*	20	80	0.036
75	100	PdA4	5.2 ± 2.1*	12	88	0.025
−30	50	PdB1	1.4 ± 0.4	71	29	0.056
1	50	PdB2	2.1 ± 0.6	36	64	0.045
25	50	PdB3	3.4 ± 0.9	25	67	0.043

* As a consequence of dense agglomeration only 100 particles were counted.

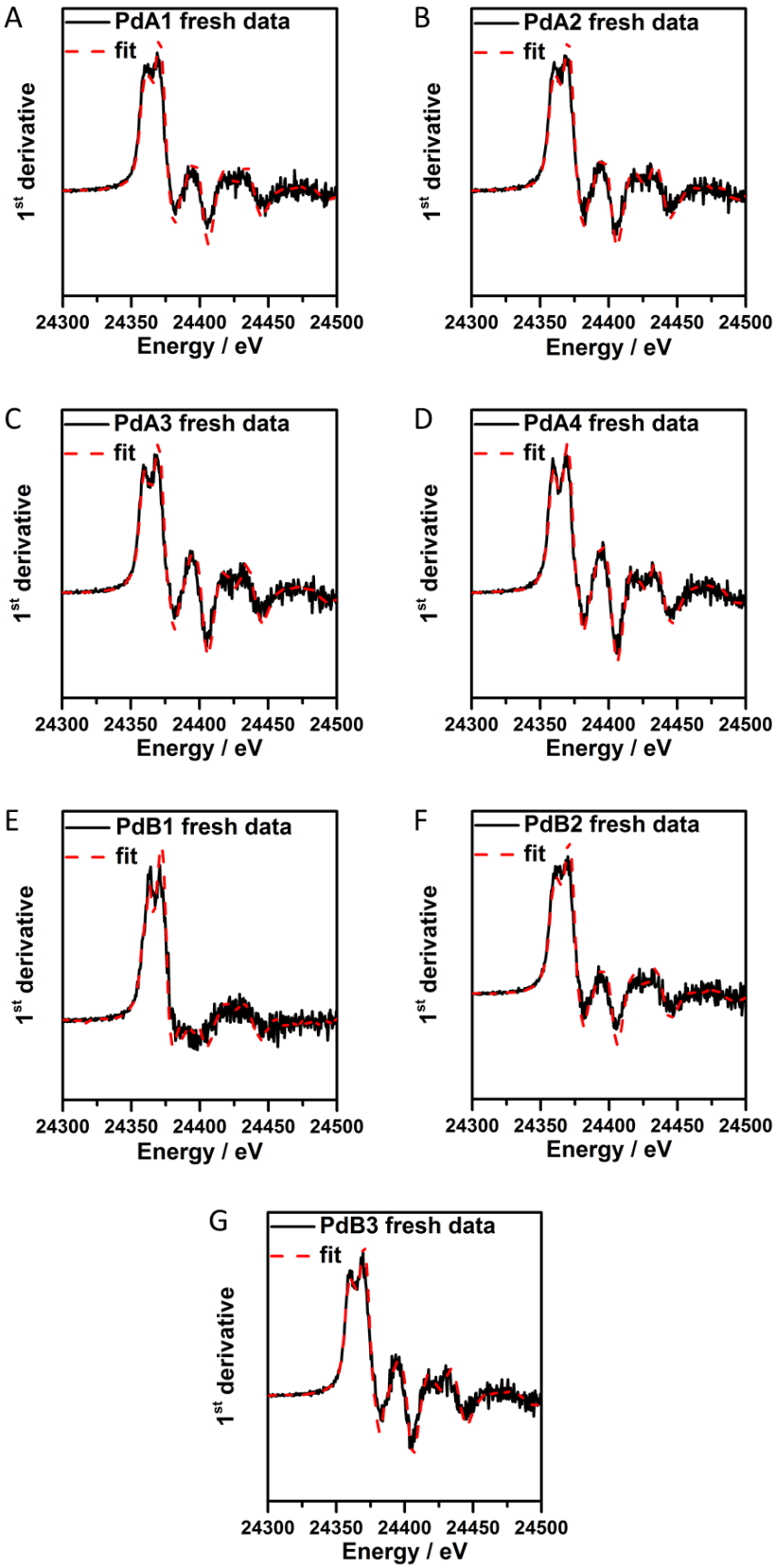

Figure 6. 1st derivative data and corresponding LCA fit for the Pd/TiO$_2$ catalysts (PdO and Pd foil used as reference materials).

EXAFS was used to investigate the local coordination of the Pd. The k^2-weighted forward Fourier transform of PdA1 (figure 7) confirms there are no large PdO crystallites. The Pd-Pd scattering path that would otherwise be present at 3Å, and can be observed in the PdO reference, is not observed in the PdA1 data. Combining this knowledge with that from the XANES analysis means that very small Pd nanoparticles exist, particularly for the PdB1 catalyst (−30°C H_2O:EtOH), in which the contribution is 71% Pd^{2+} and only 29% Pd^0. Using the ratio of Pd^{2+}:Pd^0 as an indication to Pd particle size (higher ratio = smaller Pd particles) means that the XAFS analysis is consistent with TEM analysis, confirming that preparing colloidal Pd nanoparticles at a lower temperature results in a decrease in particle size. Pd colloidal preparation at −30°C in a mixed H_2O:EtOH solvent shows the most significant interest as the stabilization of ultra-small metal nanoparticles is challenging, but achievable.

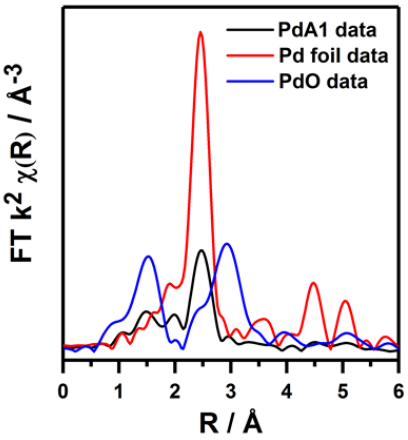

Figure 7. k^2 weighted forward Fourier transform data for PdA1 (1°C H_2O), Pd foil and PdO reference.

3.6. CO-adsorption – Transmission IR

The available surface sites of PdA1, PdA2, PdB1 and PdB2 were quantitatively evaluated using CO as a probe molecule (figure 8), in which the IR frequency of the CO band was used to assess differences in the surface structure of the Pd nanoparticles. Previous literature was used to assign the CO bands to distinguish Pd sites. The adsorption bands labelled (i) present at 2140 and 2120 cm^{-1}, are assigned to CO adsorbed linearly on Pd^{2+} and Pd^+, respectively. [41-42] The band at 2120 cm^{-1} is more prominent, with the band at 2140 cm^{-1} present as a small shoulder band in all cases. The CO bands labelled (ii) are positioned depending on the type of Pd metal site they

occupy; the band at 2086 cm^{-1} is assigned to CO linearly adsorbed on corner sites of Pd nanoparticles,[43] whereas the band at 2063 cm^{-1} can be ascribed to linear adsorption on Pd nanoparticle edges. The bands labelled (iii) present below 2000 cm^{-1} are a consequence of bridge-bonded CO, with the bands identified at ~1975 and 1945 cm^{-1} attributed to adsorption of facets and edges, respectively,[43] and the adsorption band at 1875 cm^{-1} ascribed to CO on threefold sites.[41-42] Spectra obtained for all four catalysts exhibit noticeable differences in the distribution of available sites. The relative intensities of the linearly adsorbed CO bands, compared to that from bridge-bonded CO, is much higher for the catalysts prepared in a mixed H_2O:EtOH solvent system. Furthermore, there are differences in the ratio between different types of linear and bridge-bonded sites. The series of nanoparticles prepared in the mixed H_2O:EtOH solvent have a greater proportion of the 2086 cm^{-1} linear adsorbed CO, and 1975 cm^{-1} bridge-bonded CO. It is clear that changing the solvent system of preparation affords Pd nanoparticles with different surface characteristics, must notably change the ratio of available low coordinated (corners/edges), and faceted Pd sites.

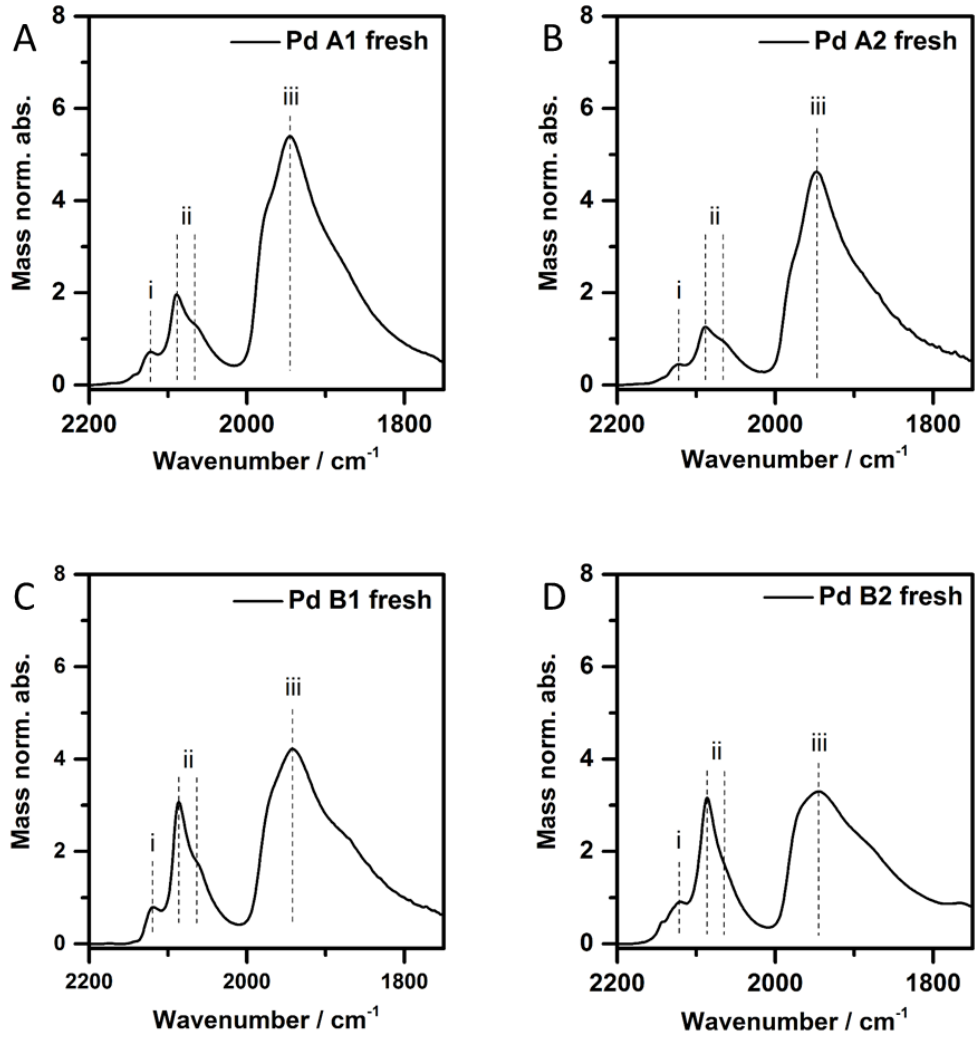

Figure 8. Pd mass normalised FTIR spectra from CO-adsorption studies on different 1 wt. % Pd/TiO_2 catalysts; A) 1°C H_2O PdA1, B) 25°C H_2O PdA2, C) −30°C H_2O:EtOH PdB1 and D) 1°C H_2O:EtOH PdB2.

3.7. Catalytic Studies – Furfural Hydrogenation

Both series of catalysts were evaluated for the hydrogenation of furfural (furfural = 0.3 M; furfural/metal molar ratio = 500, 5 bar H_2, solvent 2-propanol) at 25°C and 50°C, with the data illustrated graphically in figure 9 and presented in tables 4 and 5. Comparing the data between the A series (prepared in H_2O) and B series (prepared in H_2O:EtOH) some interesting relationships can be observed. For the A series there is clear correlation between Pd particle size and activity; smaller Pd nanoparticles are more active, regardless of the reaction temperature. Indeed, the catalyst of the A series of smallest Pd particle size (PdA1, 2.5 nm), showed the highest catalytic activity (440

and 620 mol (mol Pd)$^{-1}$ h^{-1}, at 25 and 50°C, respectively). For the A series at 50°C, other distinct trends can be seen; as the Pd particle size increases (PdA1 → PdA4), selectivity to furfuryl alcohol increases (48, 65, 76 and 78% for PdA1, PdA2, PdA3 and PdA4, respectively, table 5) with a decrease in selectivity to tetrahydrofurfuryl alcohol (39, 25, 20 and 15% for PdA1, PdA2, PdA3 and PdA4, respectively, table 5). On some occasions, the A series catalysts showed improved activity, compared to the B series at comparable particle sizes. PdA1, with mean particle size of 2.5 nm has a higher activity at 50 °C than PdB2 (620 and 470 converted mol (mol Pd)$^{-1}$ h^{-1}, respectively, table 5), despite the smaller particle size of PdB2 (2.1 nm). It must be noted that these Pd mass normalized activities are high when compared against current Pd based catalysts for this reaction.[15, 27] Biradar *et al*. reported a TOF of 183 hr^{-1} for furfural hydrogenation over Pd loaded on all silica MFI-type molecular sieve (Pd/MFI),[15] whereas Bhogeswarao *et al*. reported values up to 1372 hr^{-1} over Pd/Al_2O_3, however, much higher pressures were employed and TOFs were calculated per mole of exposed surface metal, not the total metal mass.[27] There are clearly other parameters, besides particle size, that influence activity and selectivity, as can be observed by the catalytic performance of the B series. In the case of the B series tested at 25°C, the catalyst, PdB1 (1.4 nm) was less active than PdB2 (2.1 nm) with activities of 491 and 568 mol (mol Pd)$^{-1}$ h^{-1}, respectively. The selectivity of B1 is comparable to that of the only previously reported Pd/TiO_2 catalyst (Pd particle also < 2 nm) used for this reaction, despite the different reaction solvent.[22] However, when tested at 50 °C, there was a direct relationship between particle size and activity. Another characteristic difference of the B series is the variation in selectivity profile with increasing particle size. Broadly speaking, there is an inverse relationship for furfuryl alcohol and tetrahydrofurfuryl alcohol selectivity with particle size compared to the A series; as the particle size increases furfuryl alcohol selectivity decreases and tetrahydrofurfuryl alcohol selectivity increases. It is apparent that there is a collaborative effect between the solvent system and temperature of colloidal preparation, which directs the catalytic performance. It is believed that the competing influences of sol immobilization – rate of reduction, PVA solubility, PVA/solvent/colloid interaction – are responsible for the trends observed. The difference in selectivity can be ascribed to the different binding modes of furfural on the Pd surfaces. The CO chemisorption studies for the A and B series show a clear difference in linear CO: bridged CO ratio, with the B series having

a far greater proportion of linear sites. Where CO binds linearly to Pd edge and corner sites, previous studies have indicated that these sites tend to bind furfural in a perpendicular orientation, rather than flat across a surface, in agreement with the recent work of Medlin *et al*.[29] In these instances improved selectivity to furfuryl alcohol is observed. Moreover, the adsorption sites that correspond to bridge-bonded or three-fold CO adsorption are able to bind furfural through both the aldehyde functionality and the furan ring and promote the complete reduction to tetrahydrofurfuryl alcohol.

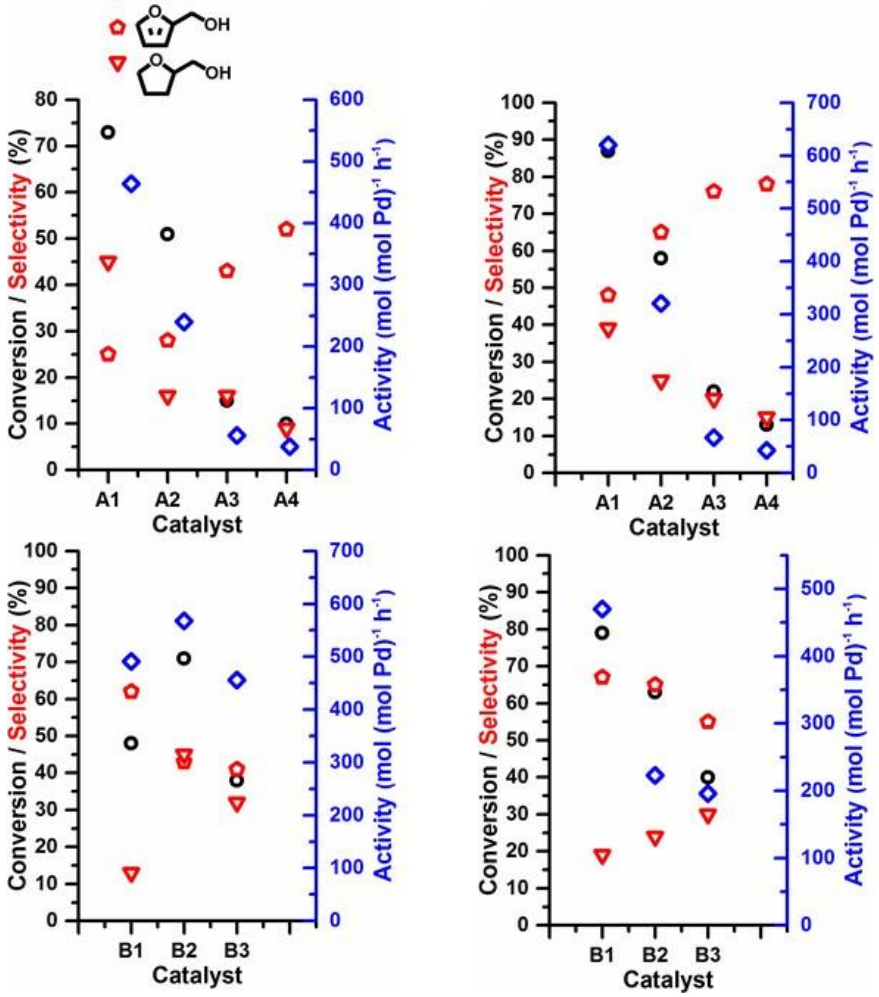

Figure 9. Catalytic performance plots for hydrogenation of furfural using tailored Pd/TiO_2 catalysts; (top left) Pd/TiO_2 A1→A4 tested at 25°C, (top right) Pd/TiO_2 A1→A4 tested at 50°C, (bottom left) Pd/TiO_2 B1→B3 tested at 25°C, and (bottom right) Pd/TiO_2 B1→B3 tested at 50°C. Reaction conditions: Furfural = 0.3 M; F/metal molar ratio = 500, 5 bar H_2, solvent 2-propranol, Converted mol $(mol\ Pd)^{-1}\ h^{-1}$ calculated after 15 min of reaction, selectivity calculated at 50% conversion, except catalysts PdA3 and PdA4 at 25°C, where selectivity is calculated at 10% conversion. Open black circles denote conversion. Open blue diamonds denote activity. Red shapes indicate selectivity to the products denoted by the inset key.

Table 4. Furfural hydrogenation activity and product selectivity of the different Pd/TiO$_2$ catalysts. Reaction performed at 25°C.

Catalyst[a]	Activity[b]	Conv. (%) after 5h	Selectivity (%)[c]						
			Furfuryl alcohol	Tetrahydro furfuryl alcohol	2-methyl furan	2-methyl tetrahydro furan	Furan	Ethers 1	Ethers 2
A1	464	73	25	45	-	-	-	15	12
A2	240	51	28	16	-	-	-	50	3
A3	56	15	43[d]	16[d]	-	-	-	40[d]	-
A4	38	10	52[d]	9[d]	-	-	-	38[d]	-
B1	491	48	62	13	-	-	-	14	1
B2	568	71	43	45	-	-	-	9	1
B3	456	38	41	32	-	-	-	26	-

[a] Reaction conditions: Furfural = 0.3 M; F/metal molar ratio = 500, 25°C, 5 bar H_2, solvent 2-propranol, [b] Converted mol (mol Pd)$^{-1}$ h^{-1} calculated after 15 min of reaction, [c] Selectivity calculated at 50% conversion, [d] Selectivity calculated at 10% conversion.

Table 5. Furfural hydrogenation activity and product selectivity of the different Pd/TiO$_2$ catalysts. Reaction performed at 50°C.

Catalyst[a]	Activity[b]	Conv. (%) after 3h	Selectivity (%)[c]						
			Furfuryl alcohol	Tetrahydro furfuryl alcohol	2-methyl furan	2-methyl tetrahydro furan	Furan	Ethers 1	Ethers 2
A1	620	87	48	39	-	-	-	5	-
A2	321	58	65	25	-	-	-	5	-
A3	67	22	76	20	-	-	-	3	-
A4	43	13	78	15	-	-	-	6	-
B1	470	79	67	19	-	-	-	13	-
B2	223	63	65	24	-	-	-	2	-
B3	196	40	55	30	-	-	-	2	-

[a] Reaction conditions: Furfural = 0.3 M; F/metal molar ratio = 500, 50°C, 5 bar H_2, solvent 2-propranol, [b] Converted mol (mol Pd)$^{-1}$ h^{-1} calculated after 15 min of reaction. [c] Selectivity calculated at 50% conversion, [d] Selectivity calculated at 10% conversion.

Catalysts used for sustainable technologies need to be robust and durable, so recycling studies were performed. The recycling tests were performed on A1 and B1 catalysts at different temperatures (figure 10), by reusing the same catalyst without any pretreatment. These data evidenced a significant deactivation of both catalysts when the reaction was performed at 25°C, whereas at 50°C the deactivation was less pronounced. Assessing the reaction profile (figure 11) as a function of time, evidences that stronger deactivation phenomena occur for all the catalysts when the reaction was

performed at 25°C. To explain the origin of the deactivation the used catalysts were also characterized.

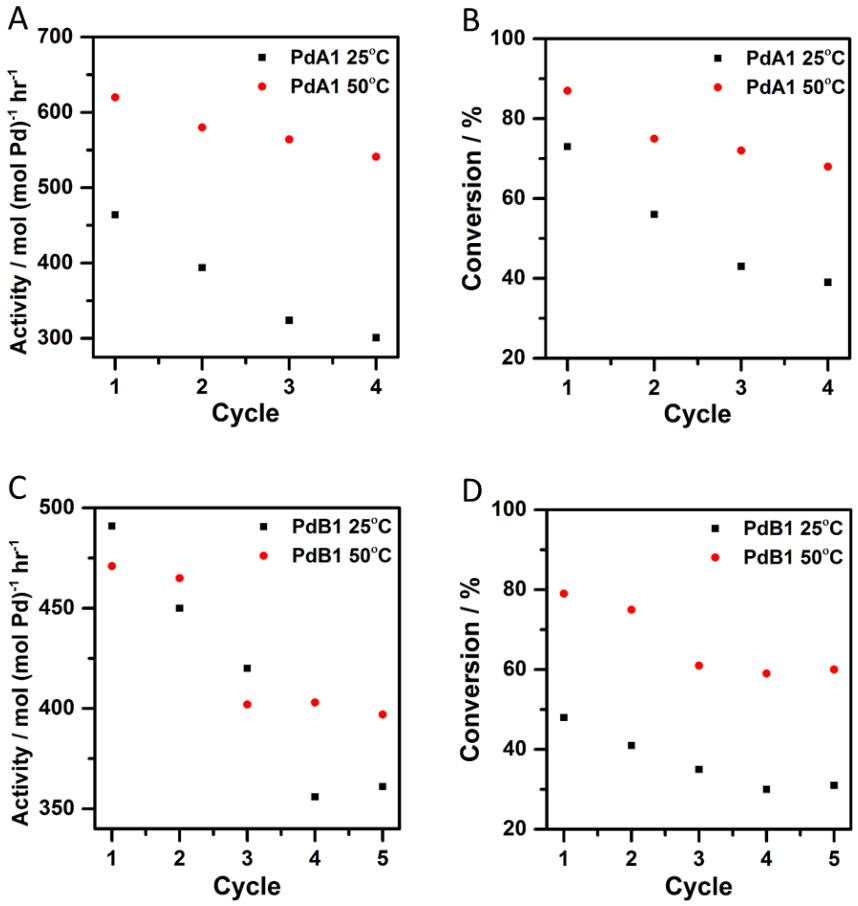

Figure 10. Furfural hydrogenation recycling studies performed at 25 and 50°C; A and B) PdA1, C and D) PdB1. Reaction conditions: Furfural = 0.3 M; Furfural/metal molar ratio = 500, 5 bar H_2, solvent 2-propranol.

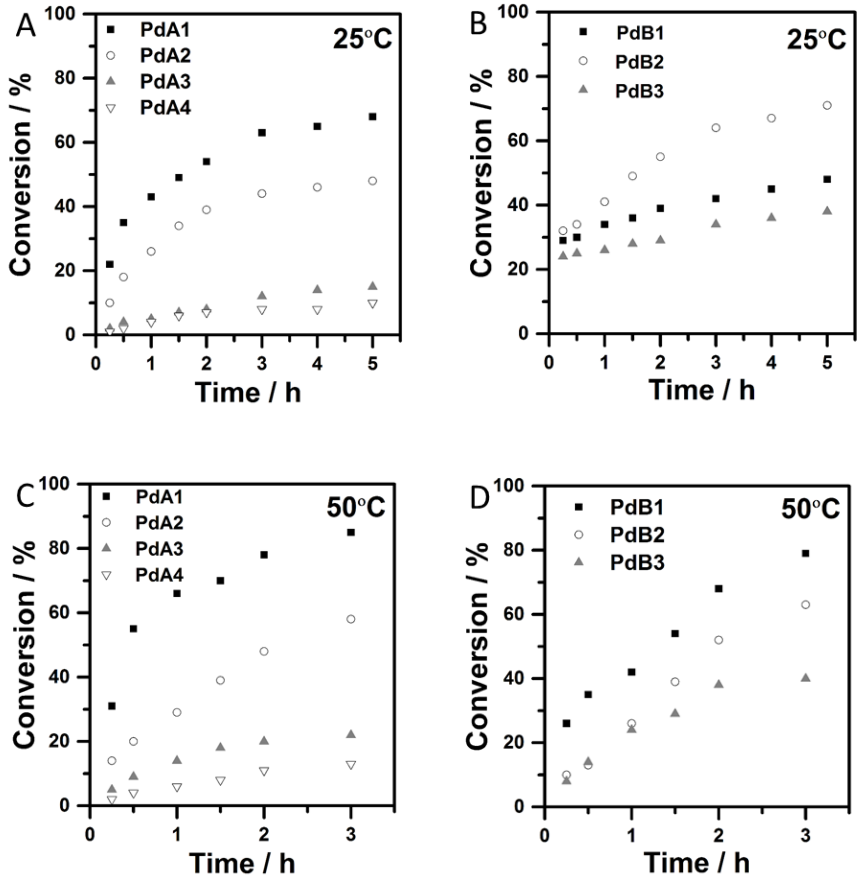

Figure 11. Time online furfural hydrogenation conversion profiles using Pd/TiO_2 catalysts. Reaction performed at 25°C. Time online furfural hydrogenation conversion profiles using Pd/TiO_2 catalysts. Reaction performed at 50°C. Reaction conditions: Furfural = 0.3 M; F/metal molar ratio = 500, 5 bar H_2, solvent 2-propranol.

3.8. Used Catalyst Characterisation

3.8.1. TEM and STEM HAADF

TEM was used to calculate the average Pd particle size after the recycling experiments were performed at both 25 and 50°C, with selected TEM images shown in figure 12. The particle size distributions (figure 13) indicate that for the samples prepared in water, there is a small increase in average size (2.5 to 2.7 nm for PdA1) when performed at 25°C, with no further particle growth when performed at the higher temperature. However, for the Pd catalysts prepared in H_2O:EtOH mixture, the temperature of reaction has a larger influence for PdB1, in which the average particle size increases from 1.4, to 2.0 nm and 2.7 nm when the reaction was performed at 25 and 50°C, respectively and these results are in agreement with the observed initial

decrease in catalytic activity. The average Pd particle diameter is still very small and STEM was used to identify the presence of Pd clusters in the PdA1 and PdB1 catalysts after performing the reaction at 25°C (figure 14). It is clear that very small Pd clusters are preserved during catalysis, a result of the mild reaction conditions and protective stabilization of PVA.

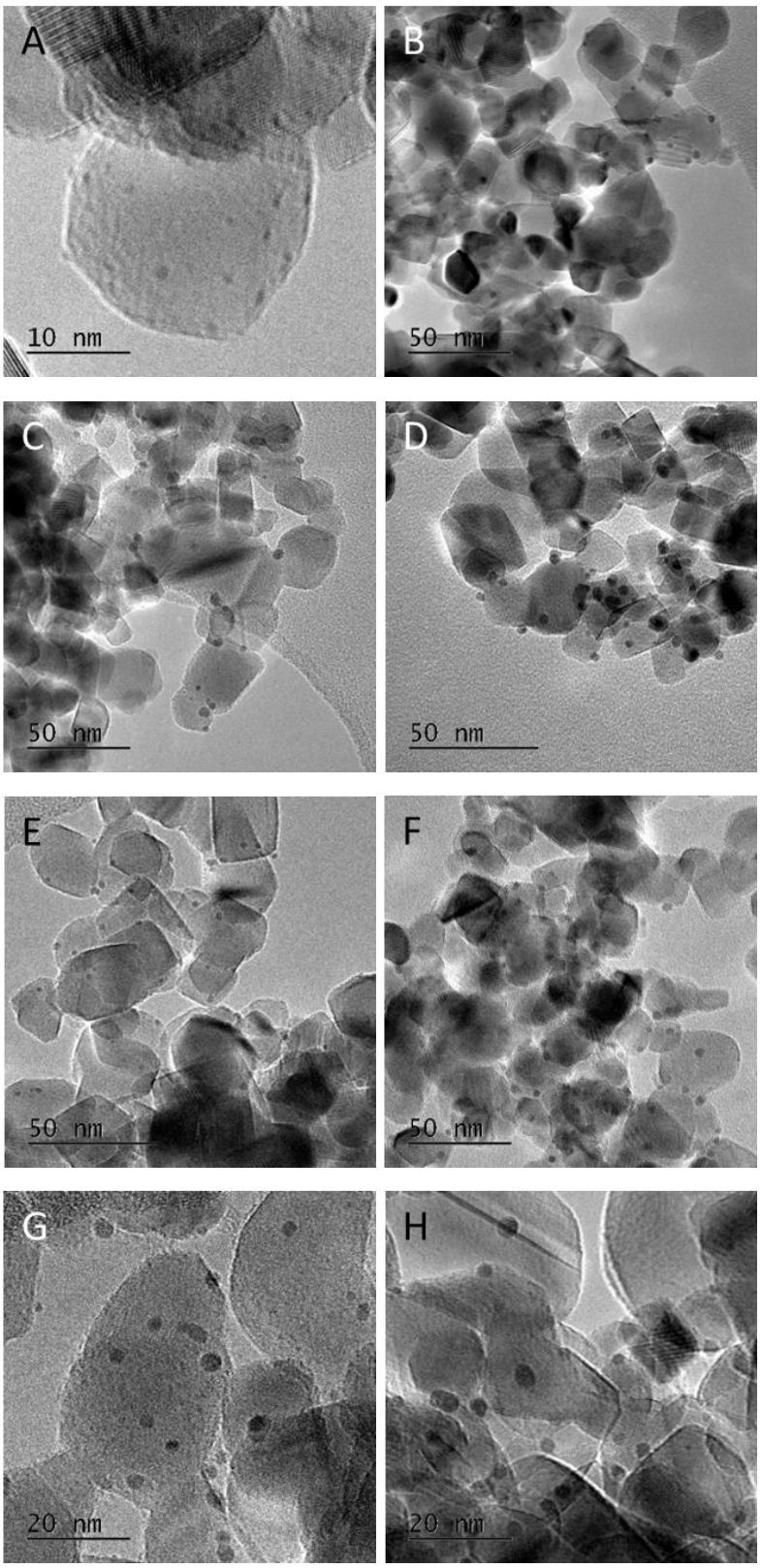

Figure 12. Selected TEM images of 1 wt. % Pd/TiO_2 catalysts used in the hydrogenation of furfural, performed at different temperatures: A) PdA1 25°C, B) PdA1 50°C, C) PdA2 25°C, D) PdA2 50°C, E) PdB1 25°C, F) PdB1 50°C, G) PdB2 25°C and H) PdB2 50°C.

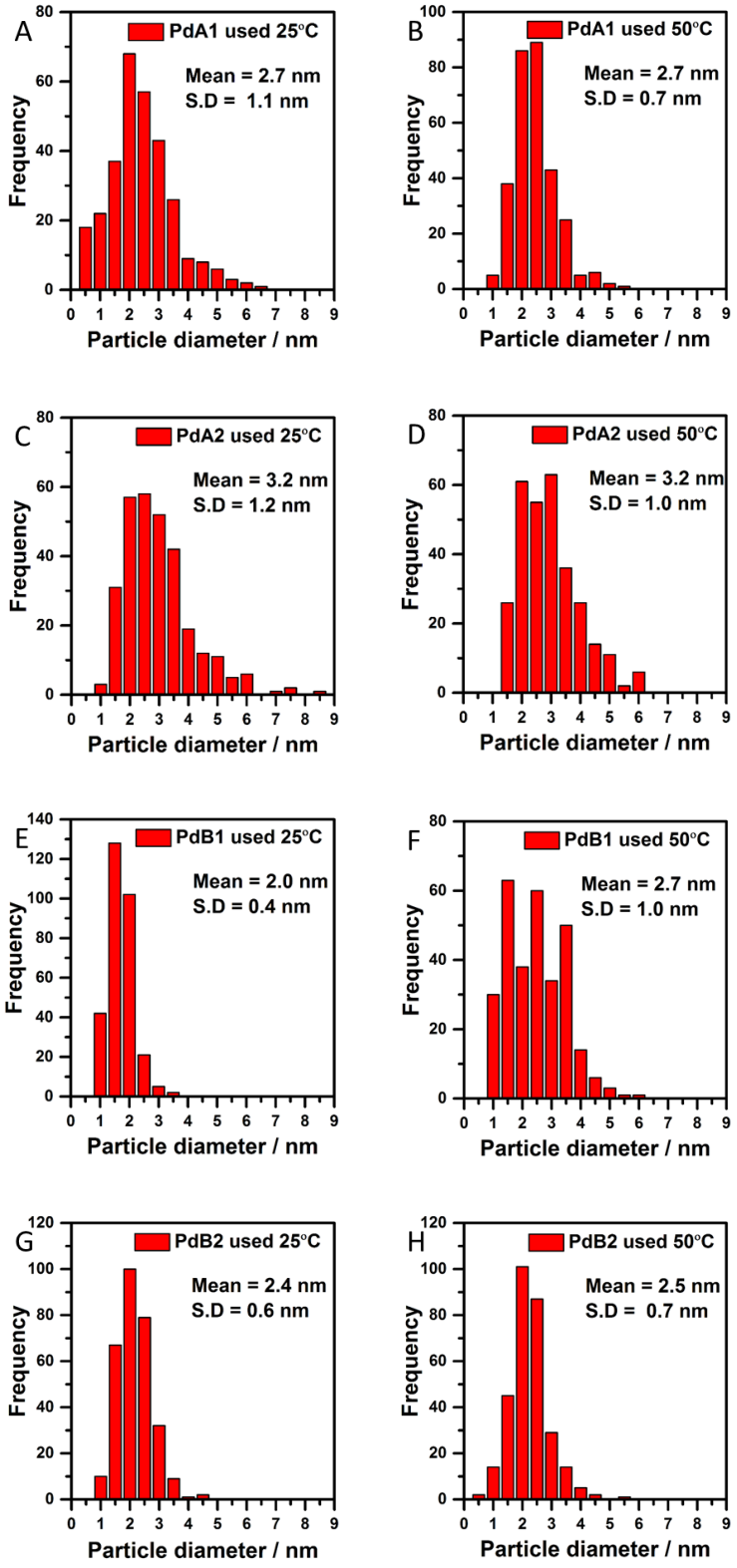

Figure 13. Particle size distribution histograms of 1 wt. % Pd/TiO_2 catalysts used in the hydrogenation of furfural, performed at different temperatures: A) PdA1 25°C, B) PdA1 50°C, C) PdA2 25°C, D) PdA2 50°C, E) PdB1 25°C, F) PdB1 50°C, G) PdB2 25°C and H) PdB2 50°C.

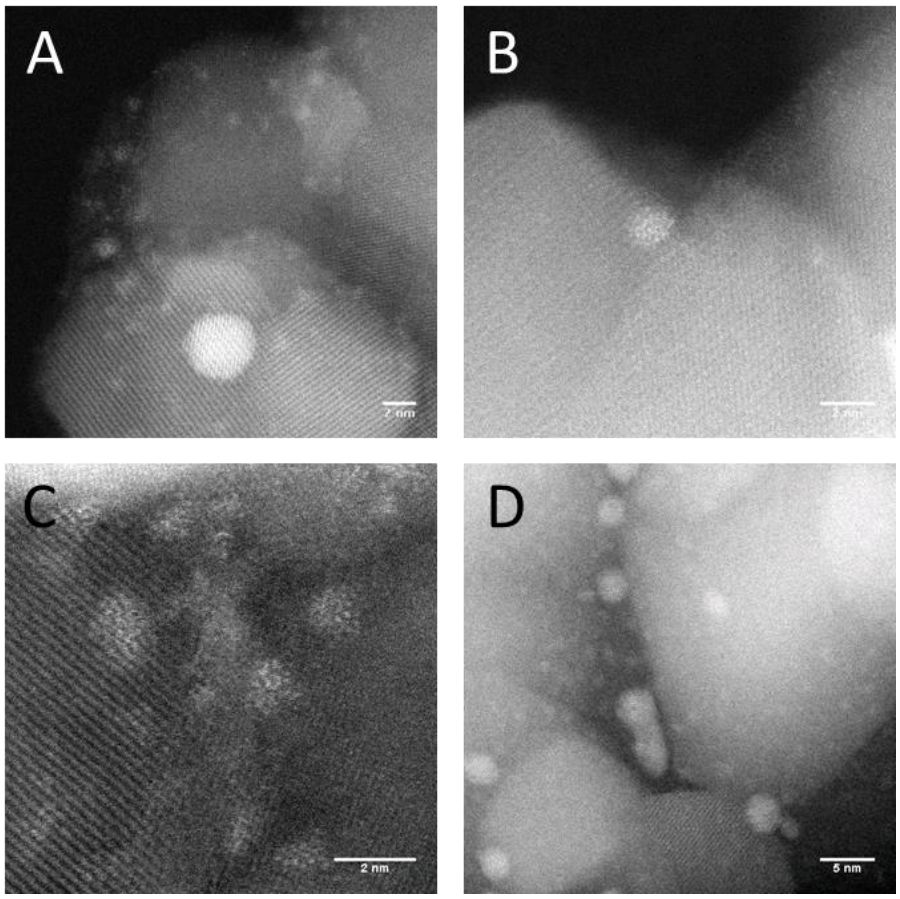

Figure 14. STEM HAADF images of the recycled Pd catalysts from furfural hydrogenation at 25°C; A) PdA1, B) PdA2, C) PdB1 and D) PdB2.

3.8.2. XAFS

The used PdA1 and PdB1 catalysts tested at 25°C (after 5 reaction cycles) were again assessed using XAFS spectroscopy, with the XANES data shown in figure 15A. The initial observation from the XANES is the presence of Pd^{2+} and Pd^{0}. The height of the main edge of the fresh and used catalysts are greater than that of Pd foil. This difference in height can be attributed to the presence of oxidized Pd in the Pd/TiO_2 catalysts. Elsewhere, the maximum of the second XANES peak is seen to move to lower energy for the used catalysts, compared to the Pd foil. The shift in the position of the second maximum is observed for both hydride and carbide forms of Pd, however, the broadening of the first peak is only observed for carbidic Pd.[44-45] In this instance changes in the first peak maximum are complicated by the separate contribution of oxidized forms of Pd. Further evidence of carbide formation was sought by assessing the EXAFS (figure 15B and table 6), which is able to probe changes in Pd-Pd spacing. Analysis of the EXAFS data confirms an increase of Pd-Pd spacing after reaction from

~2.74 Å to 2.77 Å. An increase in Pd-Pd spacing is encountered for the formation of Pd carbide and hydride,[40, 46] however, hydride is known to readily desorb from the Pd lattice under normal atmospheric conditions. Considering this, it is apparent that this expansion could not be caused by the formation of hydride. The expansion of the Pd lattice from 2.74 Å to 2.79 Å has been previously reported for bulk (PdC_x, where x = 0.13) Pd carbide formation, suggesting that only partial carbidization ($PdC_{0.8}$ based on Pd-Pd expansion) has occurred for these catalysts, and which could be better described as interstitial carbon near at the nanoparticle surface or subsurface.[46] It is proposed that the deactivation encountered during the lower temperature hydrogenation reaction is a result of the transformation to Pd carbide, expansion of the Pd-Pd distance, and the subsequent effect on hydrogen dissociation and the η^2 adsorption of C=O and C=C functionalities. Indeed, a greater degree of deactivation is observed for catalysts PdA1 (464 → 394 mol (mol Pd)$^{-1}$ h^{-1}) compared to PdB1 (491 → 450 mol (mol Pd)$^{-1}$ h^{-1}), which correlates with the extent of interstitial carbon observed. The mechanism for interstitial carbon formation is not clear, but it is possible that hydrocarbonaceous deposits (substrate adsorption) on the Pd surface influences the catalyst performance. Interestingly, there are reports that consider the effect of carbon, more specifically surface, subsurface and hydrocarbonaceous deposits on the hydrogenation performance in Pd catalyst. Setiawan *et al.* monitored the time online deactivation of Pd catalysts through the formation of carbidic species at temperatures considered to be low (180°C), albeit much higher temperatures than that for the present study (25-50°C).[47] Schlogl *et al.* reported the selectivity in the hydrogenation product distribution is related to the extent of carbon retention and also the different crystal facets of Pd; for facets in which carbon dissolution is not favorable, it is possible for bulk hydrogen to emerge to the surface. However, the high activity of this species means there is lower product selectivity.[48]

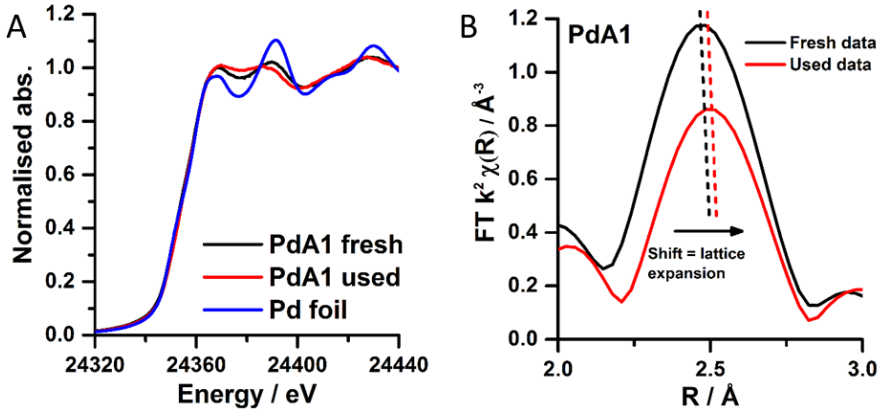

Figure 15. A) Normalized XANES spectra of PdA1 and PdB1 after catalysis and a Pd^0 reference, B) Fourier transform χ^2 weighted EXAFS data of PdA1; fresh (black line) and used (red line).

Table 6. 1st shell EXAFS fitting parameters derived from the k^2 weighted Fourier transform for the Pd K edge EXAFS data for PdA1 and PdB1.

Sample	Abs Sc	N	R / Å	$2\sigma^2$ / Å^2	E_f / eV	R_{factor}
Fresh PdA1	Pd–O	1.2 (2)	1.970 (8)	0.004 (2)	6	0.005
	Pd–Pd	5.8 (4)	2.744 (2)	0.008 (0)		
Used PdA1 25°C	Pd–O	2.1 (4)	1.977 (8)	0.006 (3)	6	0.015
	Pd–Pd	4.0 (5)	2.772 (4)	0.008 (0)		
Fresh PdB1	Pd–O	3.0 (3)	1.997 (5)	0.004 (1)	4	0.02
	Pd–Pd	1.7 (6)	2.746 (11)	0.008(3)		
Used PdB1 25°C	Pd–O	1.5 (4)	1.971 (11)	0.007 (4)	0	0.008
	Pd–Pd	5.7 (4)	2.762 (3)	0.008 (1)		

3.8.3. DFT Calculations

To assess the effect of carbidization on the adsorption of furfural, DFT calculations were performed. Two different configurations of furfural, parallel and perpendicular, on a pristine Pd(111) surface, (figures 16a and b) were considered. The calculated adsorption energy for the parallel configuration ($Pd_{parallel}$) is -2.160 eV. In the case of the perpendicular configuration, the stability of the system on top of a Pd atom (Pd_{top}), on the bridge site between two Pd atoms (Pd_{bridge}) and on the three-fold hollow site

(Pd_{hollow}) was assessed. The adsorption energies for Pd_{top}, Pd_{bridge}, and Pd_{hollow} configurations are -0.632 eV, -0.940 eV and -2.185 eV, respectively, with relaxed structures of Pd_{top} and Pd_{bridge} retaining a perpendicular orientation. However, it is interesting to note that for the Pd_{hollow} site the furfural molecule attained a parallel configuration to the surface after relaxation ($Pd_{hollow\text{-}parallel}$), and is comparable in energy to the $Pd_{parallel}$ configuration. The adsorption energies obtained confirm that the parallel configuration of furfural binding is more stable than the perpendicular orientation.

Subsequently, the increase in Pd–Pd bond distances, as a result of carbidization, in bulk Pd (by 0.095Å) and sub-surface of Pd(111) (by 0.057Å) (figures 17 and 18, respectively), which were consistent with experimentally determined values of partially carbidized Pd nanoparticles was investigated.[44-45] It was found that the increase in Pd-Pd distance correlated with an increased adsorption energy for furfural. The calculated adsorption energy for this system is -1.613 eV, confirming that adsorption of furfural is more favourable on a pristine Pd(111), compared to a PdC(111).

To assess this change in stability the atom projected partial density of states (*ap*PDOS) of the C and O atoms of furfural molecule and Pd atoms of the Pd(111) and PdC(111) surfaces closest to each other was analyazed. For convenience, the Fermi energy (E_F) is shifted to 0, which is represented by a dotted line in figures 16c and d). From the analysis of *ap*PDOS we see that around -7.0 eV to -5.5 eV (figures 16c and d) there is a strong interaction between the *p*-orbitals, of C and O atoms of furfural, with the *d*-orbital signatures of Pd atoms on Pd(111) surface. However, on incorporating an interstitial C-atom, another sharp signature due to C *p* orbital appears around this region, which has a higher contribution than the *p*-orbital signatures due to C and O atoms of the furfural molecule. The interaction of the C *p*-signatures, due to interstitial C-atoms, interact more strongly with the nearby Pd atoms and result in a weakening of the interaction of furfural C and O atoms with the Pd(111) surface. As a consequence, adsorption of furfural is more favoured on pristine Pd(111), as compared to PdC(111).

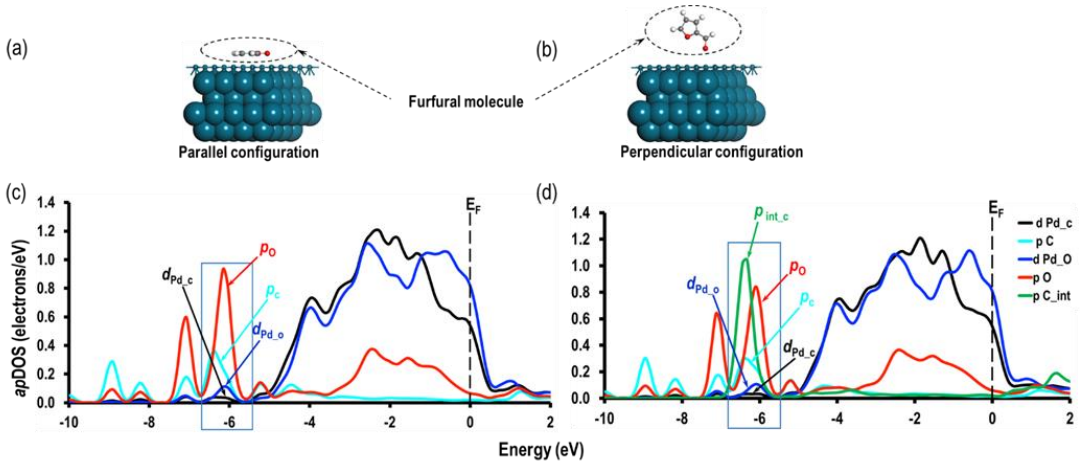

Figure 16. (a) Parallel, (b) Perpendicular configurations of furfural on Pd(111) surface, (c) *ap*DOS for pristine Pd(111) and (d) *ap*DOS for furfural on PdC(111) surface. Black and blue lines represent the signatures for Pd d orbitals close to C and O atoms respectively. Red, aqua and green lines represent the p-orbitals due to C, O and interstitial C atoms respectively.

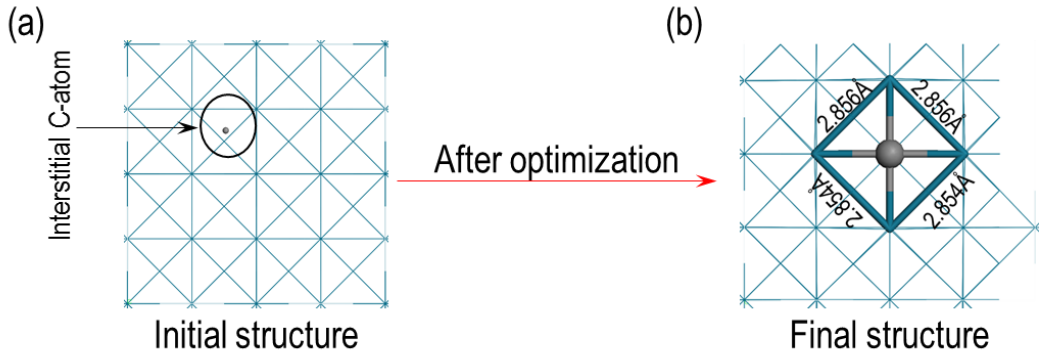

Figure 17. (a) Initial and (b) final structure of Pd bulk with an interstitial C-atom. After structural relaxation C forms bonds with the nearby Pd atoms. The average distance of Pd around C atom is 2.855 Å. So the difference between the Pd-Pd distance in bulk Pd with and without C atom is 0.095 Å (= 2.855 Å − 2.760 Å).

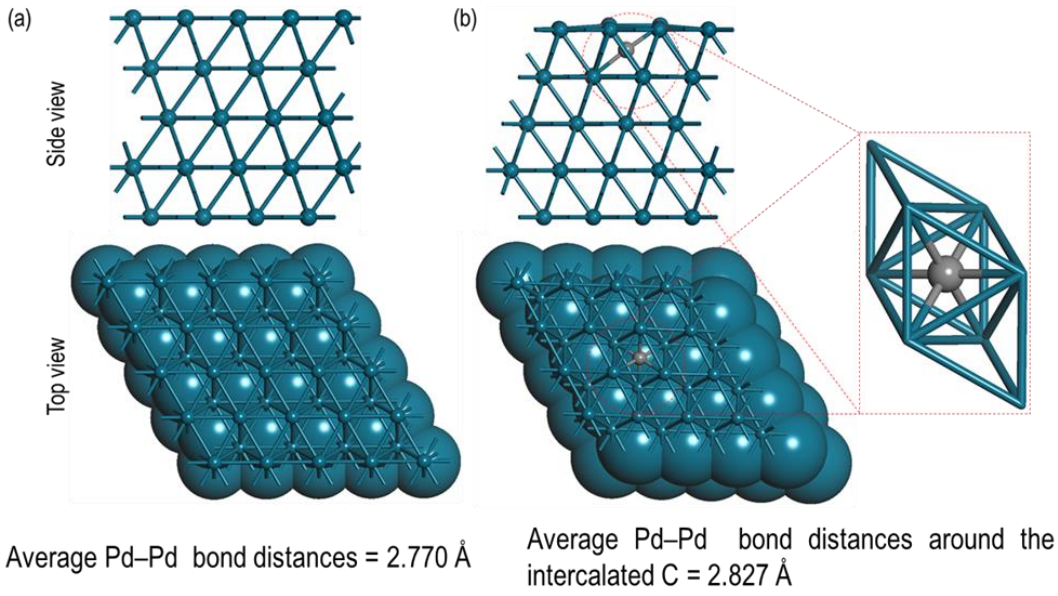

Figure 18. (a) Initial and (b) final structure of Pd(111) surface with an interstitial C-atom. After structural relaxation C forms bonds with the nearby Pd atoms. The difference between the Pd-Pd distance with and without interstitial C-atom is 0.057 Å (= 2.826833 Å − 2.769857 Å).

4. Summary and Conclusions

The optimization of colloidal preparation of nanoparticles, through adapting both the solvent of preparation and temperature of reduction, has again been demonstrated. These parameters allow the tuning of both, the size domains of Pd nanoparticles and available reaction sites, which directs the performance towards the hydrogenation of furfural. Reduced Pd nanoparticle size was achieved by lowering the temperature of colloidal reduction; for the catalyst prepared at 1°C in water, the average particle size was found to be 2.5 nm; however, clusters of Pd <20 atoms were also detected. Site selective catalysis was enabled by adjusting the solvent of colloid preparation; the Pd/TiO_2 catalysts prepared using a mixed H_2O:EtOH solvent were found to have a larger proportion of available corner and edge sites, which were able to direct the selectivity of the furfural hydrogenation products. The greater number of available corner and edge sites adsorb furfural perpendicular to the nanoparticle surface, resulting in greater selectivity to form furfuryl alcohol over the complete reduction product, tetrahydrofurfuryl alcohol. Also, the selectivity profile does not correspond solely to particle size; for the B series furfuryl alcohol selectivity decreases with increasing particle size, whereas for the A series the inverse relationship is found. The available sites are therefore not just a result of particle size, but also a consequence of the interaction of the protecting agent with the nanoparticles prepared. This influence was also manifested in recycling studies, where those catalysts prepared in mixed H_2O:EtOH solvent, were more robust than those prepared solely in H_2O. By assessing the EXAFS of the used catalysts a Pd-Pd lattice expansion was identified, which is attributed to the formation of Pd carbide, which is proposed to be responsible for the deactivation observed. It is understood this is the first report of this deactivation pathway for the hydrogenation of α, β-unsaturated aldehydes.

5. References

1. Nanda, S.; Mohammad, J.; Reddy, S. N.; Kozinski, J. A.; Dalai, A. K. *Biomass Conversion and Biorefinery,* 2014**, *4*** (2), 157-191.
2. Loow, Y.-L.; Wu, T. Y.; Md. Jahim, J.; Mohammad, A. W.; Teoh, W. H. *Cellulose,* 2016**, *23*** (3), 1491-1520.
3. Lange, J. P.; van der Heide, E.; van Buijtenen, J.; Price, R. *ChemSusChem,* 2012**, *5*** (1), 150-166.
4. Huber, G. W.; Iborra, S.; Corma, A. *Chemical Reviews,* 2006**, *106*** (9), 4044-4098.
5. Li, G.; Li, N.; Li, S.; Wang, A.; Cong, Y.; Wang, X.; Zhang, T. *Chemical Communications,* 2013**, *49*** (51), 5727-5729.
6. Lange, J.-P.; van der Heide, E.; van Buijtenen, J.; Price, R. *ChemSusChem,* 2012**, *5*** (1), 150-166.
7. Bohre, A.; Dutta, S.; Saha, B.; Abu-Omar, M. M. *Acs Sustainable Chemistry & Engineering,* 2015**, *3*** (7), 1263-1277.
8. O'Driscoll, Á.; Leahy, J. J.; Curtin, T. *Catalysis Today,* 2017**, *279, Part 2*,** 194-201.
9. Corma, A.; Iborra, S.; Velty, A. *Chemical Reviews,* 2007**, *107*** (6), 2411-2502.
10. Yan, K.; Wu, G. S.; Lafleur, T.; Jarvis, C. *Renewable & Sustainable Energy Reviews,* 2014**, *38*,** 663-676.
11. Ide, M. S.; Hao, B.; Neurock, M.; Davis, R. J. *ACS Catalysis,* 2012**, *2*** (4), 671-683.
12. Nakagawa, Y.; Nakazawa, H.; Watanabe, H.; Tomishige, K. *Chemcatchem,* 2012**, *4*** (11), 1791-1797.
13. Panagiotopoulou, P.; Vlachos, D. G. *Applied Catalysis a-General,* 2014**, *480*,** 17-24.
14. Nakagawa, Y.; Takada, K.; Tamura, M.; Tomishige, K. *ACS Catalysis,* 2014**, *4*** (8), 2718-2726.
15. Biradar, N. S.; Hengne, A. M.; Birajdar, S. N.; Niphadkar, P. S.; Joshi, P. N.; Rode, C. V. *Acs Sustainable Chemistry & Engineering,* 2014**, *2*** (2), 272-281.
16. Rao, R.; Dandekar, A.; Baker, R. T. K.; Vannice, M. A. *Journal of Catalysis,* 1997**, *171*** (2), 406-419.
17. Nagaraja, B. M.; Padmasri, A. H.; Raju, B. D.; Rao, K. S. R. *Journal of Molecular Catalysis a-Chemical,* 2007**, *265*** (1-2), 90-97.
18. Rao, R. S.; Baker, R. T. K.; Vannice, M. A. *Catalysis Letters,* 1999**, *60*** (1-2), 51-57.
19. Sitthisa, S.; Resasco, D. E. *Catalysis Letters,* 2011**, *141*** (6), 784-791.
20. Sitthisa, S.; Sooknoi, T.; Ma, Y.; Balbuena, P. B.; Resasco, D. E. *Journal of Catalysis,* 2011**, *277*** (1), 1-13.
21. Sitthisa, S.; An, W.; Resasco, D. E. *Journal of Catalysis,* 2011**, *284*** (1), 90-101.

22. Aldosari, O. F.; Iqbal, S.; Miedziak, P. J.; Brett, G. L.; Jones, D. R.; Liu, X.; Edwards, J. K.; Morgan, D. J.; Knight, D. K.; Hutchings, G. J. *Catalysis Science & Technology,* 2016**, *6*** (1), 234-242.
23. Iqbal, S.; Liu, X.; Aldosari, O. F.; Miedziak, P. J.; Edwards, J. K.; Brett, G. L.; Akram, A.; King, G. M.; Davies, T. E.; Morgan, D. J.; Knight, D. K.; Hutchings, G. J. *Catalysis Science & Technology,* 2014**, *4*** (8), 2280-2286.
24. King, G. M.; Iqbal, S.; Miedziak, P. J.; Brett, G. L.; Kondrat, S. A.; Yeo, B. R.; Liu, X.; Edwards, J. K.; Morgan, D. J.; Knight, D. K.; Hutchings, G. J. *Chemcatchem,* 2015**, *7*** (14), 2122-2129.
25. Shekhar, R.; Barteau, M. A.; Plank, R. V.; Vohs, J. M. *The Journal of Physical Chemistry B,* 1997**, *101*** (40), 7939-7951.
26. Vorotnikov, V.; Mpourmpakis, G.; Vlachos, D. G. *ACS Catalysis,* 2012**, *2*** (12), 2496-2504.
27. Bhogeswararao, S.; Srinivas, D. *Journal of Catalysis,* 2015**, *327***, 65-77.
28. Schoenbaum, C. A.; Schwartz, D. K.; Medlin, J. W. *Accounts of Chemical Research,* 2014**, *47*** (4), 1438-1445.
29. Pang, S. H.; Schoenbaum, C. A.; Schwartz, D. K.; Medlin, J. W. *Nat Commun,* 2013**, *4***.
30. Grimme, S. *Journal of Computational Chemistry,* 2006**, *27*** (15), 1787-1799.
31. Blöchl, P. E. *Physical Review B,* 1994**, *50*** (24), 17953-17979.
32. Kresse, G.; Hafner, J. *Physical Review B,* 1994**, *49*** (20), 14251-14269.
33. Kresse, G.; Hafner, J. *Physical Review B,* 1993**, *47*** (1), 558-561.
34. Kresse, G.; Furthmüller, J. *Physical Review B,* 1996**, *54*** (16), 11169-11186.
35. Perdew, J. P.; Burke, K.; Ernzerhof, M. *Physical Review Letters,* 1996**, *77*** (18), 3865-3868.
36. Singh-Miller, N. E.; Marzari, N. *Physical Review B,* 2009**, *80*** (23), 9.
37. Bianchi, C. L.; Canton, P.; Dimitratos, N.; Porta, F.; Prati, L. *Catalysis Today,* 2005**, *102–103*** (0), 203-212.
38. Wang, Z. W.; Palmer, R. E. *Nano Letters,* 2012**, *12*** (1), 91-95.
39. Jian, N.; Palmer, R. E. *Journal of Physical Chemistry C,* 2015**, *119*** (20), 11114-11119.
40. Wells, P. P.; Crabb, E. M.; King, C. R.; Wiltshire, R.; Billsborrow, B.; Thompsett, D.; Russell, A. E. *Physical Chemistry Chemical Physics,* 2009**, *11*** (27), 5773-5781.
41. Hadjiivanov, K. I.; Vayssilov, G. N. *Advances in Catalysis, Vol 47,* Gates, B. C.; Knozinger, H., Eds. Elsevier Academic Press Inc, 2002; Vol. 47, pp 307-511.

42. Zhu, H. Q.; Qin, Z. F.; Shan, W. J.; Shen, W. J.; Wang, J. G. *Journal of Catalysis*, 2004**, *225*** (2), 267-277.

43. Lear, T.; Marshall, R.; Lopez-Sanchez, J. A.; Jackson, S. D.; Klapotke, T. M.; Baumer, M.; Rupprechter, G.; Freund, H. J.; Lennon, D. *Journal of Chemical Physics*, 2005**, *123*** (17), 13.

44. Tew, M. W.; Nachtegaal, M.; Janousch, M.; Huthwelker, T.; van Bokhoven, J. A. *Physical Chemistry Chemical Physics*, 2012**, *14*** (16), 5761-5768.

45. McCaulley, J. A. *Journal of Physical Chemistry*, 1993**, *97*** (40), 10372-10379.

46. McCaulley, J. A. *Physical Review B*, 1993**, *47*** (9), 4873-4879.

47. Setiawan, A.; Kennedy, E. M.; Dlugogorski, B. Z.; Adesina, A. A.; Tkachenko, O.; Stockenhuber, M. *Energy Technology*, 2014**, *2*** (3), 243-249.

48. Teschner, D.; Vass, E.; Havecker, M.; Zafeiratos, S.; Schnorch, P.; Sauer, H.; Knop-Gericke, A.; Schloegl, R.; Chamam, M.; Wootsch, A.; Canning, A. S.; Gamman, J. J.; Jackson, S. D.; McGregor, J.; Gladden, L. F. *Journal of Catalysis*, 2006**, *242*** (1), 26-37.

Chapter Five. Pd/TiO_2 for the Hydrogenation of *p*-Nitrophenol

1. Introduction

p-Nitrophenol, arising in industrial wastewater from dyes, pesticides and explosives is a concern to both human health and the environment due to its high toxicity.[1-2] Exposure may cause damage to blood cells and the central nervous system and so its transformation to a more benign compound is needed to combatthis issue.[3]

Current methods of removal include adsorption,[4] photo-degradation[5-6] and electrochemical treatment.[7] However, all of these processes suffer from high costs or long treatment times, making them unfeasible. An alternate is the transformation of *p*-nitrophenol, such as hydrogenation to produce *p*-aminophenol, over a stable heterogeneous catalyst.

The organic compound, *p*-aminophenol, has many important uses in present day life. Most commonly it is used as an intermediate in the pharmaceutical industry for the manufacturing of analgesic and antipyretic drugs, including paracetamol.[8-9] It is also used as a dyeing agent in wood stains, fur and feathers.[10] The conventional process in the production of *p*-aminophenol is through the iron-acid reduction of *p*-nitrophenol or nitrobenzene. However, these processes result in large formations of Fe-FeO sludge (1.2 kg / kg product)[11] causing major disposal problems and environmental concerns.[12] Alternatively, the hydrogenation of nitrobenzene can be performed using noble metal catalysts and concentrated sulphuric acid,[12] albeit generating side products such as aniline and smaller amounts of other impurities.[13] In summary, the direct hydrogenation of *p*-nitrophenol over stable heterogeneous catalysts is not only favourable to alleviate many waste pollutants, but to produce important chemical intermediates.

The hydrogenation process is known to occur at room temperature when $NaBH_4$ is the choice of reductant, due to its strong reducing power, but an alternative reductant is hydrogen.[14] Although the use of a milder reagent such as hydrogen appears

favourable, high temperatures and pressures are often required, rendering the process unsustainable.[14]

Previous work on this reaction has focused on Ni[11, 15-16] and precious metal based catalysts.[17-20] Although Ni based catalysts are lower in cost, the reported *p*-nitrophenol hydrogenation activities are low, even when higher temperatures (100°C) are enforced. Lu *et al.* observed catalytic activities of 13.8 and 40.0 mol (mol Ni)$^{-1}$ hr^{-1}, for Ni/TiO_2 and Ni/Kieselguhr (naturally occurring silica/alumina) catalysts, respectively, with these values being typical of Ni catalysts.[11] Moreover, in some reports 100 % selectivity to *p*-aminophenol is difficult to achieve as Ni can also reduce the benzene ring.[11]

Au catalysts have been investigated for the hydrogenation reaction, including free and immobilised nanoparticles.[21-22] Ismail *et al.* performed systematic studies, investigating the effect of Au particle size and surface area, on the hydrogenation activity. A 6-fold increase in catalytic activity was observed when the Au particle size was decreased from 350 to 25 nm, attributed to the higher metal surface area for the smaller Au particles.[21] Although this study represents a particle size effect on activity, the particle sizes are much larger than is achieved using the sol-immobilisation method, and so a comprehensive study at smaller size domains is of interest.

Pd based catalysts have undoubtedly exhibited the best overall performance for this hydrogenation reaction. There are many literature examples focusing on both Pd nanoparticles supported in solution by polymers,[20] or supported on to solid matrices such as carbon,[23-26] metal oxides[14] and metal-organic framework (MOF) structures.[27] The support material is typically designed to have a high surface area to promote a high dispersion of Pd, which is ultimately the active species. Figure 1 illustrates the Pd metal loading effect, in which increasing the loading from 0.1 to 0.5 wt. % causes a sharp increase in activity, as a result of the increased number of active sites, but with little effect thereafter, as a consequence of particle aggregation and loss of dispersion. This behaviour is consistent with the work of Johnson *et al.*, in which it was demonstrated that Pd clusters sizes between 10 to 50 atoms exhibit size dependent activity, whilst larger nanoparticles contain a catalytically inactive core.[17]

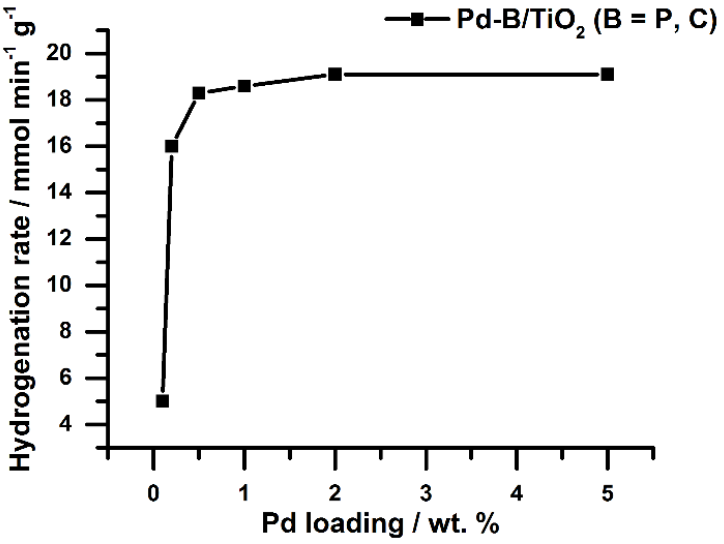

Figure 1. Effect of Pd-loading on the catalytic activity of Pd–B/TiO_2 amorphous catalyst in the hydrogenation of *p*-nitrophenol reaction.[28]

In the present chapter, PVA-stabilised Pd/TiO_2 catalysts, with a Pd loading of 0.2 wt. %, are prepared using the sol-immobilisation method with temperature control described in chapter 2, section 2. The effect of temperature on the stability of the metal nanoparticles, as well as the effect of Pd metal loading on metal particle size and dispersion are explored. For the catalytic hydrogenation of *p*-nitrophenol, TiO_2 supported catalysts have limited studies despite the high chemical stability of this material under the reaction conditions. As the catalytic activity is correlated with the total Pd surface area, this reaction is commonly used as a 'model' reaction to examine the Pd surface area of the catalyst. However, it has already been demonstrated in chapters 3 for Au, and more specifically in chapter 4 for Pd, that small metal clusters can be generated using this modified sol-immobilisation method, making them ideal candidates for this reaction. The metal nanoparticle properties are 'preformed' and so the effect of metal loading on the Pd normalised activity (for the same average Pd particle size) should, in theory, be very similar. This hypothesis is explored by comparing the performances of 0.2 and 1 wt. % Pd catalysts in the catalytic hydrogenation of *p*-nitrophenol, with the latter metal loading catalysts the same materials that were prepared and presented in chapter 4. In the present study the focus is on the Pd catalysts prepared solely in H_2O.

2. Experimental Details

2.1. Catalyst Synthesis

Pd/TiO$_2$ catalysts, with Pd weight loadings of 0.2 and 1 wt. %, were used in this study. A modified sol-immobilisation method, as detailed in chapter 2, section 2, was used to prepare 0.2 wt. % Pd/TiO$_2$ catalysts applying H$_2$O as the solvent, whereas the 1 wt. % Pd/TiO$_2$ catalysts were the same as those prepared in chapter 4. The unsupported Pd colloid was also used for catalytic testing for comparative purposes. Table 1 details the conditions used, as well as the abbreviated names to be used throughout the chapter.

Table 1. Temperature, solvent environments and Pd metal loading to which each Pd/TiO$_2$ catalyst was prepared as well as the sample notation to be used throughout.

Temperature / °C	Theoretical wt. % Pd loading	Sample notation
1	0	PdA1 colloid
1	1	PdA1
25	1	Pd A2
50	1	Pd A3
75	1	Pd A4
1	0.2	0.2 PdA1
30	0.2	0.2 PdA2
50	0.2	0.2 PdA3
75	0.2	0.2 PdA4

2.2. UV-Vis, MP-AES, TEM and Transmission IR Analysis

The details of all the techniques used to characterise the catalysts can be found in chapter 2. MP-AES analysis was performed by Kristina Penman.

2.3. Pd K edge XAFS Investigations

Chapter 4, section 2.3, gives the details of the Pd K-edge XAFS measurements performed on the 1 wt. % Pd/TiO$_2$ prepared catalysts. For the 0.2 wt. % Pd/TiO$_2$ catalysts, Pd K edge XAFS studies were carried out on the B18 beamline at the Diamond Light Source, Didcot, U.K. Measurements were performed in fluorescence mode using a QEXAFS set-up with a fast-scanning Si(311) double crystal

monochromator and a 36 element Ge detector. The undiluted samples were pressed into pellets (100 mg, area = 1.3 cm^2) for analysis. The time resolution of the spectra was 2 min/spectrum (k_{max} = 14). On average, 25 scans were acquired to improve the signal-to-noise level of the data.

2.4. Catalytic Hydrogenation of *p*-Nitrophenol

The experimental set up and general reaction conditions for the catalytic hydrogenation of *p*-nitrophenol are detailed in chapter 2, section 13. For each set of testing, specific conditions will be outlined.

As previously mentioned, when in the presence of a base, *p*-nitrophenol forms *p*-nitrophenolate ions, resulting in a red shift in the peak in the UV-Vis spectrum, from 313 to 400 nm.[29] It is widely documented that the *p*-nitrophenol hydrogenation reaction does not occur in the absence of a catalyst, nor on TiO_2 alone,[21] and so the decrease of the absorption peak at 400 nm during a catalytic reaction, illustrated in figure 2A, is a result of *p*-nitrophenol conversion, and is solely attributed to the catalytic activity of the Pd catalysts. The peak at 300 nm is that from *p*-aminophenol, rising with time of reaction as a result of its formation.[29]

The decrease in the peak at 400 nm (*p*-nitrophenolate) was used to calculate the catalytic conversion. In order to perform this, all UV-Vis spectra were manually translated in the OriginPro software, so that the absorbance at 500 nm was equal to zero, as illustrated in figure 2B. This translation process was necessary due to the variations in the UV-Vis baseline as a result of the TiO_2 absorbance; initiating the reaction suspended TiO_2 in the mixture. The absorbance of *p*-nitrophenolate at 400 nm can be used in the Beer Lambert law to calculate *p*-nitrophenolate concentration, from which reaction conversion can be calculated, with time.

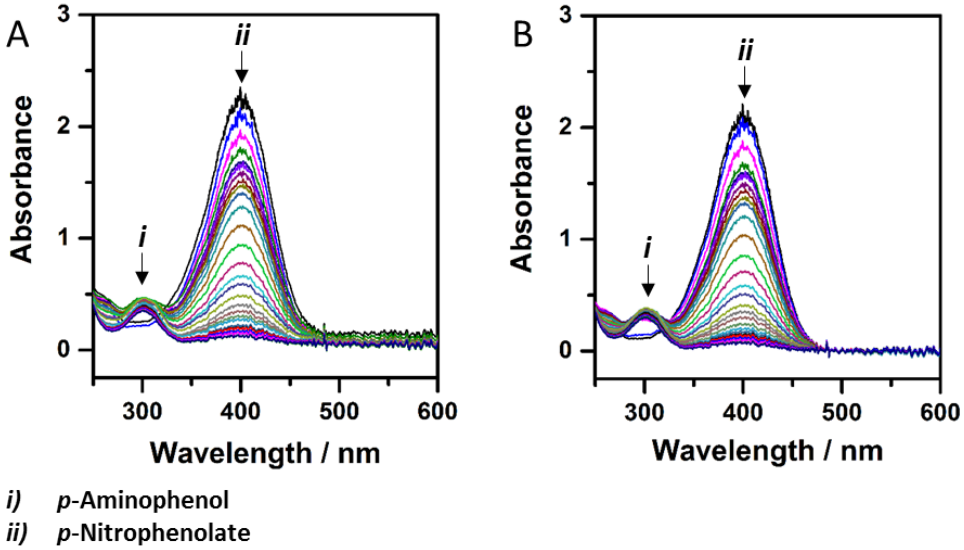

Figure 2. UV-Vis spectra collected during the catalytic hydrogenation of *p*-nitrophenol using a 1 wt. % Pd/TiO_2 catalyst; A) before baseline correction and B) after baseline correction.

3. Results and Discussion

The characterisation results for the 1 wt. % Pd/TiO_2 catalysts can be found in chapter 4, section 3. In the present section, the characterisation results for the 0.2 wt. % Pd catalysts are discussed, and compared to the 1 wt. % catalysts where necessary.

3.1. MP-AES

After immobilisation of Pd metal on to the support, catalysts were examined in MP-AES to assess the Pd metal weight loadings. Table 2 details the Pd concentrations (ppm) of each sample, with this being obtained at two different wavelengths, characteristic to Pd emission (340.5 and 361.0 nm). These concentrations were subsequently converted to give an average Pd metal loading on TiO_2.

Table 2. MP-AES results of the sol-immobilised prepared 0.2 wt. % Pd/TiO_2 catalysts.

	Concentrations (ppm) at different Pd wavelengths (nm) 1st repetition		**Concentrations (ppm) at different Pd wavelengths (nm) 2nd repetition**		**Average Pd wt. %**
	Pd 340.5	**Pd 361.0**	**Pd 340.5**	**Pd 361.0**	
0.2 PdA1	1.45	1.46	1.45	1.40	0.14
0.2 PdA2	1.80	1.79	1.73	1.75	0.18
0.2 PdA3	1.47	1.48	1.49	1.49	0.15
0.2 PdA4	1.65	1.65	1.65	1.66	0.17

Similarly to that observed in the preparation of the 1 wt. % Pd/TiO_2 catalysts (chapter 4, section 3.2), there is a no less than 70 % of the metal supported. The lowest temperature preparation (1°C) once again results in the lowest Pd metal loading (same as chapter 4), attributed to the lower viscosity of the solvent at this temperature prohibiting vicious stirring required to complete the metal on support immobilisation process.

3.2. UV-Vis Spectroscopy

UV-Vis spectroscopy was used to assess the formation of colloidal Pd, by observing the reduction of the metal precursor salt, K_2PdCl_4. Assessment of the peaks after 15 minutes of reduction time indicated that full reduction of the metal precursor had been completed for the colloidal Pd prepared at 50 and 75°C, which was confirmed by the disappearance of the peaks at $\lambda = 210$ and 238 nm, indicative of ligand to metal charge transfer in $[PdCl_4]^{2-}$, as illustrated in figure 3.[30] Therefore, for colloidal Pd prepared at these temperatures, subsequent immobilisation of Pd on to the TiO_2 support was performed after 15 minutes of metal reduction.

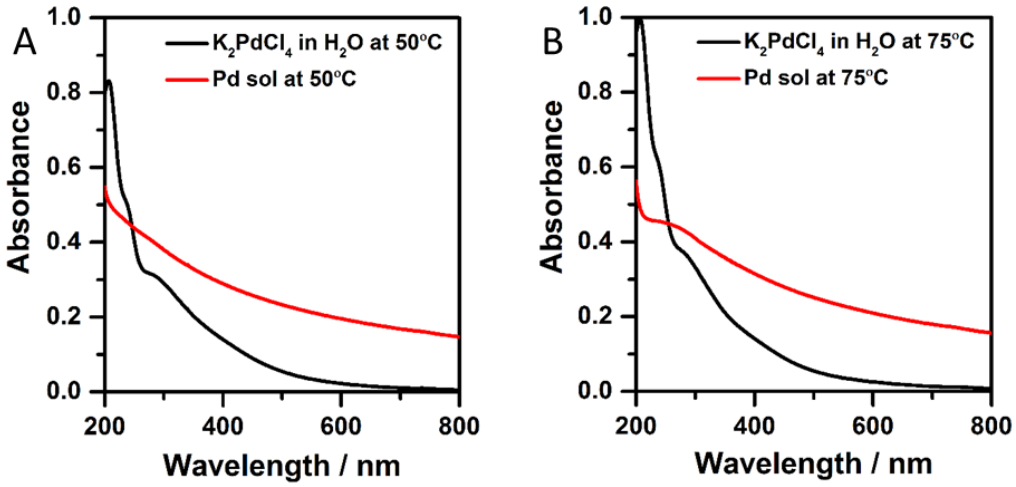

Figure 3. UV-Vis spectra of the K_2PdCl_4 precursor and the subsequent Pd sol generated after reduction of K_2PdCl_4 by $NaBH_4$, in the presence of PVA; A) prepared in a H_2O solvent at 50°C and B) prepared in a H_2O solvent at 75°C.

3.3. TEM

TEM measurements were performed to assess the Pd particle size distribution for the supported Pd catalysts, with TEM images and Pd particle size histograms illustrated in figures 4 and 5, respectively. There is a small decrease in mean Pd diameter with decreasing temperature of colloidal reduction for the 0.2 wt. % Pd/TiO_2 catalysts. The smallest and largest average Pd particle sizes, 2.2 and 2.6 nm, were achieved when colloidal Pd was prepared at 1 and 75°C, respectively. The trend in particle size is the same as that observed from the work presented in chapter 3 and chapter 4. When comparing the effect of Pd metal loading on particle size when prepared at different temperatures, it is clear a larger range of average particle size exists for the higher metal loaded catalysts (0.2 wt. % = 2.2-2.6 nm, 1 wt. % = 2.5-5.2 nm). For the Pd catalysts prepared at 1°C (PdA1 and 0.2 PdA1), the experimental protocol of preparation was identical, however, a 0.3 nm average Pd particle size difference is observed. Although it is not fully understood why the differences arises, it is hypothesised that upon immobilisation, there are preferential sites for the nanoparticles to adsorb on the TiO_2 support. Once the nanoparticle has adsorbed to the site, other small Pd colloidal clusters or single atoms aggregate to the adsorbed species, resulting in Pd particle growth. When comparing 0.2 and 1 wt. % catalysts, although the Pd colloidal concentrations are identical, there is a higher ratio of TiO_2 adsorption sites to Pd particles in the former weight loading, and so Pd growth is less. On the other hand, it could also be argued that the differences between these TEM particle sizes values are within the margins of errors, and could be as result of only counting 200-300 Pd particles, or a slight variation in human procedures during the synthesis. However, as the same trend is observed for the catalysts prepared at 25°C, it is concluded that it is not just simple error of the TEM measurement, but rather an interesting particle size effect caused during immobilisation.

By comparing the Pd metal loading effect on the average Pd particle size for the catalysts prepared at higher temperatures (50 and 75°C), it appears that the colloid is unstable, and prone to agglomeration. For the 1 wt. % Pd/TiO_2 catalysts, the average Pd particle diameters at 50 and 75°C are 2.9 and 5.2 nm, whereas for the 0.2 wt. % Pd/TiO_2 catalysts, the diameters are 2.5 and 2.6 nm, respectively. The additional 15 minutes stirring time during the colloidal formation stage for the 1 wt. % catalysts appears very influential to the Pd particle size, with the extent of agglomeration

increasing with raised temperature; the higher the temperature, the more unstable the colloid is to agglomeration (See to chapter 4, section 3.3 for TEM images of the 1 wt. % Pd catalysts).

The low contrast between Pd and TiO_2, as well as the low Pd metal loading with high dispersion (1-5 particles per image) meant the average Pd particle size was calculated over 200 particles. Performing HAADF STEM on these catalysts to observe any small Pd clusters would be very time consuming, but we consider that they are present given the fact they were observed for the 1 wt. % Pd/TiO_2 catalysts, and colloidal Pd was 'preformed' in the same conditions here.

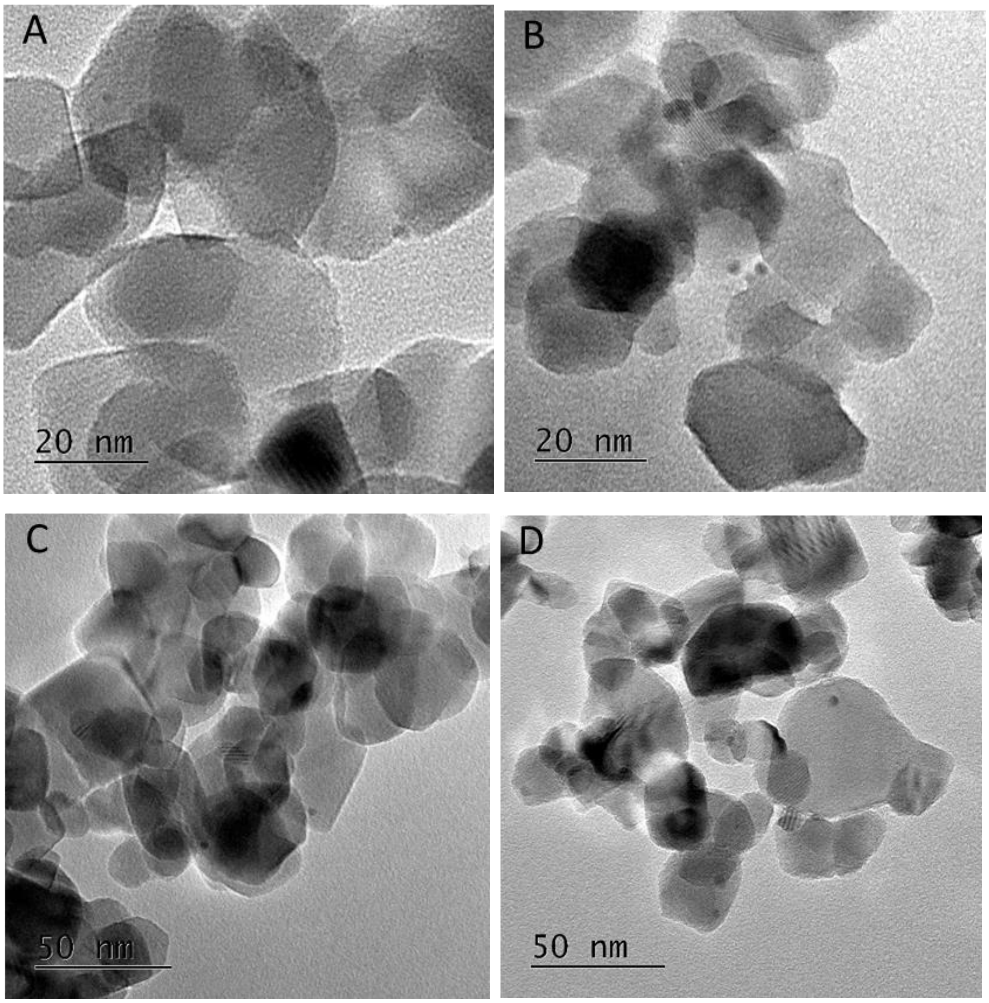

Figure 4. Selected TEM images of 0.2 wt. % Pd/TiO_2 catalysts prepared at different temperatures, in H_2O solvent environment; A) 1°C (0.2 PdA1), B) 25°C (0.2 PdA2), C) 50°C (0.2 PdA3) and D) 75°C (0.2 PdA4).

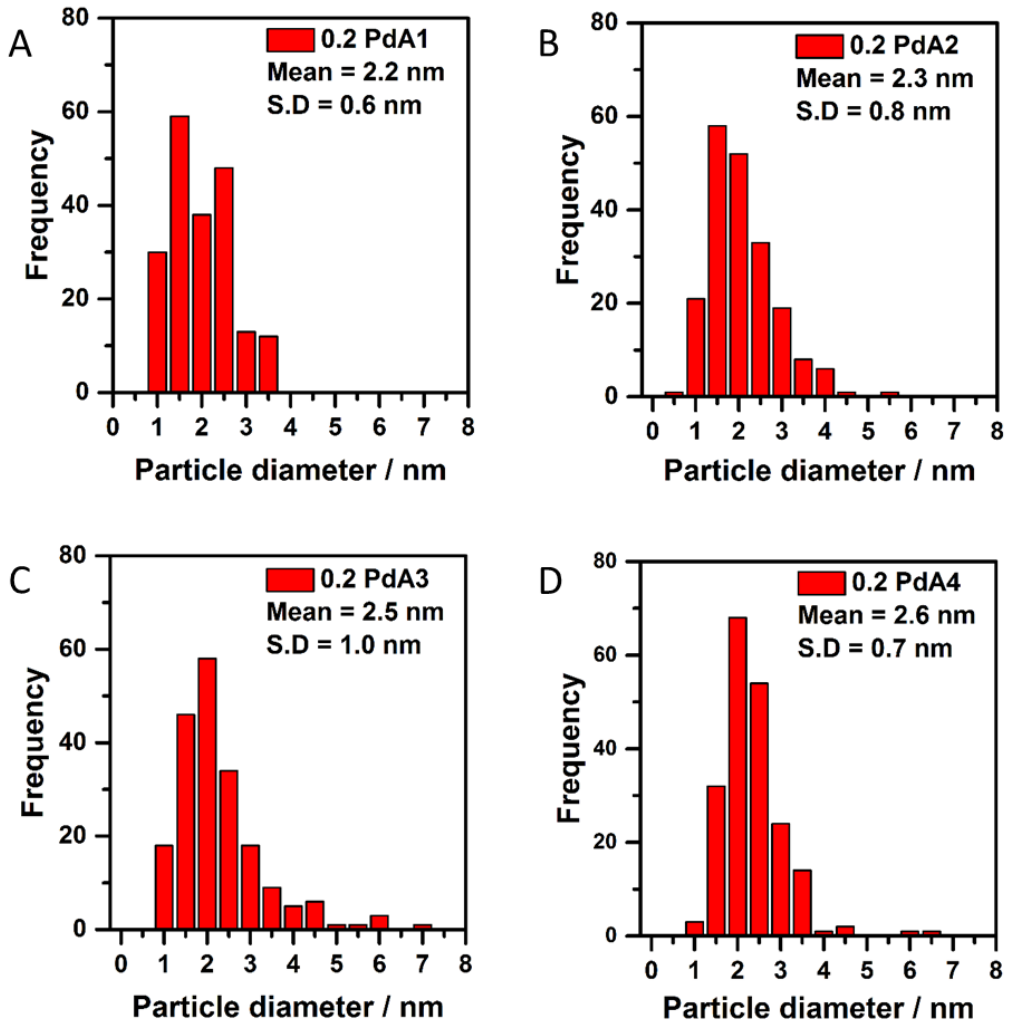

Figure 5. Pd particle size distribution histograms of 0.2 wt. % Pd/TiO_2 catalysts prepared at different temperatures, in H_2O solvent environment; A) 1°C (0.2 PdA1), B) 25°C (0.2 PdA2), C) 50°C (0.2 PdA3) and D) 75°C (0.2 PdA4).

3.4. XAFS

X-ray Absorption Near Edge Structure (XANES) was used to determine the Pd oxidation state in the Pd/TiO_2 catalysts. The ratio between Pd^{2+} and Pd^0 was performed by linear combination analysis (LCA) of the 1st derivative of the XANES profile, using PdO and Pd foil as reference standards (figure 6 and table 3). It is evident that reducing the temperature at which the colloidal Pd is prepared results in a gradual increase in Pd^{2+}, which is the same trend observed in chapter 4. To reiterate, this is due to the fact that small Pd nanoparticles form an oxidic surface layer at room temperature when exposed to the atmosphere.[31] The ratio of surface/core species increases as the average

nanoparticle diameter decreases, increasing the contribution of Pd^{2+} to the EXAFS signal.

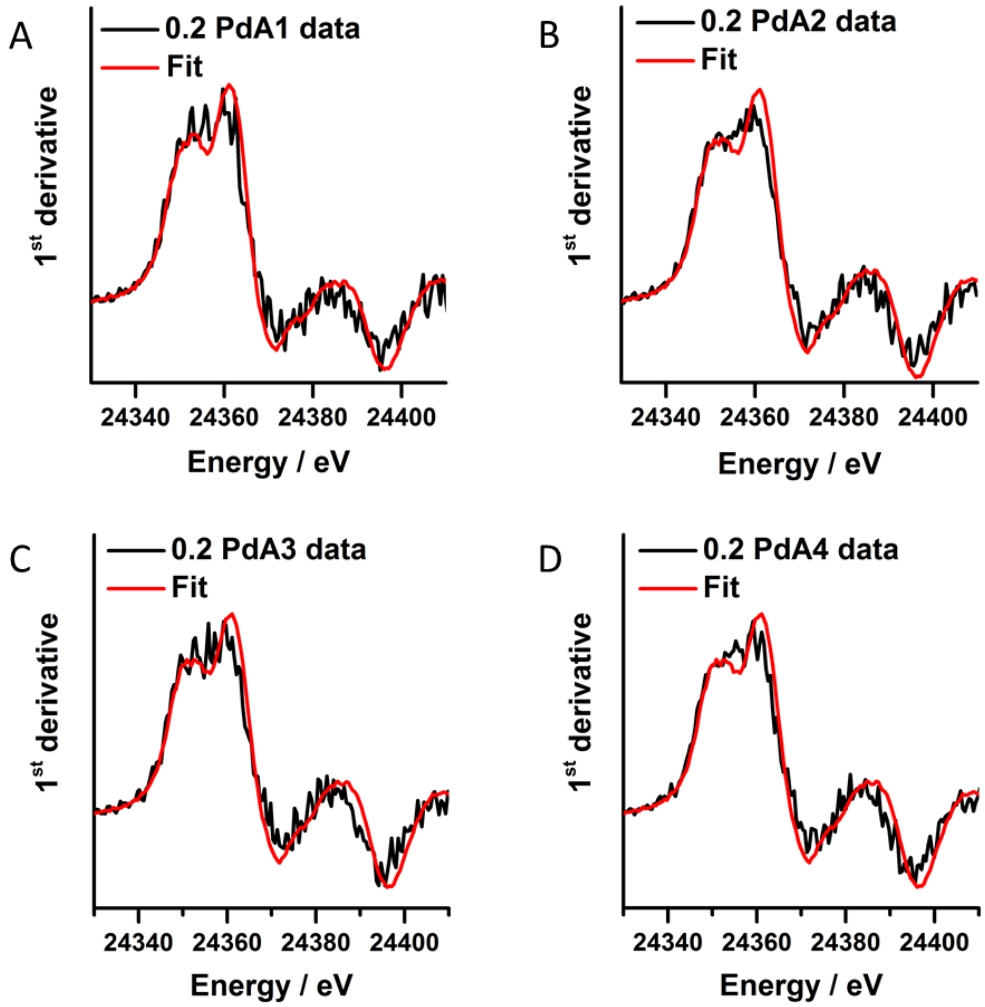

Figure 6. Linear combination fits for the different 0.2 wt. % Pd/TiO_2 catalysts using PdO and Pd foil as reference materials; A) 1°C (0.2 PdA1), B) 25°C (0.2 PdA2), C) 50°C (0.2 PdA3) and D) 75°C (0.2 PdA4).

Table 3. XANES linear combination fitting analysis. Fitting range −20 to 60.

Sample	Reference standards / %		
	Pd^{2+}	Pd foil	R_{factor}
0.2 PdA1	43	57	0.046
0.2 PdA2	34	66	0.042
0.2 PdA3	32	68	0.046
0.2 PdA4	32	68	0.044

Extended X-ray Absorption Spectroscopy (EXAFS) was used to confirm the existence of an oxidic layer on the palladium nanoparticles rather than large PdO crystallites, in the same manner as described in chapter 4, section 3.5. In the k^2-weighted Fourier transform of 0.2 PdA1 (figure 7A), the Pd-Pd scattering path that would otherwise be present at 3 Å, and can be observed in the PdO reference, is not observed in the 0.2 PdA1 data. The k^2-weighted Fourier transform of the 0.2 wt. % Pd catalysts are shown in figure 7B, and it is evident to assess the Pd particle sizes by the magnitude of the Pd-Pd scattering path at ~ 2.5 Å. The magnitude, together with the evidence from TEM analysis, support our understanding of the nanoparticle size.

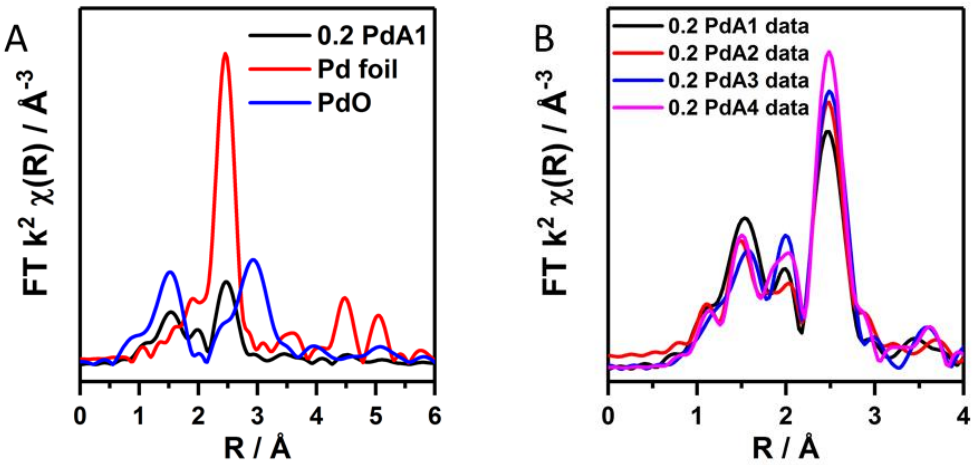

Figure 7. k^2 weighted forward Fourier transform data for A) the 0.2 PdA1 catalyst (1°C H_2O), Pd foil and PdO reference, and B) all 0.2 wt. % Pd/TiO_2 catalysts.

3.5. Transmission IR

The chemisorption of CO on metal nanoparticle systems, monitored by IR spectroscopy was employed to assess the available surface sites of the 0.2 wt. % Pd/TiO_2 catalysts (figure 8). The low Pd metal loading affected the quality of the IR bands as a result of the low number of Pd absorption sites, meaning the absorption is not Pd mass normalised. The CO bands were assigned based on the Pd work presented in chapter 4. The two bands at ~ 2134 and ~ 2145 cm^{-1} can be assigned to CO adsorbed on Pd^+ and Pd^{2+}, respectively.[32] The shape and sharpness of these bands are much the same in catalysts 0.2 PdA2, 0.2 PdA3 and 0.2 PdA4, but for 0.2 PdA1, in which the smallest average Pd diameter exists, the band is broader with adsorption up to 2152 cm^{-1}. Infrared bands consistent with linearly adsorbed CO on Pd corner sites can be

observed in all catalysts at 2080-2090 cm^{-1},[33] although the band in 0.2 PdA1 appears the most asymmetric, with a shoulder at 2063 cm^{-1}, indicating there is CO adsorption on Pd edge sites.[34] Assigning the adsorption features below 2000 cm^{-1} to bridge-bonded CO is difficult as a result of the broad bands observed.[33] For all spectra, the band starts ~1980, which is attributed to CO adsorption on facets, but for 0.2 PdA1 and 0.2 PdA2, the bands are sharper, with the peak at 1945 cm^{-1}, indicative of bridge bonded CO adsorption on edge sites.[32-33] Moreover, we can comments on the ratio of linear bonded CO:bridge bonded CO from which a trend can be observed: in general, an increased temperature of catalyst preparation increases the ratio.

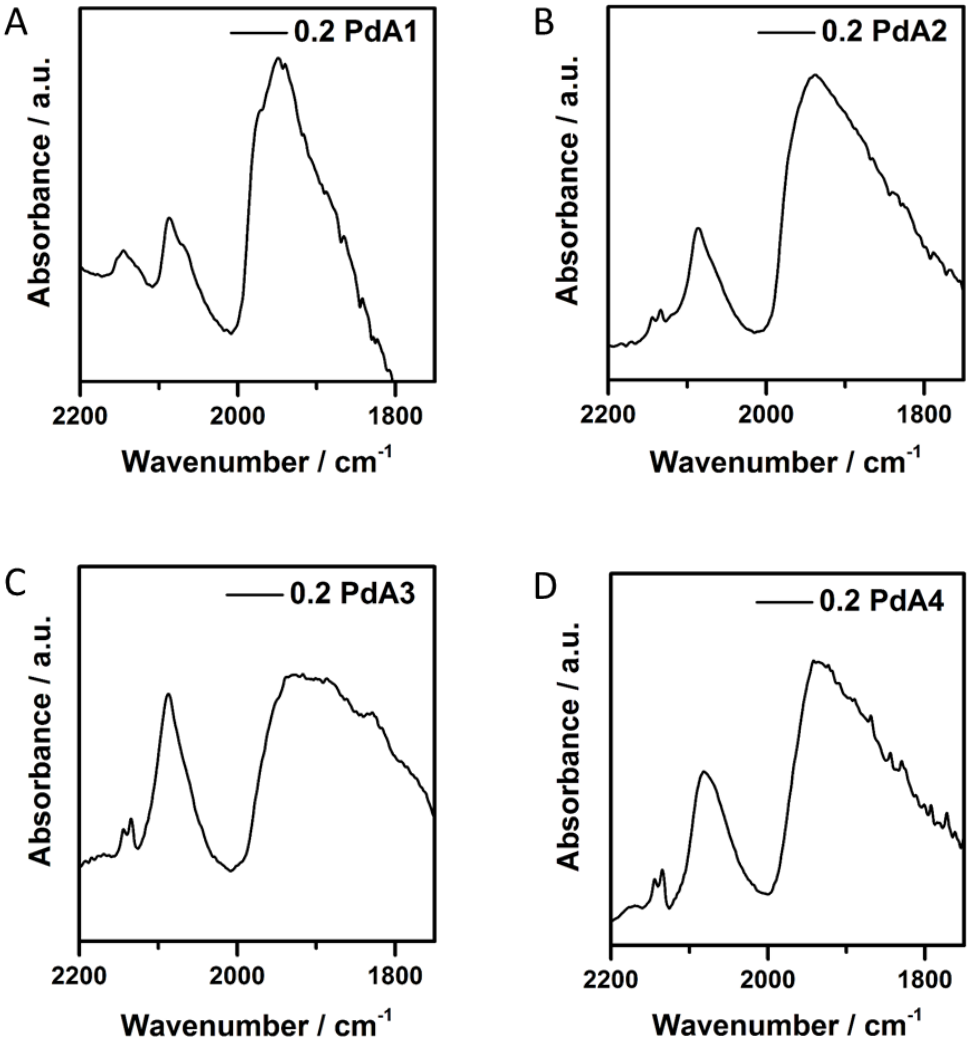

Figure 8. FTIR spectra from CO-adsorption studies on different 0.2 wt. % Pd/TiO_2 catalysts prepared at different temperatures in a H_2O solvent; A) 0.2 PdA1 (1°C), B) 0.2 PdA2 (30°C), C) 0.2 PdA3 (50°C) and D) 0.2 PdA4 (75°C).

3.6. Catalytic Hydrogenation of *p*-Nitrophenol

The catalytic performance of 0.2 and 1 wt. % Pd/TiO_2 catalysts was investigated for the hydrogenation of *p*-nitrophenol, using $NaBH_4$ as the hydrogen source. XANES analysis of both the 0.2 and 1 wt. % Pd/TiO_2 catalysts (1 wt. % presented in chapter 4 section 3.5), provides evidence that a surface oxide layer exists on the small metal nanoparticles.

The oxidation state of the active Pd species has been previously investigated and discussed. Li et al. reported that the increased hydrogenation activity was correlated with the Pd^0 content,[25] whereas Wang *et al.* found that the presence of PdO increased the activity of the catalyst.[26]

For the study presented here, we propose that all catalysts must have Pd in a zero valent state in order to establish the effect of Pd surface area (particle size) on the activity of the catalysts, for the hydrogenation of *p*-nitrophenol reaction, to achieve which, $NaBH_4$ was mixed with the Pd catalyst fifteen seconds prior to the addition of *p*-nitrophenol. Pre-treating the catalysts in this manner is not uncommon, and also prevents an induction period at the start of the reaction, caused as a result of $NaBH_4$ reacting faster with the dissolved oxygen, than with *p*-nitrophenol.[35]

To assess the reproducibility of the performed catalysis, the 0.2 PdA1 catalyst was tested three times, with the conversion profile illustrated in figure 9. It is clear the reaction is reproducible, with the maximum error in conversion at any given time point being 5 %. As very small catalyst masses are required (0.4 - 2 mg), a highly accurate balance (record down to 10^{-7} g) was needed.

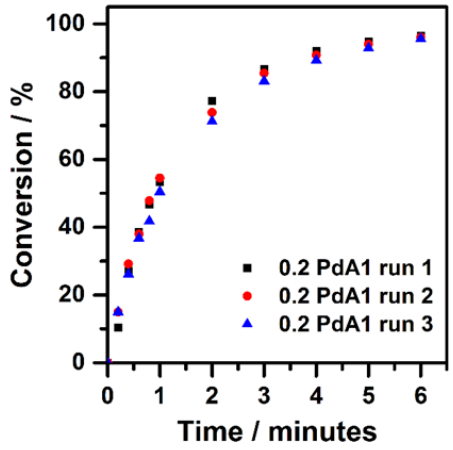

Figure 9. Hydrogenation of *p*-nitrophenol conversion profiles for 0.2 wt. % Pd/TiO_2 catalyst prepared in H_2O at 1°C for 3 separate experiments. Reaction conditions: *p*-nitrophenol/Pd molar ratio = 13.0, $NaBH_4$/*p*-nitrophenol molar ratio = 24.5.

The *p*-nitrophenol hydrogenation conversion profiles for the supported Pd catalysts, pre-treated first with $NaBH_4$, as well as colloidal Pd prepared at 1°C, are presented in figure 10. A clear difference in the catalytic activity for the 1 wt. % Pd catalysts is observed, with the rate of conversion decreasing with increased temperature of catalyst preparation. For the 0.2 wt. % Pd catalysts, the difference in the conversion rate is less pronounced, although it is clear that the TiO_2 supported Pd catalyst (0.2 PdA1) has much higher activity than the unsupported Pd nanoparticles (PdA1 colloid).

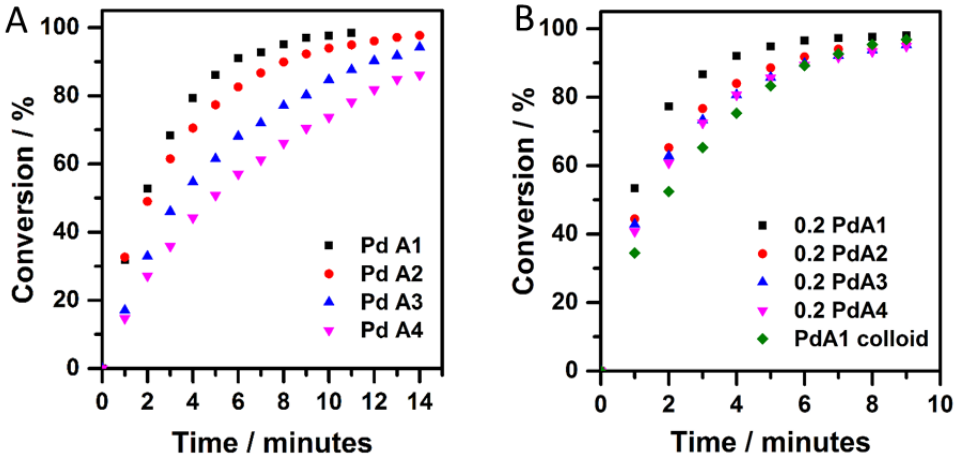

Figure 10. Hydrogenation of *p*-nitrophenol conversion profiles for; A) 1 wt. % Pd/TiO_2 catalysts and B) 0.2 wt. % Pd/TiO_2 catalysts and unsupported colloid (Pd A1-A4 denotes preparation in H_2O between 1 and 75°C). Reaction conditions: *p*-nitrophenol/Pd molar ratio = 13.0, $NaBH_4$/*p*-nitrophenol molar ratio = 24.5.

When an excess of $NaBH_4$ is used, as it is here, the reaction proceeds with pseudo first order kinetics, with the rate constant, *k*, determined *via* the first-order integrated rate law (equation 1).

$$ln[C_t] = ln[C_0] - kt \qquad \textbf{Equation 1}$$

Where C_t is the *p*-nitrophenol concentration at time t during the reaction, and C_0 is the initial *p*-nitrophenol concentration.

A plot of $\ln(C_t/C_0)$ versus time (figure 11) is therefore linear, with the gradient is equal to $-k$. For each catalyst, the rate constants were calculated and expressed in table 4.

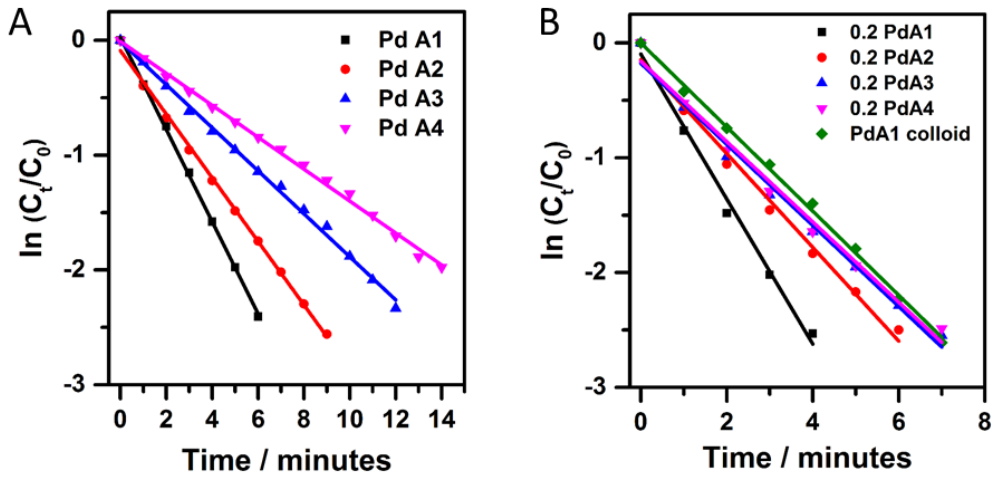

Figure 11. $\ln(C_t/C_0)$ vs time plots for; A) 1 wt. % Pd/TiO_2 catalysts and B) 0.2 wt. % Pd/TiO_2 catalysts and unsupported colloid (Pd A1-A4 denotes preparation in H_2O between 1 and 75°C) Reaction conditions: *p*-nitrophenol/Pd molar ratio = 13.0, $NaBH_4$/*p*-nitrophenol molar ratio = 24.5.

Table 4. Calculated pseudo first-order rate constants, average TEM Pd particle size and TOFs for the Pd/TiO_2 catalysts used in the hydrogenation of *p*-nitrophenol.

Catalyst	Average Pd particle size (TEM)	k^a / min^{-1}	TOF^c / hr^{-1}
Pd A1	2.5	0.401	259
Pd A2	2.7	0.277	247
Pd A3	2.9	0.187	160
Pd A4	5.2	0.139[b]	135
0.2 PdA1	2.2	0.632	333
0.2 PdA2	2.3	0.408	232
0.2 PdA3	2.5	0.353	264
0.2 PdA4	2.6	0.350	234
PdA1 colloid	-	0.366	166

[a] Rate constants calculated after 90 % conversion. [b] Rate constant calculated after 86 % conversion. [c] TOFs calculated after 2 minutes of reaction.

In catalysis, the use of high substrate/catalyst (metal) ratio whilst maintaining high conversion rates is economically favourable. The rate constant, however, does not reflect the catalytic activity in terms of the metal content, unless the same substrate/metal ratio is used. Instead, turnover frequencies (TOFs), expressed as the moles of *p*-nitrophenol converted, per mole of Pd metal, per hour, is a better evaluation of activity from an economic perspective. TOFs were calculated for each Pd catalyst (table 4), with the Pd metal loading for all the 1 wt. % catalysts set at 0.72 wt. % (Pd metal loading obtained for both PdA1 and PdA2 by MP-AES, in chapter 4, section 3.2).

Sun *et al*. reported a rate constant of 2.2 min^{-1} for a 5 wt. % Pd/C, indicating higher activity, however, the substrate/Pd ratio for this catalyst was lower (6.4), and so the Pd normalised mass activity (TOF = 70 hr^{-1}) is much lower than the Pd/TiO_2 catalysts reported in this study.[23]

There is a clear difference in TOF between the unsupported (166 hr^{-1}) and TiO_2 supported catalyst, but the enhancement is more favourable when a Pd metal loading of 0.2 wt. % (TOF = 333 hr^{-1}) is chosen, compared with 1 wt. % (TOF = 259 hr^{-1}). Combining these two observations indicates the possible roles of TiO_2 during the catalysis; the Pd-TiO_2 interaction restricts growth and agglomeration, and there is increased dispersion of Pd nanoparticles across the TiO_2. Although the pseudo first-order rate constants for the catalysts 0.2 PdA2, 0.2 PdA3 and 0.2 PdA4 exhibit a size

dependent trend, the calculated TOFs do not, showing values of 232, 264 and 234 hr^{-1}, respectively. Indeed the particle sizes are very similar for these catalysts, which, when coupled with the differing metal loadings, makes it difficult to elucidate structure-property relationships for this small scale reaction.

We showed in chapter 4 that the generation of colloidal Pd at low temperature (1°C) results in a high population of small Pd clusters, more so than when prepared at higher temperatures. Although the presence of these clusters has not been evidenced in this study, we conside rthat they are still present, and are responsible for the high activity of 0.2 PdA1 compared to the other catalysts. To the best of our knowledge, the TOF obtained for 0.2 PdA1 (333 hr^{-1}) is the highest reported value when compared to other TiO_2 supported nanoparticles (polypyrrole/TiO_2/Pd = 326 hr^{-1}).[25]

The recyclability of a catalyst is a very important attribute when considering its use in industry. Figures 12 illustrates the catalyst reusability for the 0.2 wt. % Pd/TiO_2 catalysts, in which *p*-nitrophenol hydrogenation conversion was calculated after 5 minutes of reaction time, over five successive cycles. 0.2 PdA1, in particular, showed excellent stability throughout, with the catalyst conversion maintained above 90 %. Again, this catalyst is more stable than other TiO_2 supported Pd nanoparticles, where deactivation of 42 % was observed across 6 cycles.[28] It is evident that between the 4th and 5th cycles, the conversion after 5 minutes increased (~ 3 %), however, this is within error of the catalytic experiment. It is difficult to elucidate the deactivation of the catalysts prepared between 30 and 75°C, but we propose that the irreversible adsorption of product at the nanoparticle surface is the main contributing factor.

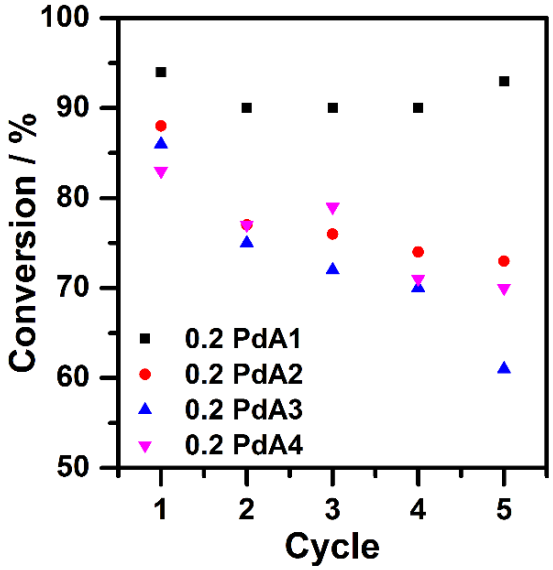

Figure 12. Catalyst recycling studies outlining the conversion achieved through five successive cycles of *p*-nitrophenol hydrogenation over each 0.2 wt. % Pd/TiO_2 catalyst. Reaction conditions: *p*-nitrophenol:Pd molar ratio = 13.0, $NaBH_4$:*p*-nitrophenol molar ratio = 24.5. Conversion calculated after 5 minutes.

4. Summary and Conclusions

The results in this chapter demonstrates once again that the sol-immobilisation method can be used to prepare metal nanoparticles with tailored properties, which subsequently show great performance in catalysis. Pd/TiO_2 catalysts were prepared using a modified sol-immobilisation method, in which colloidal Pd was formed at different temperatures, and the resulting catalysts tested for their performance in the hydrogenation of *p*-nitrophenol to *p*-aminophenol, the latter compound being an intermediate in the synthesis of paracetamol.

It was concluded that an important experimental parameter affecting the metal particle diameter during colloidal reduction, is, as well as temperature, the duration of stirring, specifically at higher temperatures (> 30°C). At low temperatures of preparation (≤ 30°C), the colloid appears stable over long stirring periods, however above this temperature, the colloid is generated quickly (in 15 opposed to 30 minutes), and is prone to aggregation (resulting in larger metal nanoparticles).

For the hydrogenation of *p*-nitrophenol reaction, Pd particle size, metal loading (0.2 *vs* 1 wt. % Pd), support effect, as well as catalyst stability was investigated. We

demonstrated the enhanced role of TiO_2 was by comparing the activities of the unsupported (TOF = 166 hr^{-1}) and supported Pd catalysts (TOF = 259-333 hr^{-1}). For the 1 wt. % Pd catalysts, where there is a larger range of particle size , a clear Pd particle size effect was observed, with lower temperatures of colloidal synthesis (smaller particles) exhibiting higher normalised Pd mass activities for the hydrogenation reaction. However, for the 0.2 wt. % Pd catalysts, the particle size effect was less apparent as a result of the similar particle sizes and different metal loadings also affecting dispersion. The 0.2 wt. % Pd/TiO_2 catalyst prepared at 1°C in H_2O undoubtedly showed the best catalytic performance, not only in terms of activity (k = 0.632 min^{-1}, TOF = 333 hr^{-1}), but also recyclability, in which 90 % conversion was achieved after 5 minutes, over 5 successive cycles. The high activity for this particular catalyst is attributed to the high population of ultrasmall Pd clusters, which results in a large total Pd surface area. As a result of the high activity maintained throughout the reusability tests, we consider that these Pd clusters are stable, and are preserved during the reaction. For both 0.2PdA1 and PdA1 catalysts, small Pd clusters exist, and the ratio of linear:bridged CO sites appear very similar, however, the activity of the former is much higher, indicating that further studies investigating how the Pd metal loading effects dispersion during synthesis, are required.

Monitoring the catalytic reaction with UV-Vis spectroscopy, particularly when TiO_2 supported catalysts are used, has its limitations; the TiO_2 absorbs in region of interest meaning non-stirring conditions are enforced and high substrate/metal ratios are difficult to achieve unless very low metal loadings or low catalyst masses are used. Nevertheless, it has been demonstrated that very active and stable catalysts can be prepared using the temperature and solvent modified sol-immobilisation method.

5. References

1. Hrapovic, S.; Majid, E.; Liu, Y.; Male, K.; Luong, J. H. T. *Analytical Chemistry,* 2006**,** ***78*** (15), 5504-5512.
2. Miranzadeh, M.; Kassaee, M. Z. *Chemical Engineering Journal,* 2014**,** ***257***, 105-111.
3. Wang, C.; Zhang, H. Y.; Feng, C.; Gao, S. T.; Shang, N. Z.; Wang, Z. *Catalysis Communications,* 2015**,** ***72***, 29-32.
4. Wu, Z. B.; Yuan, X. Z.; Zhong, H.; Wang, H.; Zeng, G. M.; Chen, X. H.; Wang, H.; Zhang, L.; Shao, J. G. *Scientific Reports,* 2016**,** ***6***, 13.
5. Chen, M. L.; Bae, J. S.; Yoon, H. S.; Lim, C. S.; Oh, W. C. *Bulletin of the Korean Chemical Society,* 2011**,** ***32*** (3), 815-820.
6. Xiong, P.; Fu, Y. S.; Wang, L. J.; Wang, X. *Chemical Engineering Journal,* 2012**,** ***195***, 149-157.
7. Canizares, P.; Saez, C.; Lobato, J.; Rodrigo, M. A. *Industrial & Engineering Chemistry Research,* 2004**,** ***43*** (9), 1944-1951.
8. M. Pinza, M. B., C. Milanese. *US Patent 6043285,* 2000.
9. Mitchell, S., *Kirk-Othmer Encyclopaedia of Chemical Technology*. 1992; Vol. 2, p 481.
10. L. Chassot, H. J. B. *US Patent 6592631 B2,* 2003.
11. Lu, H. B.; Yin, H. B.; Liu, Y. M.; Jiang, T. S.; Yu, L. B. *Catalysis Communications*, 2008**,** ***10*** (3), 313-316.
12. Rode, C. V.; Vaidya, M. J.; Chaudhari, R. V. *Organic Process Research & Development,* 1999**,** ***3*** (6), 465-470.
13. Rode, C. V.; Vaidya, M. J.; Jaganathan, R.; Chaudhari, R. V. *Chemical Engineering Science,* 2001**,** ***56*** (4), 1299-1304.
14. Zhang, D. H.; Chen, L.; Ge, G. L. *Catalysis Communications,* 2015**,** ***66***, 95-99.
15. Wang, A. L.; Yin, H. B.; Ren, M.; Lu, H. H.; Xue, J. J.; Jiang, T. S. *New Journal of Chemistry,* 2010**,** ***34*** (4), 708-713.
16. Du, Y.; Chen, H. L.; Chen, R. Z.; Xu, N. P. *Applied Catalysis a-General,* 2004**,** ***277*** (1-2), 259-264.
17. Johnson, J. A.; Makis, J. J.; Marvin, K. A.; Rodenbusch, S. E.; Stevenson, K. J. *Journal of Physical Chemistry C,* 2013**,** ***117*** (44), 22644-22651.
18. El-Sheikh, S. M.; Ismail, A. A.; Al-Sharab, J. F. *New Journal of Chemistry,* 2013**,** ***37*** (8), 2399-2407.
19. Vaidya, M. J.; Kulkarni, S. M.; Chaudhari, R. V. *Organic Process Research & Development,* 2003**,** ***7*** (2), 202-208.

20. Harish, S.; Mathiyarasu, J.; Phani, K.; Yegnaraman, V. *Catalysis Letters,* 2009***, 128*** (1-2), 197-202.
21. Ismail, A. A.; Hakki, A.; Bahnemann, D. W. *Journal of Molecular Catalysis a-Chemical,* 2012***, 358***, 145-151.
22. Lee, J.; Park, J. C.; Song, H. *Advanced Materials,* 2008***, 20*** (8), 1523-+.
23. Sun, J. W.; Fu, Y. S.; He, G. Y.; Sun, X. Q.; Wang, X. *Catalysis Science & Technology,* 2014***, 4*** (6), 1742-1748.
24. Fang, Y. X.; Wang, E. K. *Nanoscale,* 2013***, 5*** (5), 1843-1848.
25. Li, H. Q.; Han, L. N.; Cooper-White, J.; Kim, I. *Green Chemistry,* 2012***, 14*** (3), 586-591.
26. Wang, C. X.; Yang, F.; Yang, W.; Ren, L.; Zhang, Y. H.; Jia, X. L.; Zhang, L. Q.; Li, Y. F. *RSC Advances,* 2015***, 5*** (35), 27526-27532.
27. Jiang, H.; Yan, Q.; Du, Y.; Chen, R. Z. *Reaction Kinetics Mechanisms and Catalysis,* 2016***, 117*** (1), 307-317.
28. Ma, Z. Y.; Zhang, L. X.; Chen, R. Z.; Xing, W. H.; Xu, N. P. *Chemical Engineering Journal,* 2008***, 138*** (1-3), 517-522.
29. Liu, J. C.; Qin, G. W.; Raveendran, P.; Kushima, Y. *Chemistry-a European Journal,* 2006***, 12*** (8), 2132-2138.
30. Bianchi, C. L.; Canton, P.; Dimitratos, N.; Porta, F.; Prati, L. *Catalysis Today,* 2005***, 102–103*** (0), 203-212.
31. Wells, P. P.; Crabb, E. M.; King, C. R.; Wiltshire, R.; Billsborrow, B.; Thompsett, D.; Russell, A. E. *Physical Chemistry Chemical Physics,* 2009***, 11*** (27), 5773-5781.
32. Hadjiivanov, K. I.; Vayssilov, G. N. *Advances in Catalysis, Vol 47*, Gates, B. C.; Knozinger, H., Eds. Elsevier Academic Press Inc, 2002; Vol. 47, pp 307-511.
33. Zhu, H. Q.; Qin, Z. F.; Shan, W. J.; Shen, W. J.; Wang, J. G. *Journal of Catalysis,* 2004***, 225*** (2), 267-277.
34. Lear, T.; Marshall, R.; Lopez-Sanchez, J. A.; Jackson, S. D.; Klapotke, T. M.; Baumer, M.; Rupprechter, G.; Freund, H. J.; Lennon, D. *Journal of Chemical Physics,* 2005***, 123*** (17), 13.
35. Wunder, S.; Polzer, F.; Lu, Y.; Mei, Y.; Ballauff, M. *The Journal of Physical Chemistry C,* 2010***, 114*** (19), 8814-8820.

Chapter Six. Nanoparticle Synthesis using Continuous Flow Methods

1. Introduction

Traditional reactors chosen for the synthesis of heterogeneous catalysts are essentially macroscale vessels (i.e. beakers, crucibles or flasks), with the overall preparation described as a 'batch' method. Catalysts prepared in chapters 3, 4 and 5 were done so using a batch process, but there has been recent interest to prepare metal nanoparticles using 'continuous flow' methods, described as such by the manner in which the reagents are continuously flowed through a reactor, coming together at a precise mixing point.

When considering the best method to perform nanoparticle synthesis, there are many factors to consider: economics (chemical consumption and infrastructure), quantity of generated waste, reproducibility and product homogeneity (nanoparticle characteristics such as size, shape and structure). Control over local conditions (concentration, temperature and contact time) that flow synthesis offers makes the method ideal for the preparation of metal nanoparticles with tailored characteristics, over batch methods.[1-2]

There has been a steady increase in the number of studies investigating continuous flow methods for the preparation of metal nanoparticles, with particular emphasis on noble metals including Au,[3-4] Ag,[5] Pt[6] and Pd.[7] As can be observed in figure 1, polyvinyl pyrrolidone (PVP) stabilised-Au metal nanoparticles < 2 nm, were prepared in a microreactor by continuous flow methods, and displayed a far narrower particle size distribution compared with nanoparticles prepared in a batch reactor with analogous conditions.[4]

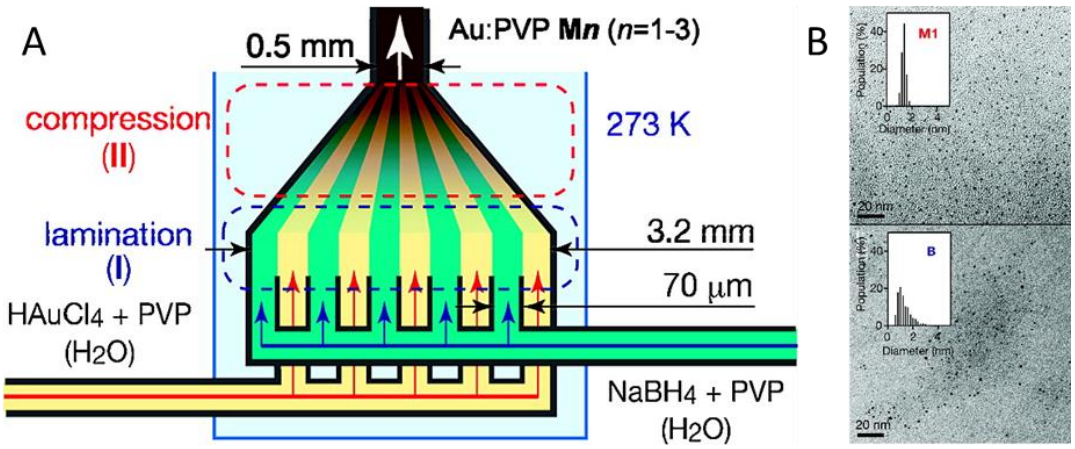

Figure 1. A) Schematic diagram of the micromixer used in the synthesis of PVP-stabilised Au particles and B) TEM images and Au particle size histograms of PVP-stabilised Au nanoparticles prepared by; M1 = continuous flow method and B = conventional batch method.[4]

The use of micro-technology for reactor design, dealing with channel dimensions from 1 to a few hundred micrometres, has grown considerably due to the advantages it holds; the large surface area to volume ratio offers enhances heat and mass transfer, as well as the efficient mixing resulting in uniform concentrations.[1] The reactor channel arrangements, flow rates and material fabrication are all important parameters dictating the flow characteristics (laminar or turbulent mixing), and the level of interaction with the reactor walls. Figure 2 illustrates a range of possible reactor shapes, each owing to a unique mixing pattern, with figure 2a mixing under laminar flow whilst figures 2b-e mix under turbulent flow.[8]

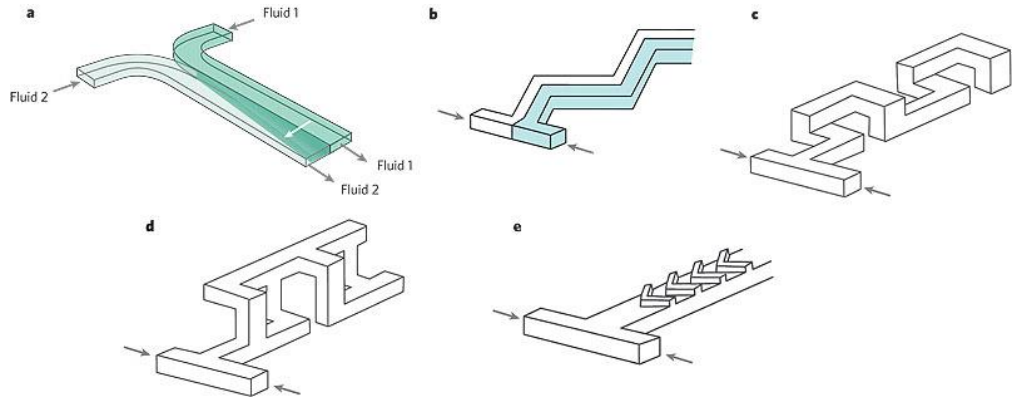

Figure 2. a) Mixing of two miscible fluid streams under laminar flow conditions. The component streams mix only by diffusion, creating a dynamic diffusive interface with predictable geometry. b) Zigzag-shaped channel c) Three-dimensional L-shaped channel d) Three-dimensional, connected out-of-plane channel and e) Staggered-herringbone grooves.[8]

The mechanism by which the colloidal metal particles initially form is still not fully understood, although, as with all such processes, it is considered that there are two main processes that occur upon addition of the reducing agent; nucleation (formation of clusters consisting of a few atoms/ions) and subsequent growth (addition to these stable nuclei to form larger metal particles).[9-10] An important factor when considering the ideal reactor fabrication is the level of interaction between the material and the species flowing through it. A low surface energy of the reactor material minimises this interaction, which, when considering the preparation of metal nanoparticles, mitigates the nucleation, growth and possible deposition of metal on the reactor walls.

To tailor metal particle morphology, it is essential to understand the nucleation and growth processes that occur during colloidal formation. Nucleation processes occur within a few hundred milliseconds, and so *in situ* experimentation is required to resolve such fast kinetics, which has severe limitations in a batch type reactor. However, such restraints are overcome by performing the synthesis in a flow set up, as each point along the mixing channel transforms into a static time point, allowing for time resolved *in situ* monitoring. There are various techniques that have been used to monitor nucleation and growth processes *in situ*, each with their own advantages and limitations, as discussed below.

The practicality of UV-Vis spectroscopy means there have been many studies observing the growth of metal nanoparticles. Information regarding the morphology on the metal nanoparticle can be inferred from the Surface Plasmon Resonance (SPR) band. For example, the red shift in the Au SPR band (figure 3), with time, indicates Au metal particle growth.[11] However, there are limitations with this technique; not all metals possess a SPR band, it is not possible to resolve any initial nucleation processes due to the time restraints and the SPR band can often be too broad to get accurate values.

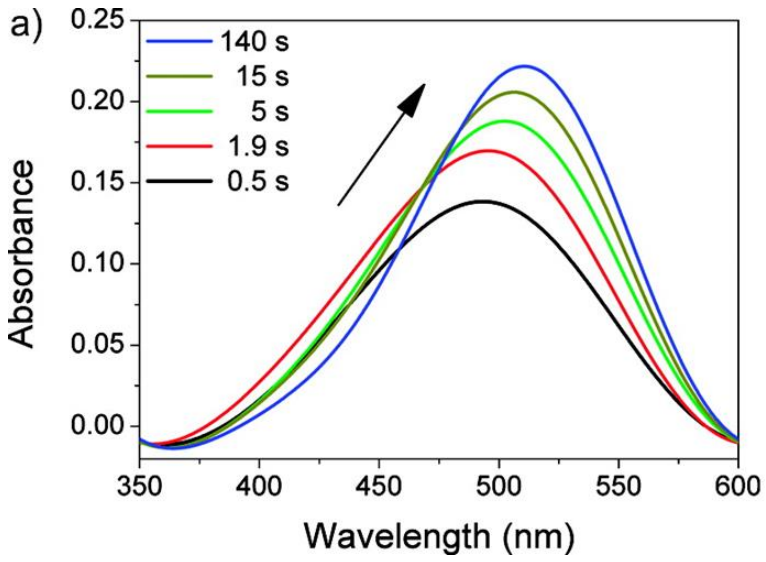

Figure 3. UV-Vis spectra monitoring the time online red shift in the SPR band of Au nanoparticles.[11]

Small Angle X-ray Scattering (SAXS) provides information on metal particle size, shape and polydispersity,[12] which, combining with the chemical and structural information inferred by XAFS, results in a very powerful technique for monitoring nucleation and growth processes in metal nanoparticle synthesis *in situ*. Polte *et al*. have performed combined XAFS/SAXS studies to monitor the synthesis of Au metal particles in both stop-flow, and continuous flow reactor, depending on the strength of reducing agent employed.[13] Performing a time resolved kinetic study in a batch reactor and using a common laboratory SAXS set up is possible when a weaker reducing agent, such as sodium citrate,[14] is employed as the process is over a long time period (up to 90 minutes). However, only a few beamlines provide the required time resolution to follow the kinetics using a strong reductant, such as $NaBH_4$,[11] in which the process occurs in the time range of milliseconds to minutes. Therefore, continuous flow methods, with rapid mixing, are required to facilitate such a fast process.[14]

To obtain high sensitivity, high intensity X-rays are required, such as synchrotron sources; however, exposure for long durations can cause beam damage.[12] The extent to which the sample is affected, is dependent on its composition and the X-ray energy, and is not a predictable process. Monitoring in a flow system, in which the reagents are constantly mixed (and fresh sample introduced), helps reduce the potential for sample beam damage.

The work in the present chapter has two main themes/aims: 1) development of the continuous flow preparation of colloidal metal nanoparticles and 2) exploration of the initial stages of metal nanoparticle formation *in situ*, a topic that is still not well understood.[15] Unlike with batch methods, PVA stabilised nanoparticles prepared using a continuous flow system have not yet been investigated. In particular, the effect of reagent flow rate on the afforded metal particle properties, will be explored. Characterisation methods to assess the metal particle sizes will include UV-Vis spectroscopy and TEM. The SPR band observed for Ag and Au colloids make these suitable metals to study. TEM can be used to image directly the colloid and/or supported metal catalyst in order to determine a particle size distribution. As mentioned, monitoring the nucleation and growth processes during metal nanoparticle synthesis in a batch method set up is difficult, and is nearly impossible when a strong reductant such as $NaBH_4$ is employed due to the rapid kinetics. Therefore, the formation of metal nanoparticles *in situ* using synchrotron techniques will be investigated, whilst also assessing and evaluating the effect of different reactor fabrications and mixing paths moving forward to the future.

2. Experimental Details – Method Development

2.1. Continuous Flow Synthesis – The Vapourtec System

The Vapourtec system (figure 4) is an instrument commonly used to perform flow chemistry. Essentially, two stainless steel Vapourtec R2 standard pumps are used to deliver reagents through a reactor, which for this work was PTFE tubing (inner diameter = 0.1 cm, total volume = 10 cm^3), with precise control of the local conditions (temperature, pressure and flow rate). The development of metal nanoparticles using continuous flow synthesis was performed using the Vapourtec, with the general preparation method outlined below:

Reagent A consisted of mixed solution, containing the metal precursor ($AgNO_3$ [Ag] = 0.17 mM or $HAuCl_4$ [Au] = 0.25 mM) and PVA (PVA/metal wt. ratio = 0.65). Reagent B was freshly prepared $NaBH_4$ solution (0.25 mM), with the flask suspended in an ice bath, to minimise the decomposition. The solvent was 18.2 Ω cm^{-2} Milli-Q H_2O. Each delivery line (32 cm, inner diameter = 0.1 cm) and pump was manually primed firstly with solvent, followed by reagent, to remove air from the system. The

reaction conditions (temperature, flow rates, residence times) were imported in to the setup control panel. Upon initiation, the reagents flowed through PTFE tubing (inner diameter = 0.1 cm, 32 cm) before mixing at the T-piece. The mixture proceeded to flow through the reactor (inner diameter = 0.1 cm PTFE tubing, 10 cm^3 volume) before exiting to yield the final product, which was collected in a beaker suspended in an ice bath, to limit any possible particle growth.

For the preparation of Au nanoparticles, the reagents were set to discharge at certain rates so as to achieve residence times through the 10 cm^3 reactor of 5, 10 and 30 minutes, and denoted as such during the results and discussion section. Each eluted colloid was collected before immobilised on to TiO_2 by vigorous stirring at pH 1-2 for 20 minutes, so as to achieve a theoretical Au loading of 1 wt. % Au.

For the preparation of Ag nanoparticles, the reagents were set to discharge at certain rates so as to achieve reactor residence times of 1, 2, 5, 10 and 15 minutes, and denoted as such during the results and discussion section.

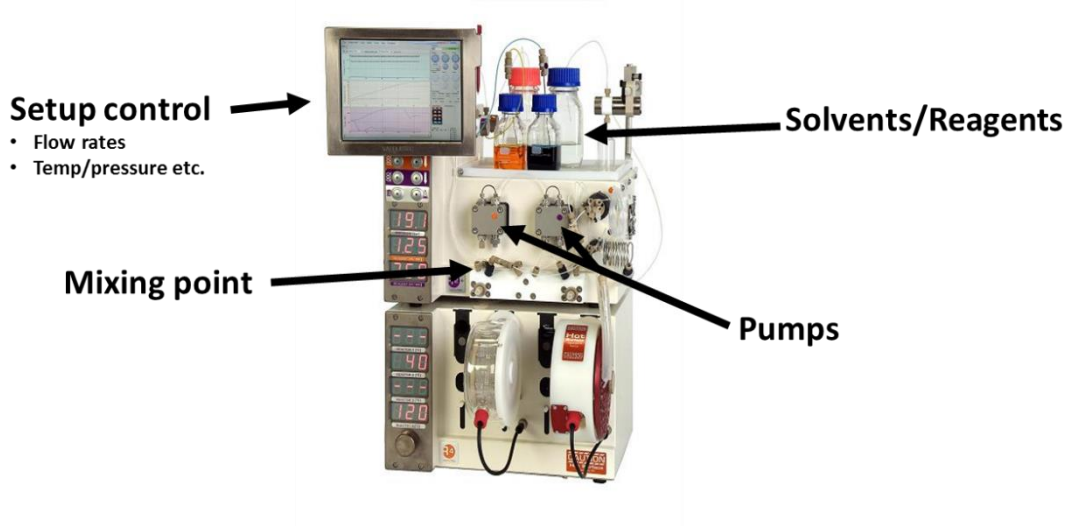

Figure 4. The Vapourtec system used to prepare metal colloids in a continuous flow set-up.

2.2. UV-Vis Spectroscopy and TEM Analysis

The details of the techniques used to characterise the catalyst can be found in chapter 2, sections 3 and 5. UV-Vis spectra were recorded of the metal sols directly from the reactor outlet, acquired between the range 200 and 800 nm. Both TiO_2 supported and unsupported metal colloids were analysed in TEM. For preparation of the unsupported

samples, 20 µL of the metal sol was allowed to evaporate on a holey carbon film supported by a 300 mesh copper grid.

2.3. *In situ* Experiment

2.3.1. Metal Nanoparticle Synthesis

Reagent A consisted of an aqueous solution of K_2PtCl_4 (0.25 mM Pt) and PVA (0.65 wt. ratio PVA/Pt). Reagent B consisted of a freshly prepared $NaBH_4$ (0.25 mM) solution. H_2O was used as the solvent. Both reagents were loaded in to 50 mL syringes connected to syringe pumps and set to discharge at a flow rate of 1 mL min^{-1}. All the lines were manually purged before, and during reactions. Three reactors, fabricated from different materials, were used during the study.

Reactor 1 – The formation of colloidal Pt was investigated firstly in a Si/glass micro-reactor (figure 5), which was manufactured and developed by Dr. Ian Silverwood, and developed by Gavriilidis.[16] The basic details of manufacture are as follows: Channels were patterned onto double-polished silicon wafers of 525 µm thickness. A thick layer of photoresist was applied, which was etched to 30 µm with deep reactive ion etching. Glass pieces of matching dimensions were cut and holes were drilled for liquid connection. Both pieces (silicon and glass) were hermetically sealed by anodic bonding at ~700 K and 800 V using a modified hotplate and high voltage power supply. Sealing was achieved by compressing the device against o-rings contained in the mount. Fluid supply to the channels was via 1/16 inch outer diameter tubing of polytetrafluoroethane (PTFE).

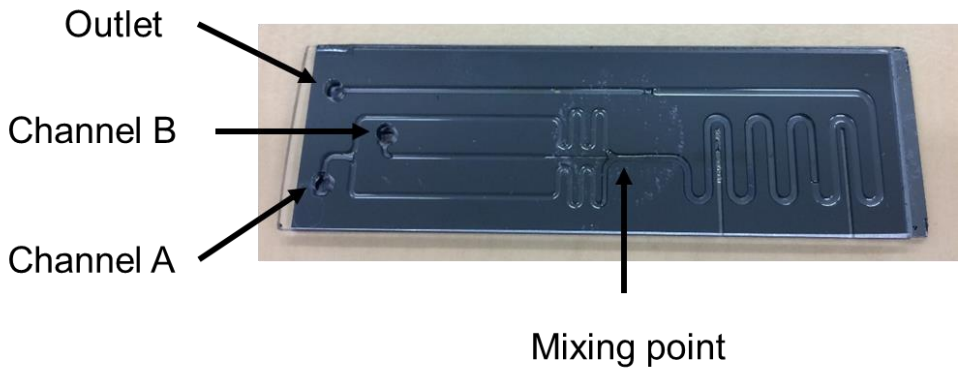

Figure 5. Si/glass micro-reactor used in the continuous flow preparation, and monitoring, of colloidal Pt.

Reactor 2 – The reactor (figure 6) was a prototype designed so as to have a PTFE tube at the mixing point, and is very similar to that used by Zhao *et al*. in a previous study.[1]

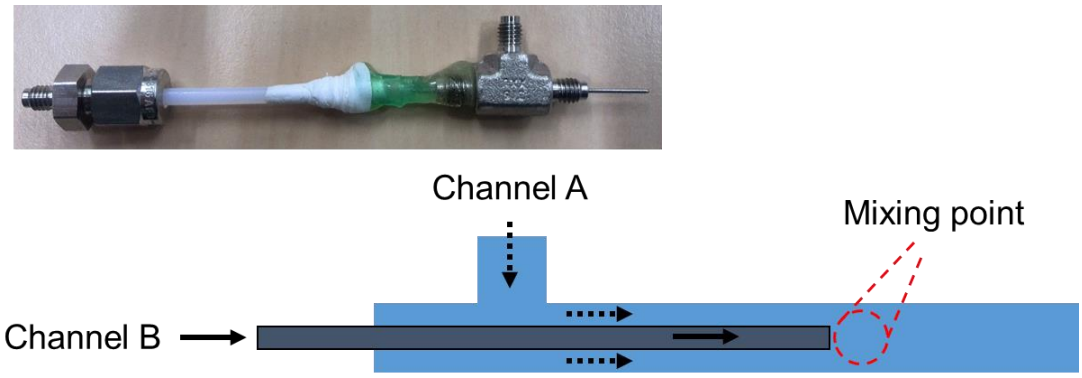

Figure 6. PTFE reactor and corresponding channel positions/flow path.

Reactor 3 – The polyether ether ketone (PEEK) fabricated reactor (figure 7) was a prototype, constructed so that the channels were Y-shaped. Simply, 1/16th inch holes were drilled in to a solid piece of PEEK (58 mm x 24 mm x 6 mm), and 1/16th inch PTFE tubing was glued at the inlets and outlet, sealing the reactor.

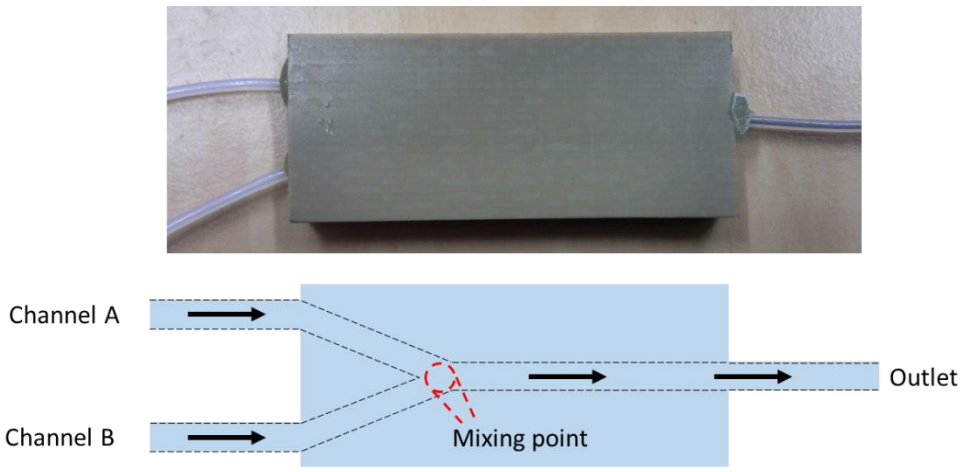

Figure 7. The reactor fabricated from PEEK, in which the channel patterns were designed in a Y-shape.

2.3.2. XAFS and XRF Studies

Pt L_3-edge XAFS and XRF studies were carried out on the I18 micro focus beamline at the Diamond Light Source, Didcot, U.K. XANES measurements were performed in fluorescence mode using a 9 element solid state fluorescence detector.

3. Results and Discussion

3.1 Au Nanoparticles

3.1.1 UV-Vis Spectroscopy

UV-Vis spectroscopy was used to assess the extent of metal reduction in the colloids produced in continuous flow using the Vapourtec system, and to investigate the position of the Au SPR band as a function of residence time (flow rate). The UV-Vis spectrum of the $HAuCl_4$ precursor (figure 8) shows a peak at 222 nm, indicative of ligand to metal charge transfer in the anion $[AuCl_4]^-$.[17] However, in the UV-Vis spectra of the Au colloids produced at different residence times, this peak disappears indicating full metal reduction has taken place. The presence of SPR band, which can be observed for all prepared colloids indicates that nanoparticulate Au has been formed. Correlating the reactor residence time during preparation with the SPR band wavelength, and therefore Au particle size, is difficult due to the broad nature of the band. Of course, to prepare a heterogeneous catalyst, the colloidal solution must be anchored on to a support material. It is not certain how the size of the metal nanoparticles changes upon immobilisation, but performing the process in a consistent manner means that any change in particle size, if any, will be identical in each sample.

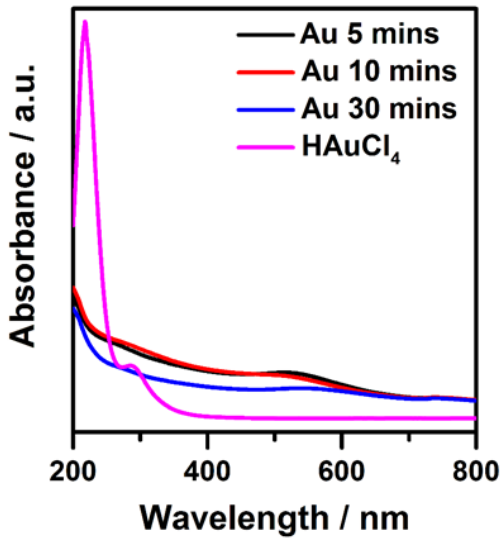

Figure 8. UV-Vis spectra indicating the SPR band for colloidal Ag prepared using a continuous flow method over varied reactor residence times (1-15 minutes), and the $HAuCl_4$ precursor material.

3.1.2. TEM

After immobilisation of colloidal Au on to TiO_2, each sample was analysed in TEM, with TEM images and representative Au particle size histograms illustrated in figure 9 and 10, respectively. It is evident that, for all samples, there is a relatively broad Au particle size distribution. The samples, in which reactor residence times of 5 and 10 minutes were employed, have very similar average Au particle sizes of 2.9 and 2.6 nm, respectively. However, a reactor residence time of 30 minutes affords Au nanoparticles with an average Au particle size of 4.4 nm, with a very broad size distribution. The results here provide useful information that the continuous flow method can be used to prepare successfully PVA-stabilised metal nanoparticles, and the contact time of the metal and reducing agent affects the resulting metal particle properties.

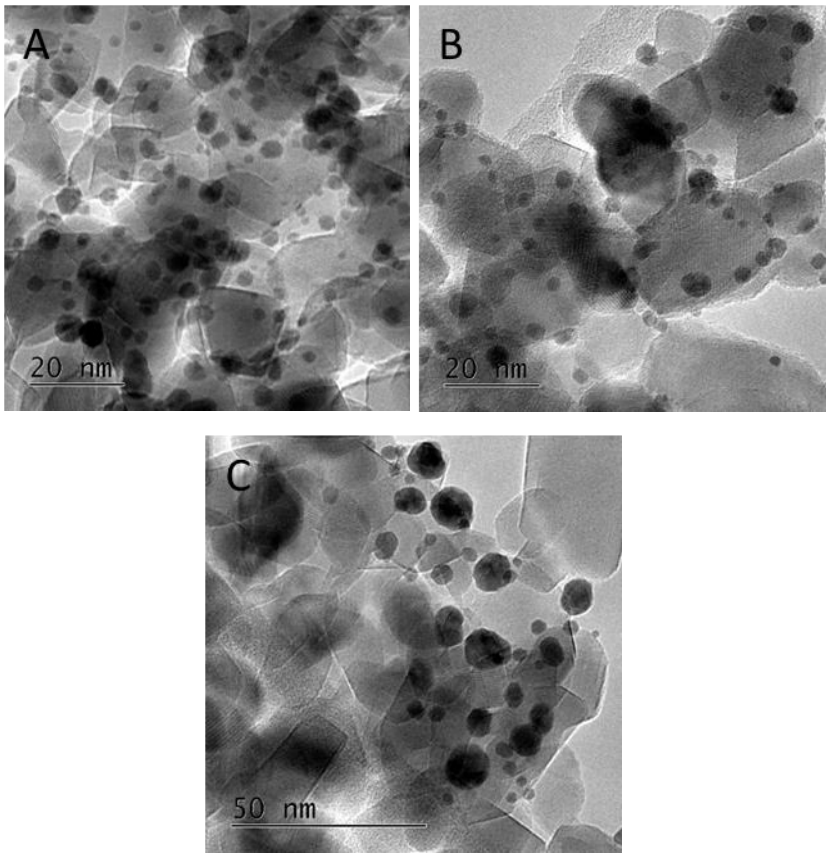

Figure 9. Selected TEM images for 1 wt. % Au/TiO_2 materials, in which colloidal Au was prepared using a continuous flow methods with a varied reactor residence time; A) 5 minutes, B) 10 minutes and C) 30 minutes.

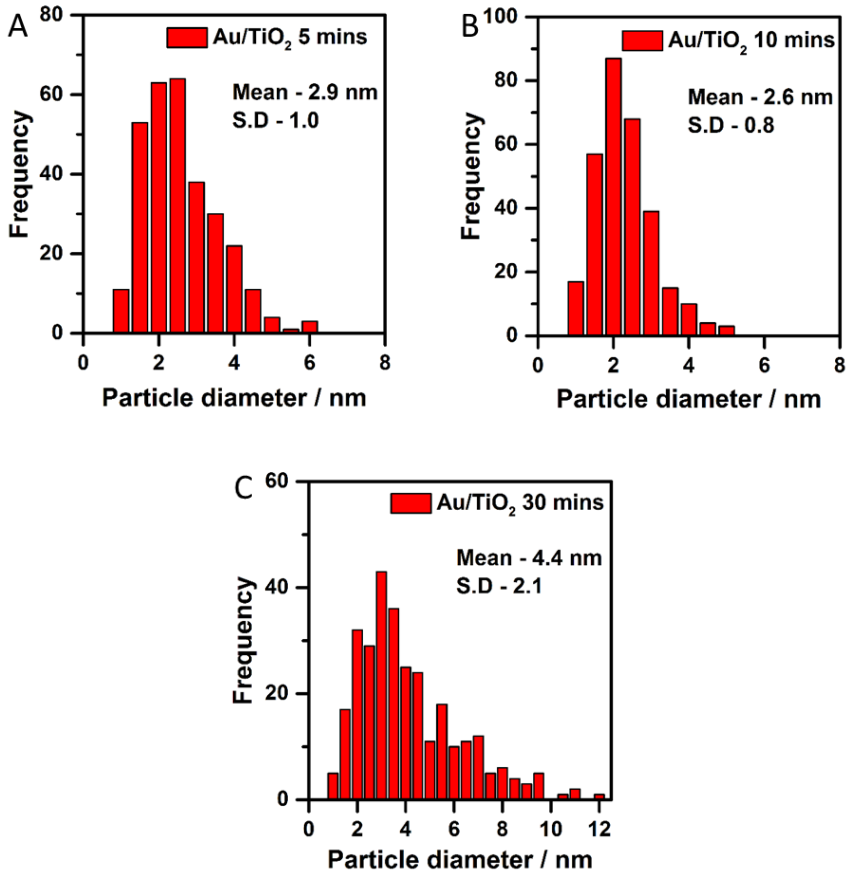

Figure 10. Au particle size histograms for 1 wt. % Au/TiO_2 materials, in which colloidal Au was prepared using a continuous flow methods with a varied reactor residence time; A) 5 minutes, B) 10 minutes and C) 30 minutes.

The reactor lines and pumps are primed with reagents prior to beginning the experiment to ensure there is no air in the system which would inhibit the flow. The use of $NaBH_4$ as the reducing agent is problematic due to the evolution of H_2 when in contact with water ($NaBH_4$ decomposition). H_2 in the system negatively effects the controlled pumping of reagents through the system, and undoubtedly hinders the contact of the two reagents at the critical mixing point. In many cases this results in a significantly lesser amount of $NaBH_4$ to be dispensed or no reagents dispensed at all due to a system failure.

3.2. Ag Nanoparticles

Ag nanoparticles were prepared using continuous flow methods over a range of reactor residence times, with focus particularly on faster flow rates (short residence).

3.2.1 UV-Vis Spectroscopy

The stronger, more pronounced SPR band that exists for Ag nanoparticles makes it a more convenient technique to monitor Ag metal nanoparticle size. Figure 11 shows the UV-Vis spectra of the Ag colloids prepared by continuous flow methods with different residence times, and it is interesting to note the position of the SPR band. For Ag colloids prepared with residence times of 1 and 2 minutes, the SPR band appears at 383 nm, and is narrow. These values are much lower in wavelength when compared to Ag nanoparticles prepared by batch methods, in which the SPR band appears at 397 nm. Interestingly, for the colloids prepared with 5, 10 and 15 minute residence times, the broad SPR bands are also found at 397 nm. The shift in the position of the Ag SPR band, which can be correlated to Ag particle size, provides important information that the Ag nanoparticle size can be tailored with continuous flow methods by varying the flow rate, and that smaller Ag nanoparticles can be prepared than with conventional batch methods.

The peak width at half maximum (PWHM) is a great indication of the relative Ag particle size distribution. For the Ag nanoparticles prepared with reactor residence times of 1 and 2 minutes, the PWHM is 45 and 51 nm, respectively, indicating a very narrow particle distribution compared with other reports in which Ag nanoparticles have been synthesised by flow methods.[18] The PWHM of Ag nanoparticles prepared with reactor residences time of 5, 10 and 15 minutes were much higher, and ranged between ~ 80 and 100 nm.

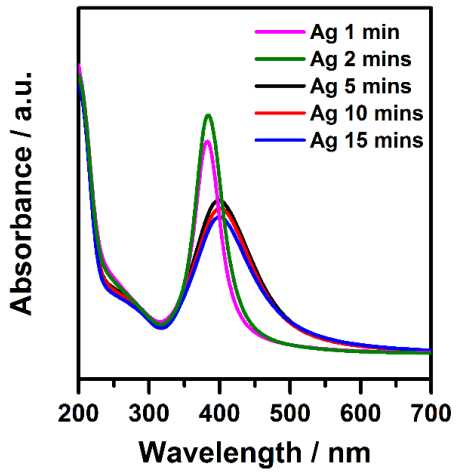

Figure 11. UV-Vis spectra indicating the SPR band for colloidal Ag prepared using a continuous flow method over varied reactor residence times (1-15 minutes).

3.2.2. TEM

TEM was employed to obtain the Ag particle size distribution, through direct imaging of the generated Ag colloid, in an attempt to understand the effect of flow rate on the resulting metal particle size. Although the Ag nanoparticles are protected by PVA, there is not the additional stabilisation of the TiO_2 support material and so the effect of the 200 keV microscope on the particle growth is not known. Upon elution from the outlet, the colloid was suspended in an ice bath so as to minimise any growth that may occur. TEM images and respective Ag particle size histograms are presented in figure 12 and 13. There is no real trend in Ag particle size with reactor residence time of preparation, unlike the results obtained with the UV-Vis analysis. Despite efforts to minimise the Ag particle growth, it is possible that the electron beam in the TEM results in particle aggregation. Nevertheless, TEM analysis provides evidence that the average Ag particle sizes of the colloids prepared by continuous flow methods (ranging between 3.7 and 4.8 nm). These values are much lower than the reports in which the corresponding batch method is used (8-9 nm) is used.[19]

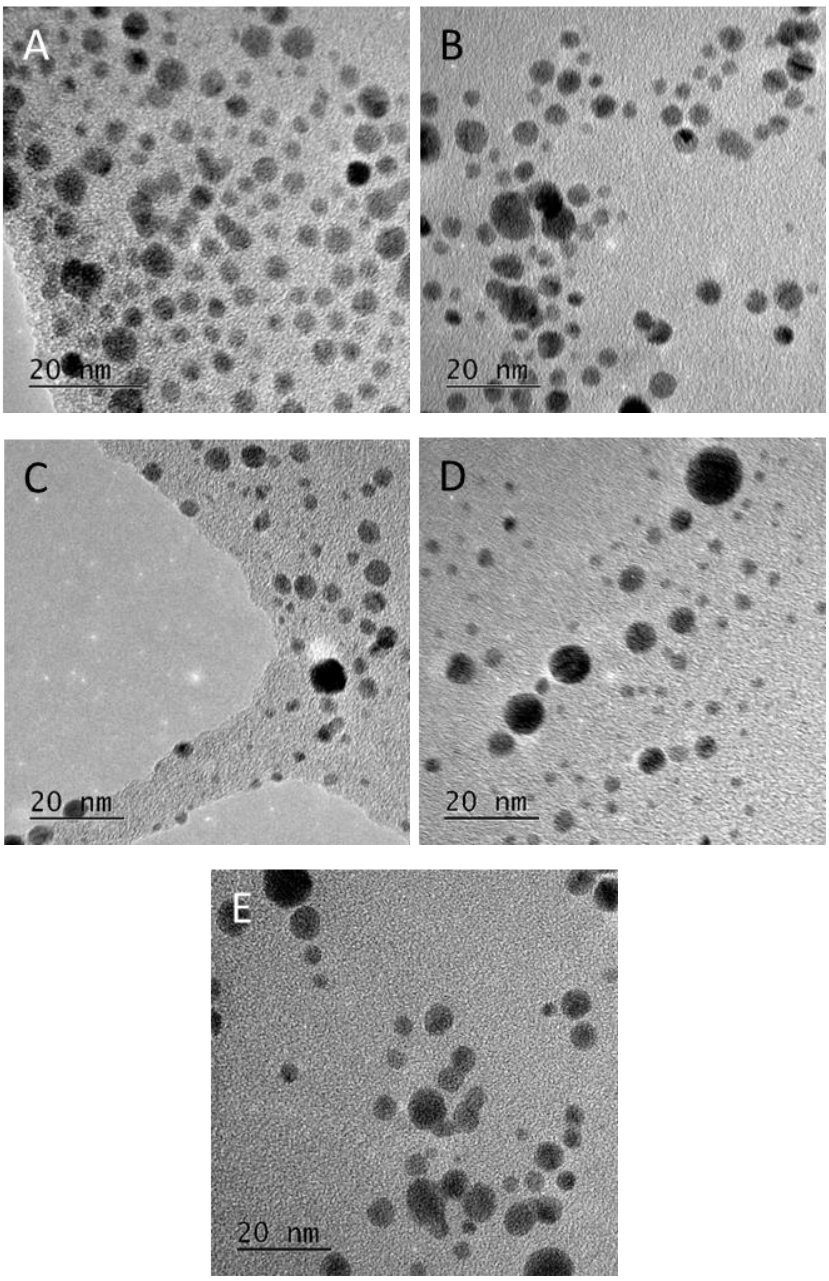

Figure 12. Selected TEM images of colloidal Ag prepared using continuous flow methods with varied reactor residence time; A) 1 minute, B) 2 minutes, C) 5 minutes, D) 10 minutes and E) 15 minutes.

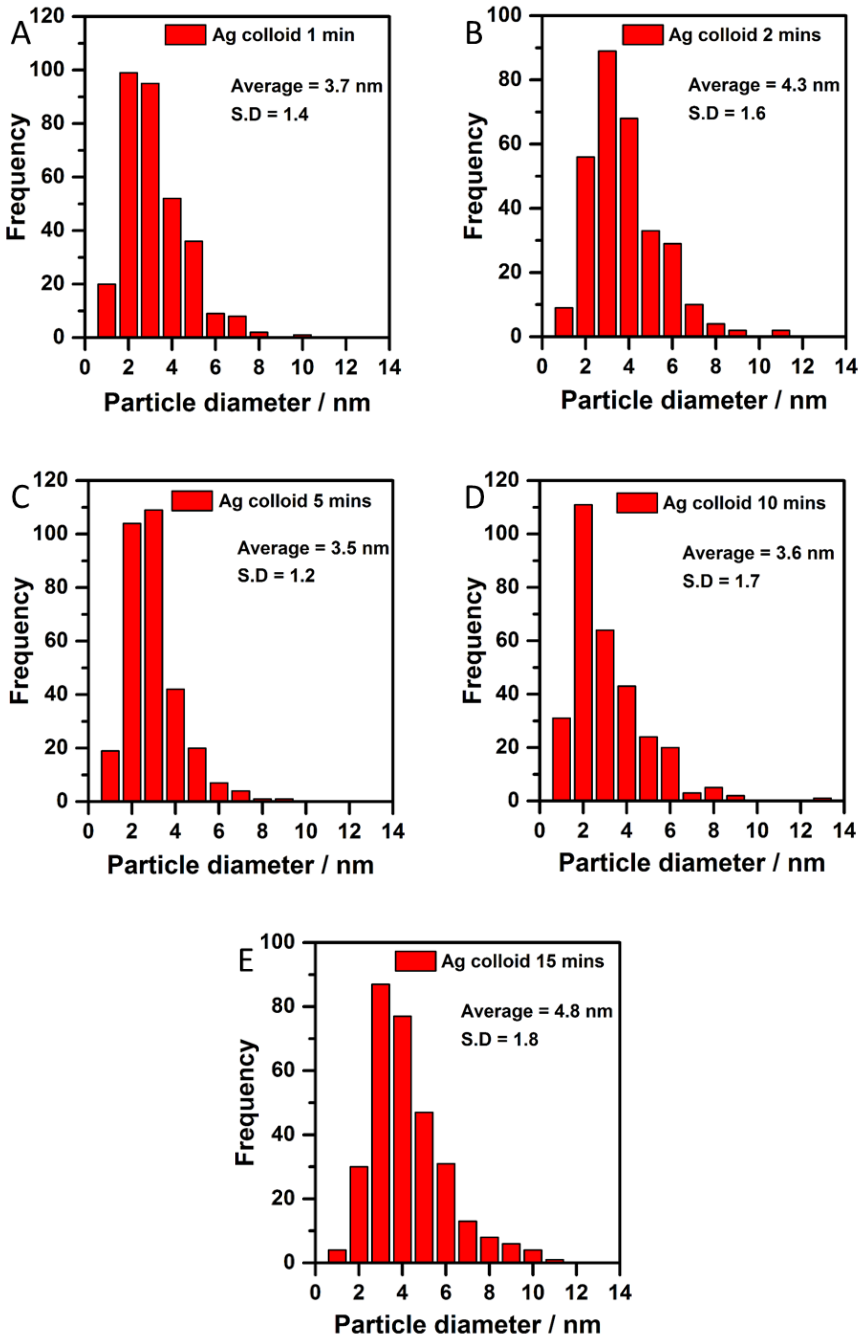

Figure 13. Ag particle size histograms for colloidal Ag prepared using continuous flow methods with varied reactor residence time; A) 1 minute, B) 2 minutes, C) 5 minutes, D) 10 minutes and E) 15 minutes.

3.3. *In situ* Experiment

3.3.1. Si/glass Microreactor

The X-ray transmission (I_t) map of the Si/glass microreactor (figure 14A) clearly indicates the channel positions. Figure 14B illustrates the Pt XRF map, obtained upon flowing reagent A (Pt + PVA solution) through channel A and H_2O solvent through channel B. As a result of the continued separation between the Pt solution (figure 14B, green colour) and H_2O through the reactor channel, it is evident that the type of flow through the reactor is laminar, and does not become turbulent despite flowing through U-bends. After switching the flow through channel B to reagent B ($NaBH_4$ solution) for 30 minutes and flushing both channels with solvent, the Pt α-emission fluorescence counts at varied points were used to monitor the amount of Pt deposition. At most points, the counts increased by over 50 %, indicating a significant amount of Pt metal deposition on the reactor walls during the reaction.

Figure 14. A) I_t map of the Si/glass micro-reactor zoomed in to the mixture region in the channel and B) Pt XRF map (green) indicating laminar flow through the Si/glass micro-reactor. (Pt solution and H_2O used as the reagents).

3.3.2. PTFE Reactor

The X-ray I_t map (figure 15A) illustrates the mixing channel, with the needle tip (channel B) evident on the left hand side. After flowing reagent A (Pt + PVA solution) and B ($NaBH_4$ solution) through the reactor for 30 minutes, followed by flushing with solvent, a Pt XRF map (figure 15B) was acquired to monitor the amount of Pt deposition on the PTFE reactor walls. The green colour on the edge of the reactor walls indicates Pt metal deposition, but after assessing the Pt α-emission fluorescence counts before and after reaction, the extent of deposition is not substantial. Pt α-emission

fluorescence counts near the reactor wall, close to the mixing point, increased from 133,000 to 141,000 counts per second (cps). The Pt deposition is only apparent on one side of the wall, indicating the flow through channel A is not uniform. A second issue encountered was the formation of bubbles in channel B, which collected and remained at the critical mixing point (figure 15C). These were hydrogen bubbles produced as a result of $NaBH_4$ decomposition.

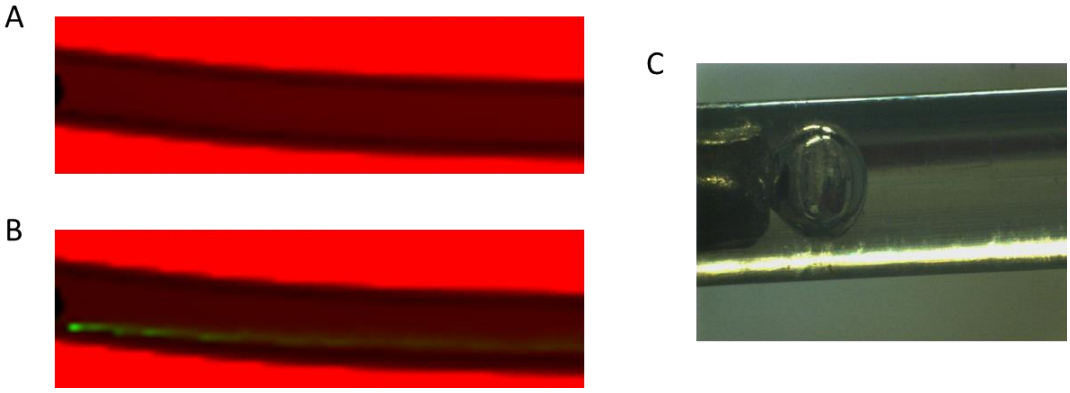

Figure 15. A) X-ray I_t map of the mixing channel in the PTFE reactor, B) Pt XRF map (green) of the PTFE reactor mixing channel after colloidal Pt formation, and solvent (H_2O) flushing and C) Photo of H_2 bubble formation occurring at the tip of the needle, produced through $NaBH_4$ decomposition.

3.3.3. PEEK Reactor

The Y-shaped channels can be observed in the X-ray I_t map (figure 16A). A dark area at the mixing point in the X-ray I_t map indicated there was a small bit of debris stuck near the mixing point, caused during the drilling of the channels. After flowing reagent A (Pt + PVA solution) and B ($NaBH_4$ solution) through the respective reactor channels for 30 minutes, followed by flushing with solvent, a Pt XRF map (figure 16B) was acquired to monitor the amount of Pt deposition on the PEEK reactor walls. The green colour along the mixing channel again indicates substantial Pt metal deposition. However, the Pt α-emission fluorescence counts measured before and after reaction indicates the Pt deposition is minimal, and is prominent only around the edge of the lodged debris.

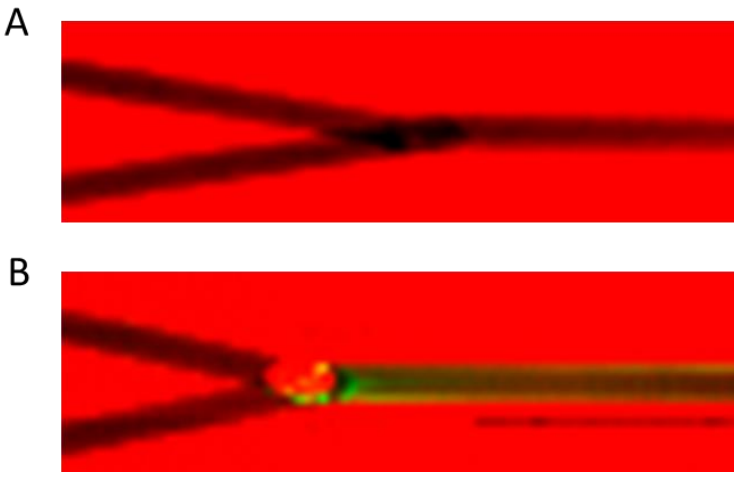

Figure 16. A) X-ray I_t map of the PEEK reactor with black representing the channel locations and B) Pt XRF map (green) of the PEEK reactor after reaction (colloidal Pt formation), and solvent (H_2O) flushing.

XANES measurements (figure 17) were taken along the mixing channel, in which the transformation of Pt^{2+} to Pt^0 is observed. Despite the low signal/noise ratio, it is clear that the white line feature indicative of oxidised Pt, disappears.[20]

Yao *et al.* summarised two pathways to which metal nanoparticle formation proceeds.[15] The first (path A) is where metallic ions are firstly fully reduced into zero valent atoms which then aggregate into nuclei and subsequent nanoparticles. The second (path B) involves the formation of cluster complexes by unreduced metal species, followed by the full reduction of the complexes to the metallic state. Although preliminary, *in situ* XANES measurements here indicate the first pathway of nanoparticle growth is more likely, as there is rapid transformation to the metallic state, which is probably a result of the strong reducing nature of $NaBH_4$, as other studies employing weaker reducing agents (methanol, citrate) have resulted in intermediate cluster complexes.[15, 21]

$$M^{x+} + xe \rightarrow M^0 \ , \ M^0 + M_n^0 \rightarrow M_{n+1}^0 \qquad \textbf{Path A}$$

$$M^{x+} + e \rightarrow M^{(x-1)^+} \ , \ M^{(x-1)^+} + M^{(x-1)^+} \rightarrow M_2^{(2x-2)^+} \qquad \textbf{Path B}$$

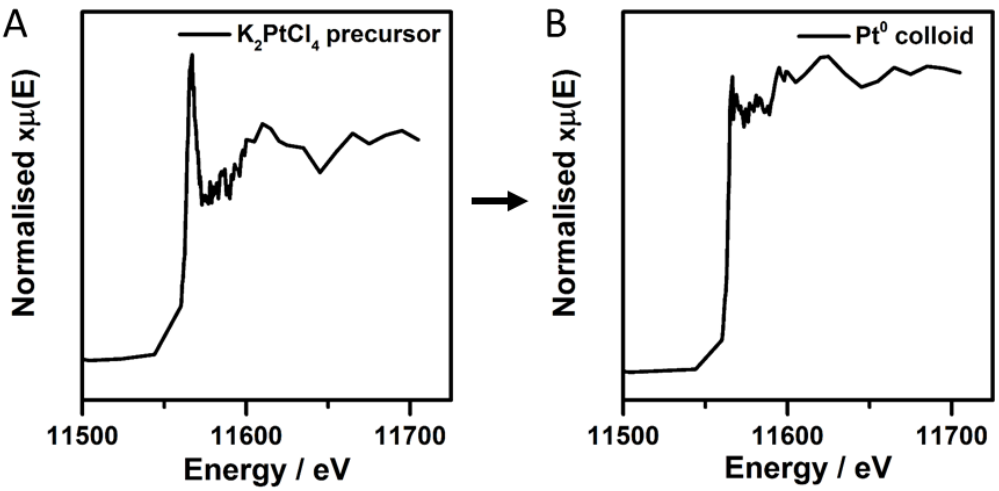

Figure 17. Normalised Pt L_3 XANES spectra of measurements collected at; A) at the start of the mixing channel and B) ~ 1 cm downstream of the mixing channel.

4. Summary and Conclusions

The results presented in this chapter demonstrate that PVA stabilised metal nanoparticles can be prepared with flow methods in which the reagents are continuously mixed with precise control over the flow rates, at a definitive point, through a reactor.

Au and Ag nanoparticles were successfully prepared, with UV-Vis spectroscopy indicating that the reactor residence time (reagent flow rate) is an important factor in the outcome of the afforded Ag particle size and particle distribution.

XAFS and XRF was employed to monitor nucleation, growth and metal deposition processes during colloidal formation in reactors fabricated from different materials. It was shown that for Si/glass microreactor, the type of flow through the cell was laminar, but more importantly there was a large extent of Pt metal deposition on the reactor walls during synthesis, impeding any more detailed investigations regarding the metal reduction process. For the reactor fabricated from PTFE, significantly less deposition was observed, but the reactor design promoted inconsistent mixing, and resulted in H_2 (from $NaBH_4$ decomposition) becoming stuck at the mixing point, again impeding investigation at the crucial stage. For the reactor fabricated from PEEK, with Y-shaped channels, not only was metal deposition minimal, but the metal reduction process was monitored along the mixing channel by assessing the XANES profile. Although the signal/noise ratio was very low in the XANES spectra, it is clear there is a rapid transformation from Pt^{2+} to Pt^0, indicating that the formation of zero valent stable nuclei is the first stage in the formation of Pt nanoparticles for this system.

5. References

1. Zhao, C.-X.; He, L.; Qiao, S. Z.; Middelberg, A. P. J. *Chemical Engineering Science,* 2011**,** ***66*** (7), 1463-1479.
2. Ying, Y.; Chen, G.; Zhao, Y.; Li, S.; Yuan, Q. *Chemical Engineering Journal,* 2008**,** ***135*** (3), 209-215.
3. Wagner, J.; Kohler, J. M. *Nano Letters,* 2005**,** ***5*** (4), 685-691.
4. Tsunoyama, H.; Ichikuni, N.; Tsukuda, T. *Langmuir,* 2008**,** ***24*** (20), 11327-11330.
5. Xue, Z. L.; Terepka, A. D.; Hong, Y. *Nano Letters,* 2004**,** ***4*** (11), 2227-2232.
6. Baumgard, J.; Vogt, A. M.; Kragl, U.; Jahnisch, K.; Steinfeldt, N. *Chemical Engineering Journal,* 2013**,** ***227***, 137-144.
7. Karim, A. M.; Al Hasan, N.; Ivanov, S.; Siefert, S.; Kelly, R. T.; Hallfors, N. G.; Benavidez, A.; Kovarik, L.; Jenkins, A.; Winans, R. E.; Datye, A. K. *Journal of Physical Chemistry C,* 2015**,** ***119*** (23), 13257-13267.
8. deMello, A. J. *Nature,* 2006**,** ***442*** (7101), 394-402.
9. Woehl, T. J.; Evans, J. E.; Arslan, L.; Ristenpart, W. D.; Browning, N. D. *Acs Nano,* 2012**,** ***6*** (10), 8599-8610.
10. Bonnemann, H.; Richards, R. M. *European Journal of Inorganic Chemistry,* 2001**,** (10), 2455-2480.
11. Polte, J.; Erler, R.; Thunemann, A. F.; Sokolov, S.; Ahner, T. T.; Rademann, K.; Emmerling, F.; Kraehnert, R. *Acs Nano,* 2010**,** ***4*** (2), 1076-1082.
12. McKenzie, L. C.; Haben, P. M.; Kevan, S. D.; Hutchison, J. E. *Journal of Physical Chemistry C,* 2010**,** ***114*** (50), 22055-22063.
13. Polte, J.; Kraehnert, R.; Radtke, M.; Reinholz, U.; Riesemeier, H.; Thunemann, A. F.; Emmerling, F. *Xiv International Conference on Small-Angle Scattering*, Ungar, G., Ed. Iop Publishing Ltd, 2010; Vol. 247.
14. Polte, J.; Ahner, T. T.; Delissen, F.; Sokolov, S.; Emmerling, F.; Thunemann, A. F.; Kraehnert, R. *Journal of the American Chemical Society,* 2010**,** ***132*** (4), 1296-1301.
15. Yao, T.; Sun, Z. H.; Li, Y. Y.; Pan, Z. Y.; Wei, H.; Xie, Y.; Nomura, M.; Niwa, Y.; Yan, W. S.; Wu, Z. Y.; Jiang, Y.; Liu, Q. H.; Wei, S. Q. *Journal of the American Chemical Society,* 2010**,** ***132*** (22), 7696-7701.
16. Silverwood, I. P.; Ai-Rifai, N.; Cao, E.; Nelson, D. J.; Chutia, A.; Wells, P. P.; Nolan, S. P.; Frogley, M. D.; Cinque, G.; Gavriilidis, A.; Catlow, C. R. A. *Review of Scientific Instruments,* 2016**,** ***87*** (2), 5.
17. Bianchi, C. L.; Canton, P.; Dimitratos, N.; Porta, F.; Prati, L. *Catalysis Today,* 2005**,** ***102–103*** (0), 203-212.

18. Patil, G. A.; Bari, M. L.; Bhanvase, B. A.; Ganvir, V.; Mishra, S.; Sonawane, S. H. *Chemical Engineering and Processing,* 2012***, 62***, 69-77.
19. Kennedy, J.; Jones, W.; Morgan, D. J.; Bowker, M.; Lu, L.; Kiely, C. J.; Wells, P. P.; Dimitratos, N. *Catalysis, Structure & Reactivity,* 2015***, 1*** (1), 35-43.
20. Yoshida, H.; Nonoyama, S.; Yazawa, Y.; Hattori, T. *Physica Scripta,* 2005***, T115***, 813-815.
21. Chen, S. M.; Yang, Q. Y.; Wang, H. H.; Zhang, S.; Li, J.; Wang, Y.; Chu, W. S.; Ye, Q.; Song, L. *Nano Letters,* 2015***, 15*** (9), 5961-5968.

Chapter Seven. Summary, Conclusions and Future Work

In the field of catalysis there is a requirement to effectively prepare metal nano-particulate catalysts with control over the catalyst properties, including metal particle size, shape and structure. The research presented in this thesis was based on three main themes; designing a reproducible experimental protocol for the preparation of supported metal nanoparticle catalysts with tailored properties: investigating the effect of the catalyst properties on important catalytic reactions; and exploring/developing metal nanoparticle synthesis using continuous flow methods.

In chapters 3, 4 and 5, an established sol-immobilisation method, in which PVA stabilised metal nanoparticle particles are 'preformed' in a colloidal mixture before anchored to a support material, was modified by applying temperature and solvent environment variations. Mixed ratios of H_2O and EtOH were employed, with the minimum temperature dependent on the solvents freezing point. Within each independent solvent environment, the size of metal nanoparticle generated, increased as a function of temperature. Out of all the prepared catalysts, it was established that low temperature colloidal reduction yields the smallest metal nanoparticles, with the smallest metal nanoparticles afforded when a 50:50 H_2O:EtOH volume ratio, at −30°C was employed. However, the number of small metal clusters (< 5 atoms for Au and < 20 atoms for Pd) as well as the surface sites available are heavily affected by the solvent environment employed during synthesis, with preparation in H_2O yielding the greater population of these isolated sites.

Despite efforts to decrease further the metal particle size by switching to pure EtOH solvent and reducing the temperature further, this approach proved unsuccessful. We consider that the insoluble nature (without the use of any H_2O) of the stabilising agent (PVA), in EtOH, results in ineffective prevention against particle growth, leading to larger metal particles. Therefore, a future study should involve the replacement of PVA with a stabilising agent soluble in EtOH, so as to investigate the effect of temperature on the nano-metal properties over a larger temperature range, with particular interest in temperatures below −70°C.

TiO_2 supported Au and Pd catalysts, prepared by this modified sol-immobilisation method, were tested for their performance in a range of catalytic applications including the chemical upgrading of biomass derivatives, and the synthesis of important fine chemicals. We concluded that both the temperature and solvent environment were crucial in effecting the metal nanoparticle properties.

Chapter 3 showed that the activity of glycerol oxidation is heavily influenced by the metal particle size, but in particularly by sites containing low coordinated Au atoms. HAADF STEM analysis confirmed that the Au catalyst prepared in H_2O at 1°C possessed a high population of Au clusters (< 5 atoms), and hence the activity of this catalyst was higher than any other reported Au/TiO_2 catalyst (TOF = 915 hr^{-1}). It was interesting to note that catalysts with similar particle sizes, but prepared in different solvent systems, performed very differently.

By testing the Pd catalysts prepared by the modified sol-immobilisation method, for the hydrogenation of the α,β-unsaturated aldehyde furfural, the metal surface sites were investigated in more detail. Selectivity to hydrogenation of either the C=O or C=C bond depends on the orientation of the furfural bound at the metal surface and on the types of site available at the metal surface. Pd/TiO_2 catalysts prepared using a mixed H_2O:EtOH solvent were found to have a larger proportion of available corner and edge sites, which were able to adsorb furfural perpendicular to the nanoparticle surface, resulting in greater selectivity to form furfuryl alcohol (C=O) over the complete reduction product, tetrahydrofurfuryl alcohol (C=C and C=O). We also concluded that the selectivity profile does not correspond solely to particle size; for the B series (prepared in H_2O:EtOH mixed solvent) fufuryl alcohol selectivity decreases with increasing particle size, whereas for the A series (prepared in H_2O only solvent) the inverse relationship is found. The available sites are therefore also a consequence of the interaction of the protecting agent with the nanoparticles prepared. This influence was also manifested in recycling studies, where those catalysts prepared in mixed H_2O:EtOH solvent, were more robust than those prepared solely in H_2O, with the catalysts prepared in the latter solvent more susceptible to the formation of Pd carbide, which is proposed to be responsible for the deactivation observed. To our knowledge, this is the first report of this deactivation pathway for the hydrogenation of α, β-unsaturated aldehydes.

In chapter 5, Pd catalysts were tested for the hydrogenation of *p*-nitrophenol to produce *p*-aminophenol, an important intermediate in the synthesis of the antipyretic drug paracetamol. The work concluded that the catalytic activity is directly correlated with Pd particle size (Pd surface area), dispersion and Pd-TiO_2 interaction. The Pd catalyst with the smallest particle size (prepared at 1°C) not only exhibited the highest activity comparable to other Pd (TOF 333 hr^{-1}), but better recyclability. UV-Vis spectroscopy permits fast, *in situ* monitoring of the catalytic reaction. However, there are limitations with this technique, particularly when testing TiO_2 supported catalysts; high analyte concentration and stirring are not permitted as both saturate the UV-Vis detector. Therefore, we propose that performing the reaction in a larger batch reactor, with controlled stirring, will not only enable more accurate analysis of the catalytic activity of TiO_2 supported catalysts, but enable higher substrate/metal ratios to be employed with improved practicality.

All of the work presented in this thesis focused on the preparation of monometallic catalysts, but there has been considerable interest in the preparation of bi-metallic catalysts, which have demonstrated superior catalytic performance in a range of applications, including photocatalytic hydrogen production and alcohol oxidation. The structure of the metals, either core-shell, alloyed or segregated has proven decisive in the observed activity, with the arrangement dependent on the experimental protocol of preparation. An interesting field of work would be to tailor the size of the core metal using the methods developed in this work, which would subsequently alter the electronic properties of the bimetallic particle, affecting catalytic behaviour. Indeed, the work has opened up endless possibilities of work that could be performed: metals, stabilisers, reductants, solvents, temperatures, metals and supports can all be varied, as well as the different catalytic applications.

All catalysts prepared in chapters 3-5 used batch methods, essentially synthesis in a macroscale vessel. Chapter 6 explored the preparation of PVA-stabilised metal nanoparticles by flow methods instead, in which the reagents are continuously mixed through a reactor with precise control over the flow rates. Ag nanoparticles were prepared with different reactor residence times, and by monitoring the surface plasmon resonance band in the UV-Vis spectrum; we concluded that the flow rate is an important parameter influencing the Ag particle size. However, monitoring nucleation and growth processes that occur during metal nanoparticle formation is difficult due

to the fast reaction kinetics. Preparing metal nanoparticles in a continuous flow method in principle allows the particle formation to be monitored without kinetic limitations, as each point along the mixing channel becomes a static time point. *In situ* XAFS and XRF was used to investigate Pt colloidal generation in three reactor fabricated from different materials. Pt metal deposition on the reactor walls of a Si/glass microreactor limited the ability to monitor the reaction, but interestingly, XRF helped elucidate the type of flow through the reactor to be laminar. A PTFE reactor helped reduce the metal deposition, but the flow was inconsistent as well as hydrogen bubble formation hindering the analysis. The reactor that showed the most potential was fabricated from PEEK, in which the channels were positioned in a Y-shape. Not only was the metal deposition minimal, but more importantly the XANES spectra taken at different points along the mixing channel indicated metal reduction had taken place.

To perform an experiment of this nature in the future is challenging, and improvements need to be made based on the observations during the experiments conducted here. Understanding and mitigating the cause of metal deposition, is fundamental to the success of this experiment, which can only be improved by exploring, in depth, different reactor fabrications with varied channel paths (mixing) and flow rates. To observe nucleation and growth kinetics a weaker reductant, such as citrate, would be the ideal candidate. $NaBH_4$ as the reductant not only results in very fast colloidal metal formation, but also presents issues with analysis due to the hydrogen formation upon decomposition.

Finally, the work presented in this thesis demonstrates major progress in controlling metal nanoparticle synthesis, with substantial implications for catalysis.